ESTIMATES OF CRUSTAL TRANSMISSION LOSSES USING MLM ARRAY PROCESSING

by

EDWARD KURT SCHEER

S.B., Massachusetts Institute of Technology
(1972)

S.B., Massachusetts Institute of Technology
(1972)

SUBMITTED IN PARTIAL FULFILLMENT
OF THE REQUIREMENTS FOR THE DEGREE OF

OCEAN ENGINEER

at the

MASSACHUSETTS INSTITUTE OF TECHNOLOGY

and the

WOODS HOLE OCEANOGRAPHIC INSTITUTION

MAY 1982

Signature of Author..... .....
Department of Ocean Engineering,
May 1982

Certified by..... .....
Thesis Supervisor

Accepted by..... .....
Chairman, Joint Committee on Ocean Engineering,
WHOI/MIT Joint Program

ACKNOWLEDGMENTS

Of all the persons who have helped me during the past few years, I first thank Cathy for putting up with me in the most trying times, and for her love and support. Then I must thank Heidi for giving me the final push to get everything done. Art Baggeroer did some pushing too, and I am indebted to him for his valuable advice and guidance.

I am grateful to the MIT/WHOI Joint Program office for providing support for graphics and reproduction costs.

Thanks to Ken Prada and Dave Gever for answering many "stupid questions", and for letting someone like me get near their computer.

To my parents: Vielen Dank!!

I am especially grateful to Betsey Pratt for her figures, and to Gretchen McManamin for her Wang.

For helping maintain my sanity, I must thank Norbert's brother, Bill Weaner, Fifi Larue, Bill Cox, D.I.G., the staff and management of the Copley Plaza Hotel, Lulu, Taffy, Scummy, and the boys in the band.

This work was supported under ONR contract N-00014-75-C-0852.

CHAPTER I

INTRODUCTION

Background

Seismic refraction experiments have been used extensively in the past thirty five years in investigations of the structure of the oceanic crust. The longer range of the refraction or wide angle reflection technique, on the order of tens of kilometers, permits a deeper and wider area of examination, although with less resolution, than the spatially limited seismic reflection experiment. Observations of arrivals from the Mohorovicic discontinuity, at an average depth of seven kilometers below the sea floor, are routinely made.

The major focus in interpreting refraction data has been the analysis of travel time/range data and the "inversion" of this data for the purpose of determining a velocity versus depth profile of the crust. The most frequent application of this procedure is the geophysicist's use of velocities for postulating geologic structures and rock types below the sediment (Christensen & Salisbury, 1975). Another area using refraction data, less widely seen, falls into the ocean acoustician's domain. In studying the behaviour of sound in the ocean, the sea floor is often modelled as a boundary with a half space below, and with some form of reflection characteristic and/or loss mechanism. If acoustic energy, upon encountering the bottom, was either reflected or transmitted directly, this would be appropriate, and the determination of reflection and transmission coefficients for the sea-sediment interface would probably be sufficient. However, sound energy does penetrate beneath the sea

floor and is both reflected and refracted back to the water. In an active acoustical experiment, especially at longer ranges, a significant amount of the received energy may come from waves that have interacted with the earth's crust and have been reinjected into the water. Since these arrivals can be detected in the ocean, their study is of concern for the acoustician.

The role of bottom interaction, especially at low frequencies, is now an area of intense research activity in modelling acoustic propagation. In particular, in the language of the sonar engineer, the TL, or transmission loss, of this energy is of major importance for i) predicting the character of the sound field at a receiver in future experiments, ii) for comparing crustal loss with the better known TL of paths remaining primarily in the water layer, and iii) expanding the role of arrival amplitudes in inversion theory. Just as there may be a number of possible paths in the sea between a source and receiver, each with a different loss characteristic, trajectories in the crust are variegated and exhibit different TL behaviors. It is important to be able to differentiate the energy partitioned among the different paths, and to determine which paths are most important.

Resolving the locus of a particular acoustic path is intimately tied to the problem of determining the velocity structure of a medium. To the limits of the geometrical optics approximation of acoustic behaviour, sometimes sorely pressed at low frequencies, a completely detailed knowledge of sound speed variations, both laterally and with depth, plus known source characteristics and attenuation losses in the medium, enables one in principle to predict signals observed at a receiver. For an ocean acoustician, the

requirement of environmental knowledge of the sound speed profiles, both in water and crust, needed to predict the amplitude and timing of data, is clearly very burdensome. In the past twenty five years, however, models of the oceanic crust have been formulated which are statistically consistent over much of the oceans. These models divide the crust into three or more horizontal layers with certain average thicknesses and velocities (Raitt, 1963). At least within the confines of these models, if a typical transmission loss were known for each of these layers, an acoustician can make predictions of the expected strength and timing of crustal arrivals at other stations. Most of this environmental information has been obtained from refraction and/or wide angle reflection data, usually via travel time analysis. Little has been done in developing models accounting for amplitude dependence.

Arrays for Refraction Experiments

The standard technique in ocean refraction experiments has basically involved one ship and one or more receivers (sonobuoy or OBS), with increasing range between shots. With a dense shot spacing and large enough total range, the use of event arrival times, especially the first ones, for the most prominent features in the data has been sufficient for obtaining a reasonably good understanding of the velocity structure of the crust. The crustal model referred to above was developed from averaging experiments of this type from many diverse areas. Lately, a multichannel hydrophone array has replaced the single receiver in some experiments, with the array sometimes being towed by a second ship (Stoffa, Buhl, 1979). In the latter technique, termed an expanding

spread profile (ESP), the two ships start at a common point and steam in opposite directions. In this way, a common depth point is shared by all shots. With the use of a Raydist apparatus, accurate range information, which is a sensitive parameter in the inversion methods, is also available. As with all arrays, the SNR for the detection of coherent energy can be improved with appropriate processing. Moreover, estimates of the received energy for different horizontal phase velocities can be made which, under the condition of horizontal crustal layering, provides us with crustal velocity estimates using just one shot. However, for a single offset, complete information concerning crustal structure is not be obtained since the SNR for certain events is range dependent.

Since receiver arrays have the ability of generating phase velocity information on a shot by shot basis, the process of traveltime analysis used in inversion studies can be somewhat automated. The original procedures of generating a travel time versus range plot for a sequence of densely spaced shots and visually picking arrivals can be improved by using an array velocity analysis technique that can assign velocities to arrivals in each shot trace. An expanded use of data received from one shot would minimize interpretation errors caused by uncertainties in range and source level variations. Clearly, once a composite of a number of shot traces is developed with estimated phase velocities along the trace for each shot, the problem of selecting different arrival times for a particular velocity is eased, and the intercept times can be found for use in traveltime inversion techniques, eg. the tau-p method (Stoffa, Diebold, & Buhl, 1981). Array processing techniques are also

important in discriminating distinct phenomena that occur in the multipath reverberation one encounters after the first refracted arrival, and effects of local inhomogeneities such as bathymetric variations in exploration and/or oceanographic experiments.

Velocity Analysis

A conventional way of doing array velocity analysis employs a statistic that estimates the amount of trace to trace coherence across the array, for a given assumed phase velocity. All realistic velocities are scanned, and the normalized statistic, a "semblance coefficient", indicates the relative amount of energy in the data, at each velocity (Sereda and Hajnal, 1976). Another method, used throughout in what follows here, employs a data adaptive spectral estimator. Several data adaptive techniques were originally developed in various areas, particularly large aperture teleseismic arrays and sonars. The Maximum Liklihood Method (Capon, 1969; Edelblute, 1967; Lacoss, 1971) was used at Woods Hole originally in the processing of reflection data (Leverette,1977), and eventually extended to seismic refraction work (Baggeroer and Falconer,1981). The technique conceptually designs a beamformer based on the input data (hence data adaptive). This beamformer minimizes output power with the constraint that energy from a specific direction is passed undistorted. We shall see that the structure of this beamformer can be used to define an algorithm that estimates what is known as the frequency-wavenumber function of the acoustic field for a certain spatial frequency associated with a specific direction. Insofar as the directions of

the arrivals at the array are related to the crustal sound speed of the paths the energy has traversed, estimated directions lead to estimated velocities. In the horizontal layering situation, this relationship is quite simple and the velocities estimated are very accurate, especially at high SNR.

In stochastic process theory, the power spectral density function is a measure of the partitioning of energy in a process with respect to frequency. The corresponding function for a wide sense stationary random process in space and time is the frequency-wavenumber function. It is a measure of the mean square power per unit bandwidth in temporal frequency arriving from a unit steradian in spatial frequency or wavenumber, which is uniquely related to horizontal phase velocity. The estimated function indicates the amount of energy that has arrived at the array via a particular path.

The acoustic field generated by an explosion, however, cannot be modelled as a stationary process. With the transient nature of the field, only a small part of the data is used. This "windowed" data must then be treated as if it were part of an ongoing, time invariant process. The power estimated in the hypothetical process is an indication of the actual energy, needed for true amplitude measurement, in the windowed data segments that were employed. The concept of windowing data to track nonstationary phenomena is extensively used in signal processing, particularly speech analysis. This technique is often referred to as "short time, spectral estimation".

The MLM estimate is known to be biased (Capon, 1969). An analytic expression for this bias has yet to be developed for all possible situations, however. We an empirical technique that can be used to evaluate the bias for

the particular data set and array configuration discussed below. Given a accurate estimate of the frequency/wavenumber function and the energy spectrum of a source, the transmission loss for a certain ray path can be determined.

The Rose Experiment

The MLM algorithm and our transmission loss calculation procedure will be applied to a data set obtained from a large scale acoustic/seismic program (ROSE) conducted off the western coast of Mexico in January 1979, near the East Pacific Rise. Together with seventy ocean bottom seismometers, a vertical (MABS) and a horizontal (ESP) array were used to receive acoustic energy generated by a series of explosions. The horizontal array was towed so that data was received in the ESP format described above. The vertical array was stationary. The use of these two types of array deployments, and of the bottom receivers, resulted in one experiment employing most of the techniques currently used in seismic refraction work.

Insofar as the experiment occurred near an active plate boundary, the structural makeup of the crust was not "typical", and difficulties were experienced in relating the velocity estimates obtained from single shots to the simple layered models discussed above. As we shall see, the complex seafloor topography also limited the accuracy of our calculated velocities. However, interesting and useful results were obtained and estimates of crustal energy partitioning shall be presented.

Overview

In Chapter II, a summary of the standard theories of seismic refraction is given. The emphasis is on current ideas concerning the strength of refracted waves. Next we discuss the data set and describe the different experiments conducted in the ROSE project. Chapter IV deals with the velocity spectral algorithm and the method used to determine bias corrections. Chapter V presents some results of the computations done on the data with respect to velocity estimation. Next, we describe the compensations that were necessary to make the measurements obtained from the algorithm correspond to transmission loss estimates in physical units. Source levels, biases, surface effects, group beampatterns, sensitivities, and analog to digital conversion factors must all be included to arrive at estimates of path losses. Finally, a summary of transmission loss estimates from this data set is presented.

CHAPTER II

SEISMIC REFRACTION

In this chapter, the fundamental concepts underlying the refraction experiment are presented. In particular, we concentrate on factors influencing the travel time and amplitude of arrivals. The material discussed is mainly a review for the geophysicist, but may not be as familiar for the ocean acoustician.

We begin with the free space solution of the wave equation in a homogeneous, isotropic elastic solid. We then discuss acoustic propagation in a simple layered medium, with one interface separating two isovelocity half spaces. Using a high frequency, ray theory analysis, the concept of a critically refracted interface wave is presented. We show that this analysis, based on the "geometrical optics" model of sound propagation, does not explain empirical observations of remotely sensed acoustic events, and turn to a "wave theory" analysis in which the concept of "head waves" is introduced. Travel times in layered media are accurately predicted by head wave theory. A second interface, representing the sea surface, is added to the model and we define specific events observed in the ROSE data which can be represented in terms of head waves and surface reflections from this model. Since the ocean crust is not an isovelocity layer, the model is then extended to include multiple interfaces below the seabed. Events received at different horizontal offsets, based on the multiple layer model and head wave theory, are presented in the form of a theoretical travel time/offset (T-X) diagram. Because of the absence of events that correspond to expected interlayer reflections with this model

in most refraction data, the model of the crust is finally generalized as a region with a continuous velocity gradient. The current perspective of oceanic crust is based on this last model, which provides better agreement with observed arrival amplitude behavior. We show, however, that some layers or interfaces of the classical layered model of the crust mentioned in Chapter I have counterparts as regions with very small or very large velocity gradients respectively in the continuous model. Finally, since we are concerned with energy partitioning in the crust, current theories of head wave (in layered media) and ray (in continuous models) amplitude behavior with respect to range are presented.

Free Space Propagation

Let $\overline{\Phi}$ and $\overline{\Psi}$ be defined as the Fourier transforms of the dilational and rotational displacement potentials in an elastic solid. Under the conditions of homogeneity and isotropy, the Helmholtz equations in free space for these quantities are (Grant & West, 1965):

$$\nabla^2 \overline{\Phi} + k_\alpha^2 \overline{\Phi} = 0 \qquad (2\text{-}1a)$$

$$\nabla^2 \overline{\Psi} + k_\beta^2 \overline{\Psi} = 0 \qquad (2\text{-}1b)$$

where:

$$k_\alpha = \omega \Big/ \sqrt{\frac{\lambda+2\mu}{\rho}} \triangleq \omega/\alpha \qquad (2\text{-}2a)$$

$$k_\beta = \omega \Big/ \sqrt{\lambda/\rho} \triangleq \omega/\beta \qquad (2\text{-}2b)$$

λ and μ are Lame's constants, ω is the radian frequency, and ρ is the density of the solid. In a homogeneous, free space, two dimensional geometry, a solution found by separating variables, is given by:

$$\overline{\Phi}(x,z:\omega) = A(\omega)\, e^{j 2\pi \nu_\alpha (lx + nz)} \qquad (2\text{-}3)$$

where $l^2 + n^2 = 1$, $\nu_\alpha = k_\alpha / 2\pi$, and $A(\omega)$, corresponding to temporal behaviour, is an arbitrary function. This solution represents a compressional (P) plane wave traveling with velocity α in a direction with cosines $(l, 0, n)$. The "wavenumbers" k_α and ν_α represent spatial frequency in radians and cycles per unit distance, respectively. The solution for Ψ is the same, except that the phase speed is β , and the displacements are orthogonal to the direction of propagation, representing "shear" (S) waves.

Medium with one interface

We now turn from the free space model, and consider a medium with one horizontal plane boundary separating elastic half-spaces with velocities α_1 , β_1 and α_2, β_2 as in Fig. 2-1 (Telford et al, 1976). An incident compressional plane wave with amplitude A_o imposes the boundary condition that apparent wave numbers in a direction parallel to the interface are constant. This leads to Snell's law:

$$\frac{\sin\theta_1}{\alpha_1} = \frac{\sin\theta_2}{\alpha_2} = \frac{\sin\lambda_1}{\beta_1} = \frac{\sin\lambda_2}{\beta_2} \triangleq p \qquad (2\text{-}4)$$

where θ_1 is the angle both of incidence and of P-wave reflection, (θ_2, λ_2) are the angles for P and S plane wavefronts that are "refracted" into the second layer. λ_1 is the angle of reflection for an S wave in the upper layer and the constant p is termed the ray parameter. If the sound velocity in the second layer is greater than α_2 , we see that there is a critical incidence angle, θ_c , when $\sin\theta_2 = 1$. At incident angles θ_c , a compressional plane wave solution exists that travels parallel to the boundary as an interface

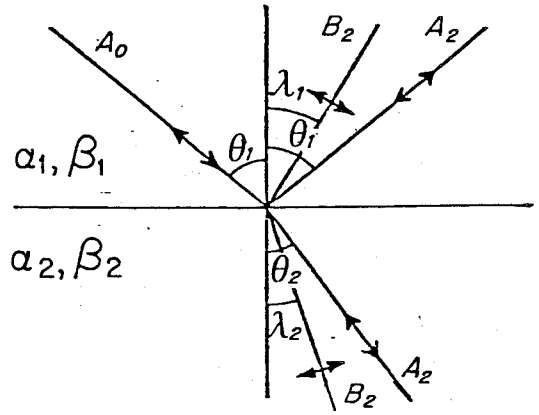

Fig. 2-1
Geometry of reflected and refracted waves at one interface.

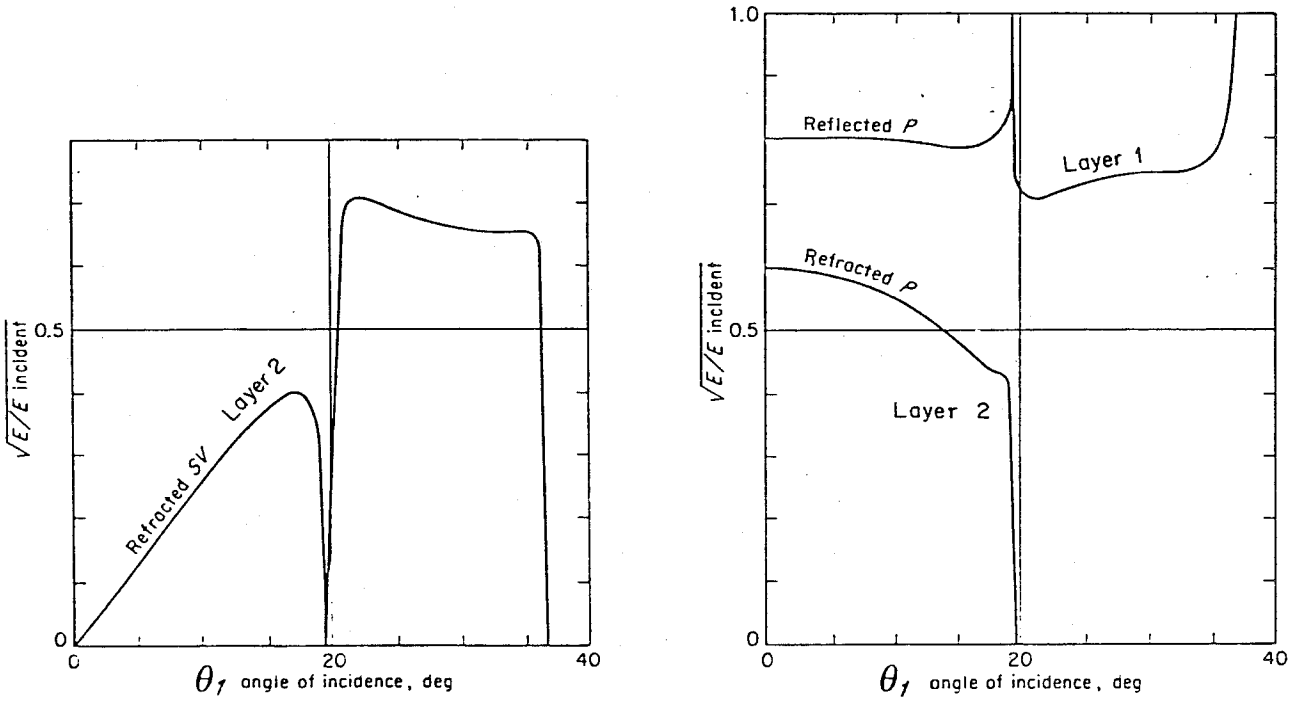

Fig.2-2
Amplitudes of reflected and refracted compressional (P) and shear (SV) waves versus angle of incidence at one interface for / = .33 and / =.6.
(from Grant & West, 1965)

wave. This solution is the basis of all simple refraction theories and formulae. The "critically refracted" wave travels with the higher speed, α_2, so that at large horizontal ranges, it should be the earliest arrival.

From this ray theory or geometrical optics viewpoint, however, the interface wave will not appear in the upper layer, and its predicted amplitude is zero. The latter fact is seen by applying six boundary conditions of continuity of stress and displacement at the interface to eqs. 2-1, whereby the Knott equations (Telford, 1976) in terms of the potential function amplitudes, or the Zoeppritz formulae for the displacement amplitudes (Grant & West, 1965) are derived. An example, calculated from these equations, is shown in fig. 2-2 (from Grant & West) in which ratios of incident amplitude to the refracted P and S amplitudes in the lower layer and to the reflected P amplitude in the upper layer are shown versus angle of incidence for a fluid-solid boundary. In these, $\alpha_1/\alpha_2 = 1/3$ and $\beta_1/\beta_2 = .6$. The critical angle for the compressional (P) and shear (SV) waves are thus $\sin^{-1}(1/3) = 19.5^\circ$, and $\sin^{-1}(.6) = 37^\circ$, respectively. In the ROSE experiment, typical critical angles for P waves were in the 10° to 15° range. Note that, in these figures, all energy in the upper layer is either incident or is reflected from the interface at angles other than critical, while amplitudes associated with interface waves at the critical angles is zero. It is observed, however, that significant energy with travel times much as one would calculate for an interface wave with speed α_2 refracting energy into the water at the critical angle, does appear in refraction experiments.

Head waves

The most widespread theory to explain this is based on Huygen's principle using curved instead of ideal planar wavefronts. It predicts the existence of "head waves" as shown in Fig. 2-3 (from Cerveny and Ravindra, 1971). In 2-3-a, a spherical wavefront originating at M_o impinges upon the interface for time $t > h/\alpha_1$. At the boundary it sets up a disturbance along OP and creates Huygen wavelets (Fig 2-3-b) which produce the reflected and refracted wavefronts where constructive interference occurs. The speed along the interface of P, the contact point with the incident wavefront, is $\alpha_1 / \sin\theta(P)$. $\theta(P)$ is the angle from PM_o to the horizontal axis. Beyond a critical horizontal distance, $X_c = h / ((\alpha_2/\alpha_1)^2 - 1)^{1/2}$, the speed of this point becomes less than α_2. At this range, the angle $\theta(P)$ has increased to the critical angle $\theta^* = \theta_c$. We now get the situation in fig. 2-3-c. The refracted wave in layer 2 is now ahead of the incident or reflected fronts. Again using a Huygen construction, M^*Q is seen to be a locus of constructive interference, and for constant α_1 and α_2, is a straight line (in 2 dimensions). In time Δt, the disturbance at point O^* will move both to Q along the boundary at speed α_2, and to point M^* in layer 1 at speed α_1. The angle of this "head wave" is seen to be: $\sin^{-1}\left(\frac{\alpha_1 \Delta t}{\alpha_2 \Delta t}\right) = \theta_c$. Wave theory thus predicts that the Snell's law interface wave constantly reflects energy, in the form of a head wave, back into the uppermost layer at the critical angle. The apparent horizontal phase velocity of the head wave in layer 1 will be:

$$\frac{\alpha_1}{\sin\theta_c} = \alpha_2 = 1/p \qquad (2\text{-}5)$$

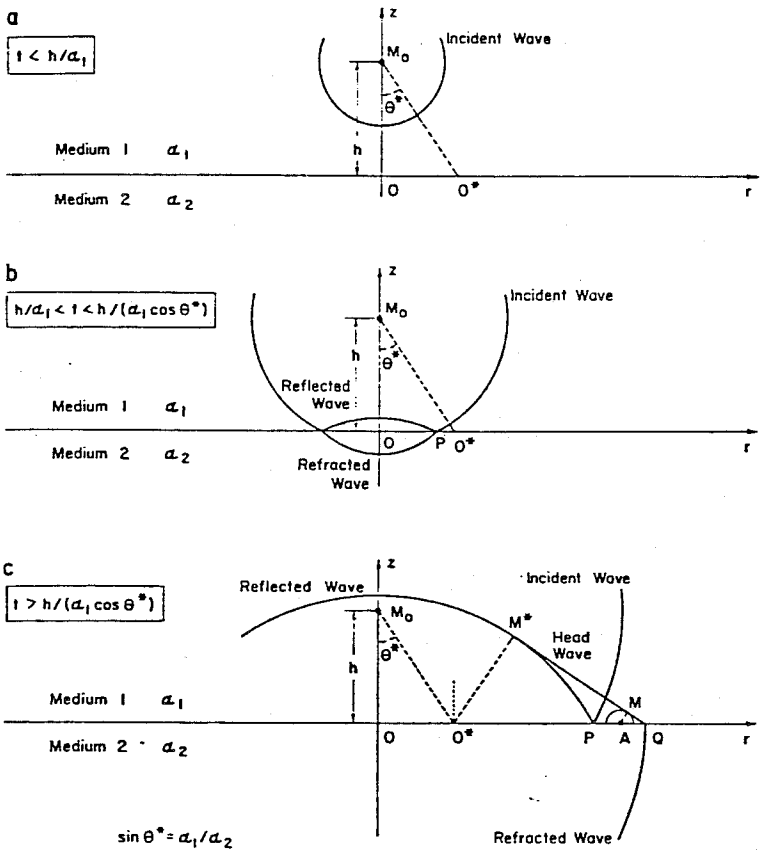

Fig.2-3
Construction of head wave using Huygen wavelets.
(from Cerveny & Ravindra, 1971)

Thus, if the direction of the refracted energy or the horizontal phase velocity of an emerging plane wavefront can be determined within the upper medium, the sound speed in layer 2 can be found remotely for a horizontally layered medium. This is the basis of classical inversion theory for two simple layers as discussed in Ewing, 1963.

Two interface model

We now modify the proceeding model by introducing a perfectly reflecting interface in the upper half space, representing the sea surface. Due to surface reflections, many arrivals other than those from emerging interface waves, will occur at a receiver with this model. Referring to Fig. 2-4, together with the critically refracted compressional wave labelled 1P, a converted shear wave (1S), a direct wave, and a series of water layer reflections (1W, 2W, etc), will be recorded at the array. Since 1P refracts energy continuously back into the water, a surface receiver may encounter energy which travels as an interface wave and refracts into the water. Upon reflection from the surface, this energy reenters the seabed, again as an interface wave, before finally refracting into the water and being detected. This "multiple refraction" is termed 2P in Fig. 2-4. More multiples of this type (3P, 4P, etc), for which an arrival has had a number of encounters with the surface, can be observed with velocity analysis in the array data presented subsequently. Often it is found that the amplitudes of 2P arrivals, and even those of higher multiples, are stronger than 1P. Since a multiple refraction arrival can be the sum of a large number of rays each travelling

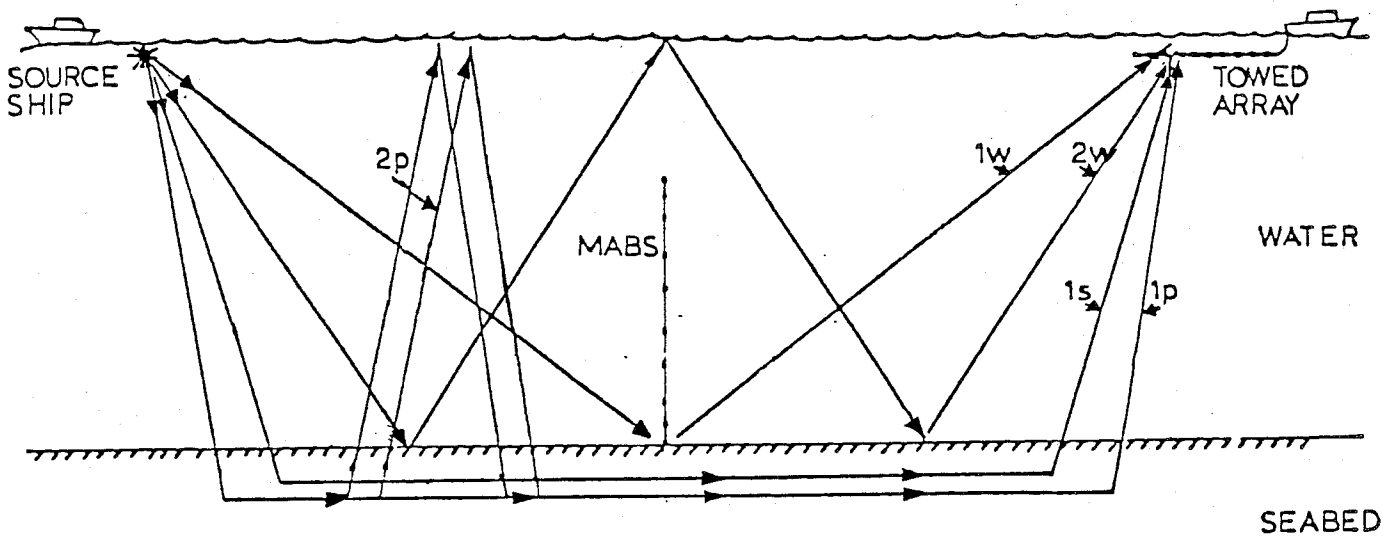

Fig.2-4
Possible ray paths with a two-interface model.

along a different path, this is possibly due to the constructive interference. While the exact acoustics solution still remains unsolved for these multiples, they are important from the ocean acoustician's perspective because of their relatively high energy levels.

Multiple layers

The upper layer in the two interface model discussed above represents the water. For the region below the seabed, we first introduce a multiple layer model and use head wave theory to predict events received at a horizontal offset X in the form of a travel time/offset (T-X) plot. As discussed in Chapter I, the original, "classical" model of the oceanic crust has 3 isovelocity layers above the mantle interface.

In a multiple layered case, the number of events one can expect is large, especially in sedimentary locales. Figure 2-5 depicts a situation with N interfaces. In constructing a time versus range (T-X) plot for this example, and concentrating only on critical refractions of first arrivals, we see that up to range X_{c1} , the first event is the "1P" from the layer with velocity V_o. When the range exceeds X_{c1}, the 1P event from the second boundary arrives earlier. With densely spaced sample points in range, the locus of the first arrival traces a straight line in the T-X plane with slope $1/V_1$. As range is increased beyond X_{c1}, the interface wave from the V_2 layer will eventually be the earliest arrival. This pattern continues until, at the largest distance, the slope of the first arrival line will be $1/V_N$. In this way, for a horizontal layered situation, in which layer velocities increase with depth,

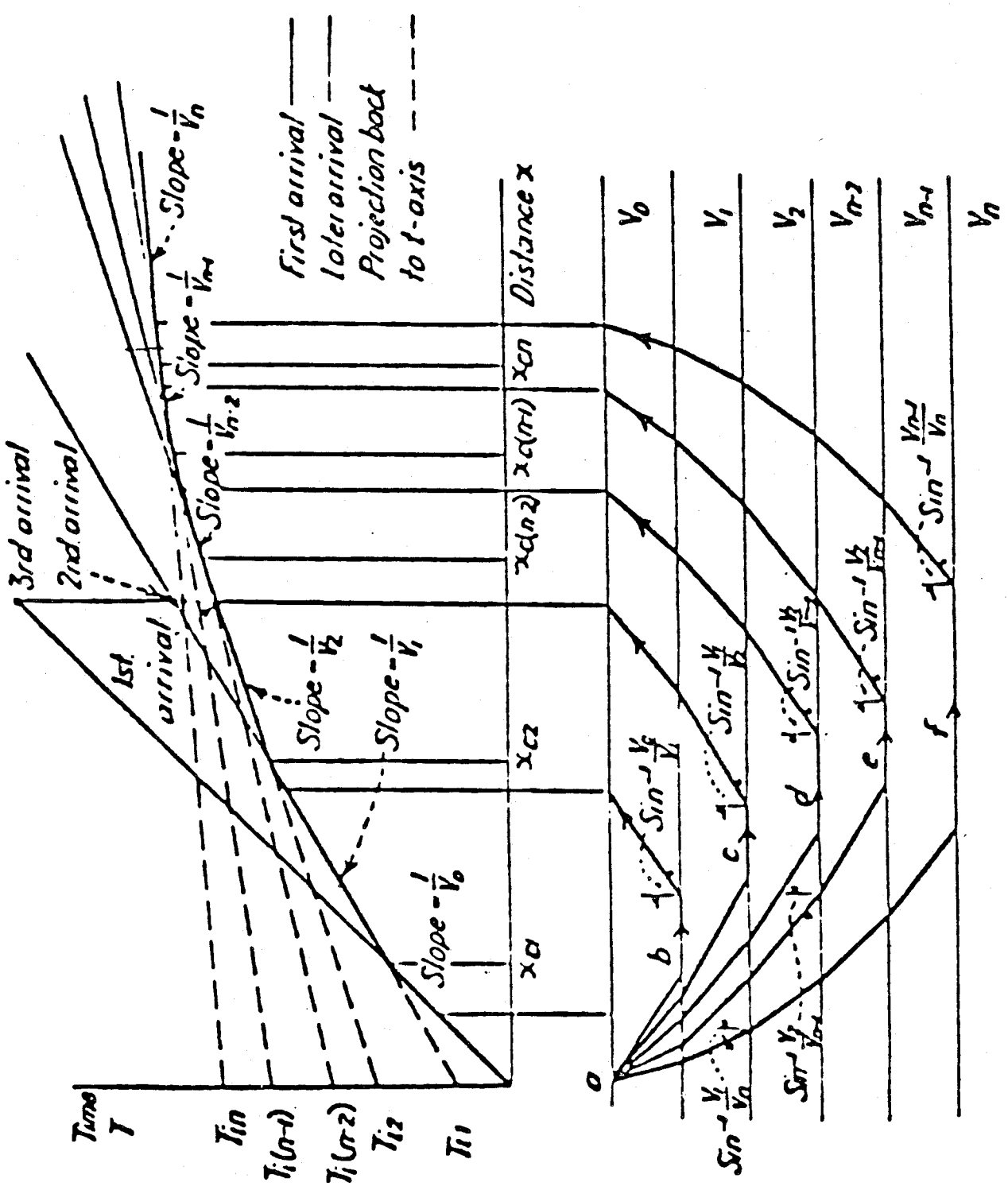

Fig.2-5
Theoretical T-X diagram for ideal multilayered medium.

the calculation of slopes from earliest arrivals on a T-X plot is sufficient for obtaining the layer velocities of interest.

For the multiple layer case, we have discussed arrivals due to head waves only. A T-X diagram for the multi-layer model is more complex than this because multiple reflections and multiple refractions from each of the interfaces are present. These appear after the first arrival. Except for those involving the water surface, seafloor, sedimentary layered sequences, and the mantle interface, interlayer reflections are rarely seen (Ewing & Houtz, 1969) in refraction data, however. An example of an actual T-X plot is shown in figure 2-6a (Detrick & Purdy, 1980) for an experiment conducted near the Kane fracture zone. The locus of events that can be attributed to layer reflections are limited to those designated by PmP, PmPPmP, and SmS, for the mantle interface, and PnWW for the ocean surface boundary (see key to path nomenclature in fig. 2-6b). In the ROSE data presented subsequently, which is for a young area with little sediment coverage, the only clearly identifiable reflections we find involve the water layer, directly (1W, 2W), or indirectly (2P,etc.). Since strong reflections occur at areas of considerable contrast in elastic properties, e.g. at the interfaces in the model, the lack of reflected energy argues against clearly defined layering in the sub-basement. Because of this experimental evidence, a model based on a continuous velocity/ depth relationship in the crust is more appropriate, although more complex, especially in sedimentary regions.

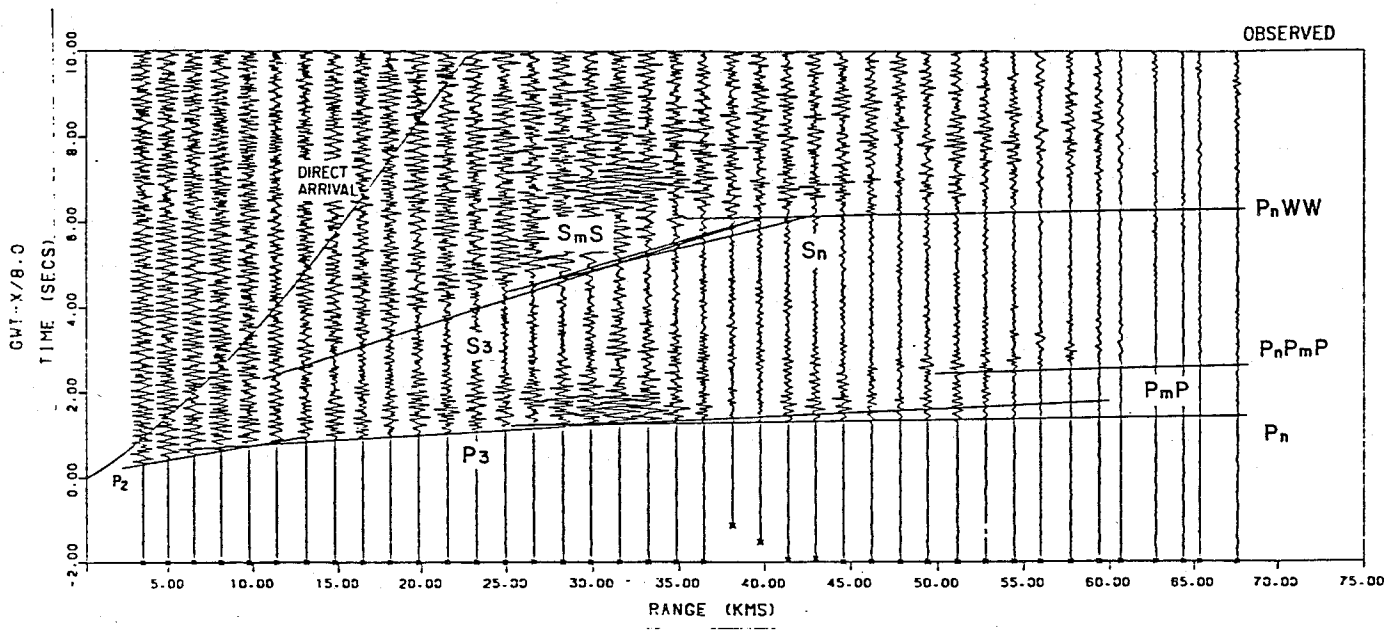

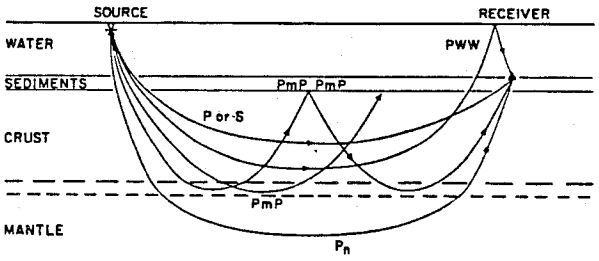

Fig.2-6a
Actual T-X diagram from OBH data obtained near Kane fracture zone.
(from Detrick & Purdy, 1980)

Fig.2-6b
Key to path nomenclature in Fig.2-6a.

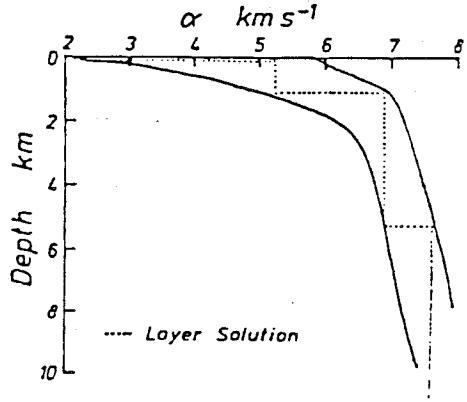

Fig.2-7
Representative bounds on velocity/depth profile
obtained from tau-p method of travel time inversion.
(from Kennett, 1977)

Continuous velocity/ depth profiles

In the analysis of acoustic propagation in regions with continuous velocity gradients, ray theory is the primary tool for analysis. Head wave theory is not applicable. Whereas is a layered model, the horizontal phase velocity of an emerging plane wavefront is equal to the layer velocity, in ray tneory, it is equal to the velocity at which the ray turns upward. This velocity is also the reciprocal of the ray parameter, i.e. 1/p. Knowledge of arrival direction remains important as a tool for remotely obtaining information about velocity structure.

By conceptually allowing layer thicknesses in the multiple layer model to approach zero, we can see that any arbitrary velocity/depth relationship, provided that velocities increase with depth, may be determined from the slopes produced by the first arrival events on a T-X diagram. This is the basis of the Herglotz-Wiechert integrals (Aki, 1980), used for the inversion of travel time versus range data. The density in range with which data is available is of critical importance since the slope of the first arrival changes continuously with offset.

The tau-p method of travel time inversion (Stoffa, Diebold, & Buhl, 1981) assumes a continuous velocity gradient in the crust. Using first arrival times, it produces bounds on possible velocity-depth profiles which are compatible with the data. Many of these resulting profiles are similar to the example in figure 2-7 (Kennett, 1977). Although a continuous gradient is assumed, a consistent feature of these velocity/depth profiles is an area of small velocity change immediately above a sharper gradient at the mantle

interface. This region corresponds to the "classical" layer 3 in Raitt (1963). Averaging from many experiments, this region has a mean compressional speed of 6.8 km/sec, a thickness of about 5 km, and begins at a mean depth of 2 km below basement. We shall see that velocities in this band were the most prevalent at the arrays in the Rose experiment. Rays that travel within this "layer" emerge as first arrivals at offsets of approximately 10 to 30 km in areas where ocean depth is on the order of 3 km. Beyond about 30 km, mantle reflections and mantle interface waves appear as the earliest events.

The model of the oceanic crust we have been employing has evolved from a simple one-interface case to a continuous velocity gradient representation. Although the latter is the most general, we point out that at least the mantle interface and the sea surface can be effectively considered from the simpler, layered model. Reflections from these interfaces are routinely observed in refraction work and the concept of head waves predicts travel times along the mantle interface accurately. In many instances, "layer 3" can also be treated as a homogeneous isovelocity layer.

Amplitude considerations

Since the main focus of this paper centers on energy partitioning in the crust, we now look at some theories concerning head wave amplitude behavior with range (for layered models) and the amplitude behavior of rays, (for the continuous velocity gradient case).

The behavior of head wave amplitude with range is a controversial issue. Cerveny and Ravindra (1971) use a first order ray series solution in solving the equations of motion for a single interface problem in contrast to

the above "zeroeth" order plane wave or geometric optics solution. They obtain an amplitude distance curve for a "pure" head wave that behaves as $L^{-3/2} X^{-1/2}$ where X is the horizontal offset, and $L = (X-X_c)$ is the propagation distance along the interface. According to this equation, at large ranges, amplitude decreases as $1/X^2$ ("spherical spreading").

Alternatively, if we assume a velocity distribution that varies arbitrarily with depth, ray theory predicts that the pressure amplitudes will behave with distance as:

$$p^2 = \frac{P_o^2 R_o^2 \Delta\theta}{hX} \frac{c}{c_o} \left| \frac{\sin\theta_o}{\sin\theta} \right| \qquad (2\text{-}6)$$

(from Clay & Medwin (1977))

R_o is the reference range where sound speed is c_o. θ_o is the initial angle of a ray bundle of width $\Delta\theta$ and amplitude P_o. θ is the average angle of the bundle, with vertical height h, at horizontal range X where average sound speed is c (see fig. 2-8). This equation is valid at ranges where focusing of the ray bundle does not occur, so that θ closely approximates the angle of all rays in the bundle at X. For a source at the surface of an isovelocity layer lying above a half-space with a linear sound speed gradient with slope $\frac{dc(z)}{dz} = b$, the equation for the mean square pressure at the surface at offset X reduces to:

$$p^2 \approx \frac{b R_o^2 P_o^2}{4 c_o X} \qquad (2\text{-}7)$$

Rays will behave with an X^{-1} amplitude dependence for a linear gradient. This type of geometrical behavior is termed "cylindrical spreading" and is also

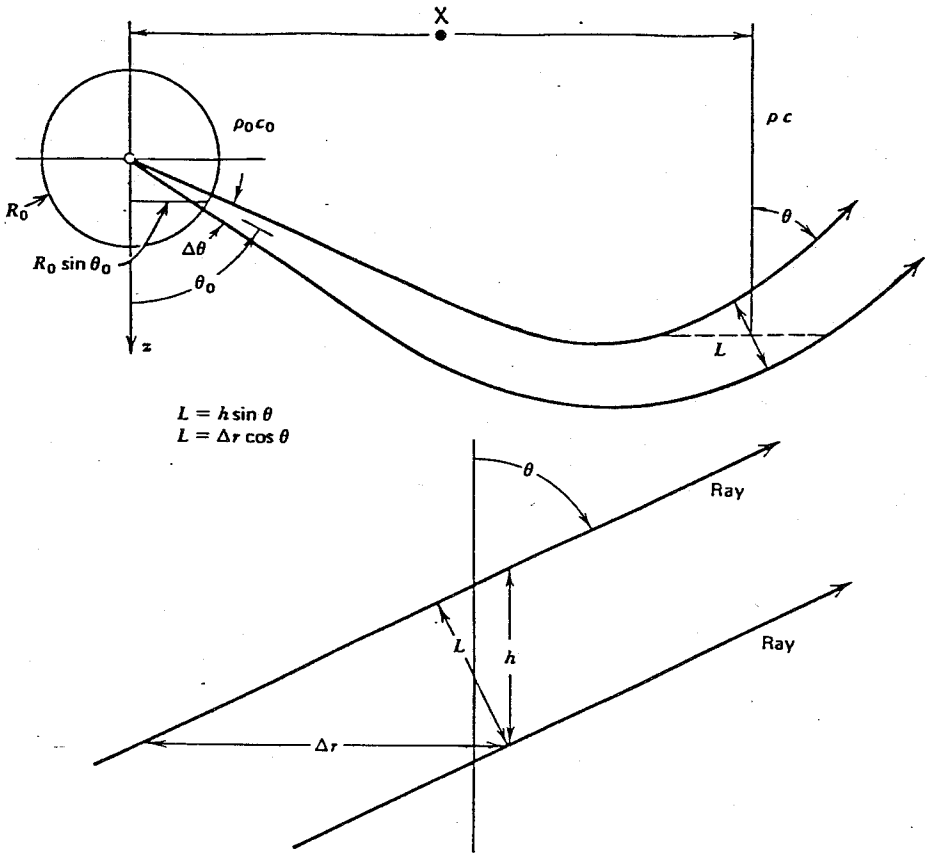

Fig.2-8
Geometry used for calculation of pressure amplitude behavior with horizontal offset in medium with arbitrary velocity/depth profile. (from Clay & Medwin, 1977)

discussed in Kennett (1977) specifically with regard to crustal acoustics. We subsequently see that TL calculations done on the ROSE data yield results which suggest an amplitude attenuation that increases somewhat faster than the X^{-2} dependence. This is probably due to geometrical losses of the types discussed discussed above, coupled with absorption losses in the crust.

We have mentioned that at an approximate offset of 30 km, energy which has interacted with the mantle overtakes "layer 3" energy as the earliest event. Ray bundles with different parameters, p, appear at the same offset and interact to produce a "focusing" effect, so the measured transmission loss at these ranges will be low. Although TL may obey a cylindrical or spherical relationship with respect to range from an overall point of view, fine scale behavior can depart from the general trend at certain offsets. The effects on TL at the 30 km offset will be shown in Chapter 5.

Although the ROSE data to be presented was not sampled with sufficient density for a detailed crustal velocity analysis, events from "layer 3" and the mantle interface are observed with the use of the velocity analysis routine. With the MLM algorithm, events occuring after the first arrival were also identifiable. We report on these results following a description of the ROSE experiment and a discussion of the analysis algorithm.

CHAPTER III

THE ROSE DATA SET

The Rivera Ocean Seismic Experiment (ROSE) was a large seismic/acoustic program involving ten oceanographic institutions and Navy Laboratories. Originally planned to be sited near the Rivera Fracture Zone, it was relocated to an area north of the Clipperton Fracture Zone because of difficulty in obtaining permission to operate in Mexican territorial waters. The experiment took place in the first two months of 1979. Figure 3-1 shows the general area of the experiment, and Fig. 3-2 maps the locations of some of the instruments deployed with respect to the East Pacific Rise central anomaly. Seventy ocean bottom seismometers, a 12 channel vertical array (MABS), and a 24 channel towed array were used in conjunction with explosive sources ranging in weight from .1 to 1000 kg. Five research vessels were involved in the project. The experiment was designed to study the following problems:

1) structure and evolution of young oceanic crust,

2) structure and dynamics of the East Pacific Rise,

3) structure and dynamics of the Orozco fracture zone,

4) long and short range propagation of low frequency acoustic energy,

5) partitioning of energy transmission between the ocean volume and the crust/lithosphere.

To investigate these problems, the experiment was divided into two phases. Phase I consisted of an active program of shooting explosives to

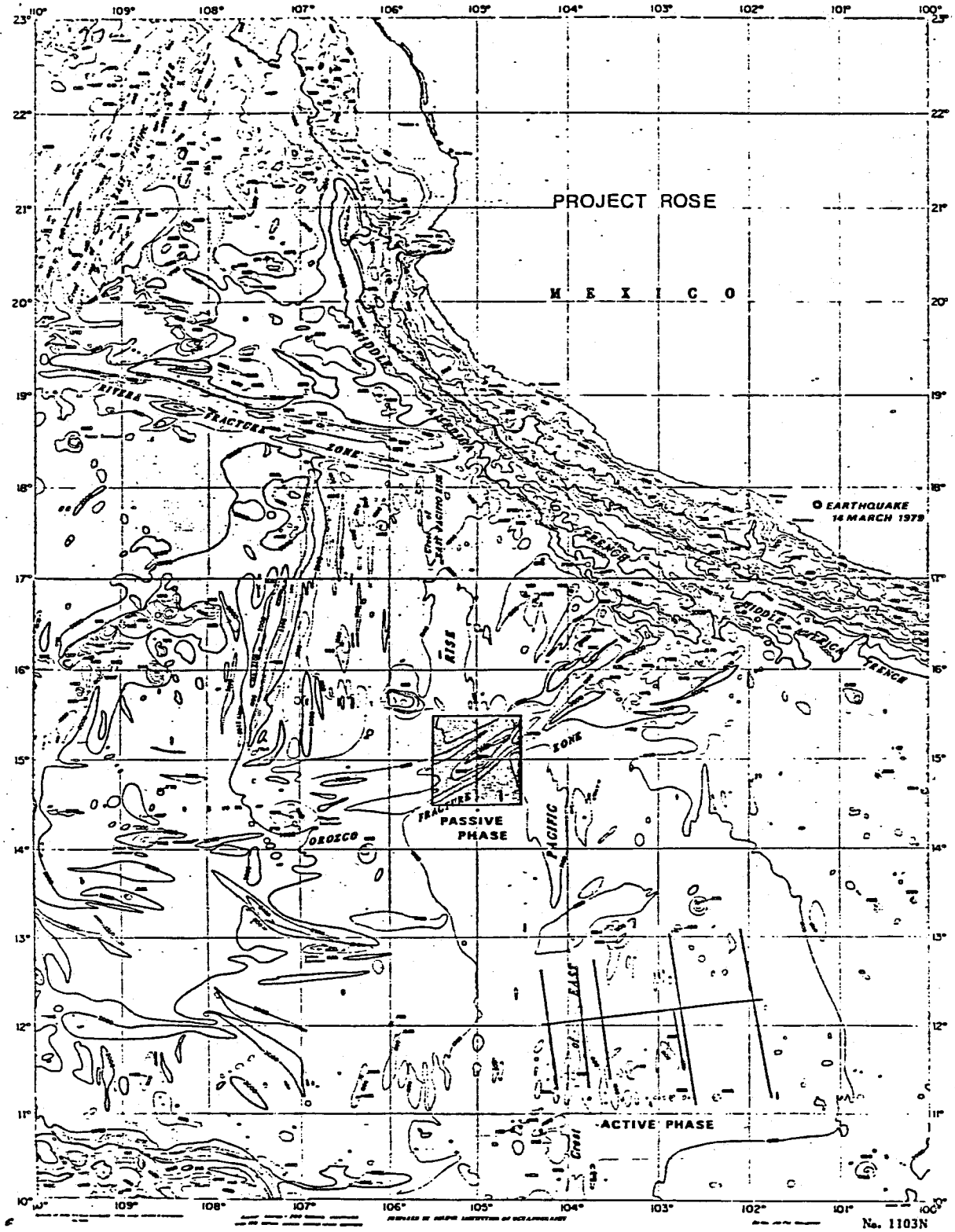

Fig.3-1
Location of ROSE project active and passive phase experiments.

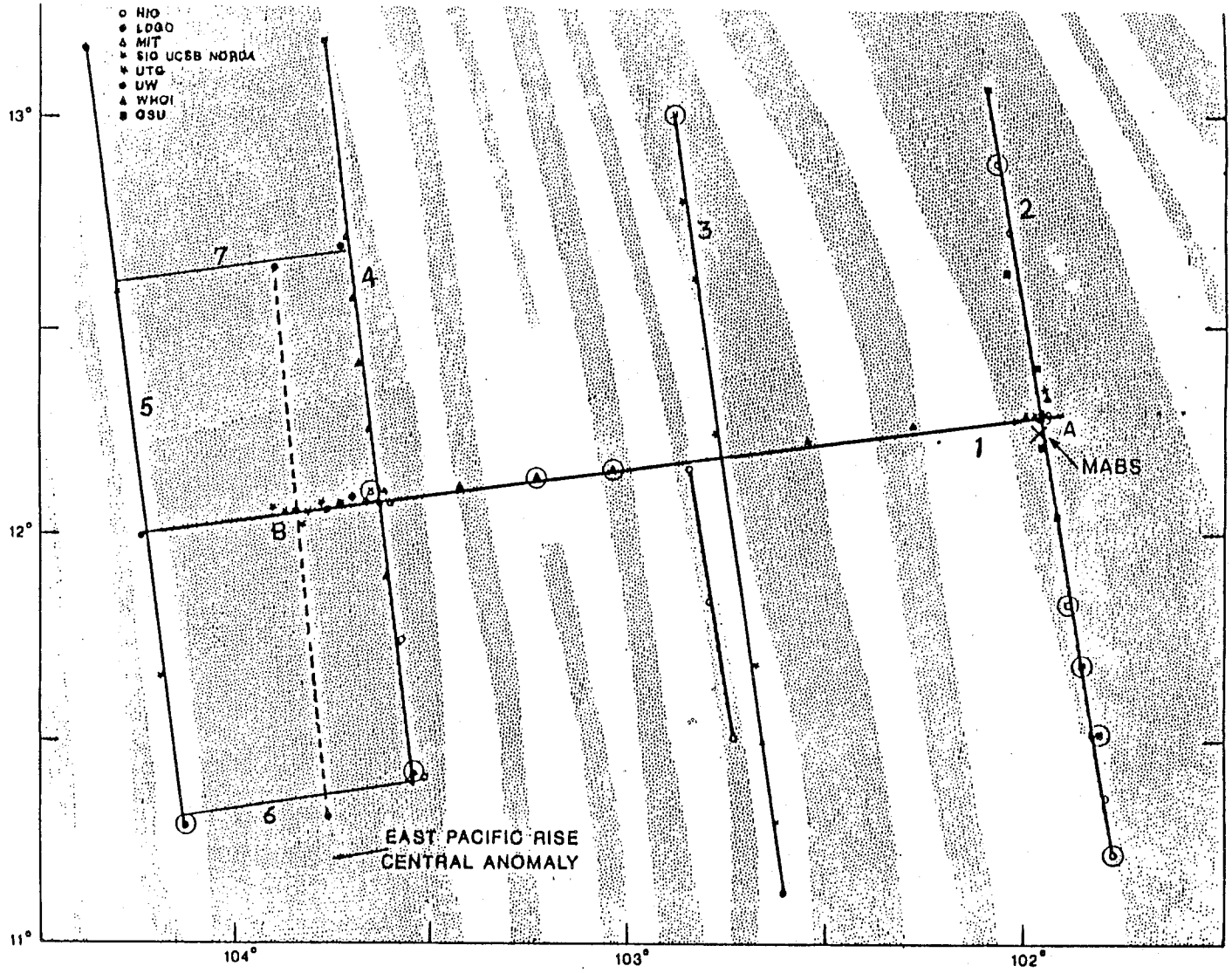

Fig.3-2
Location of vertical (MABS) array and ocean bottom receivers in active phase of ROSE experiment.

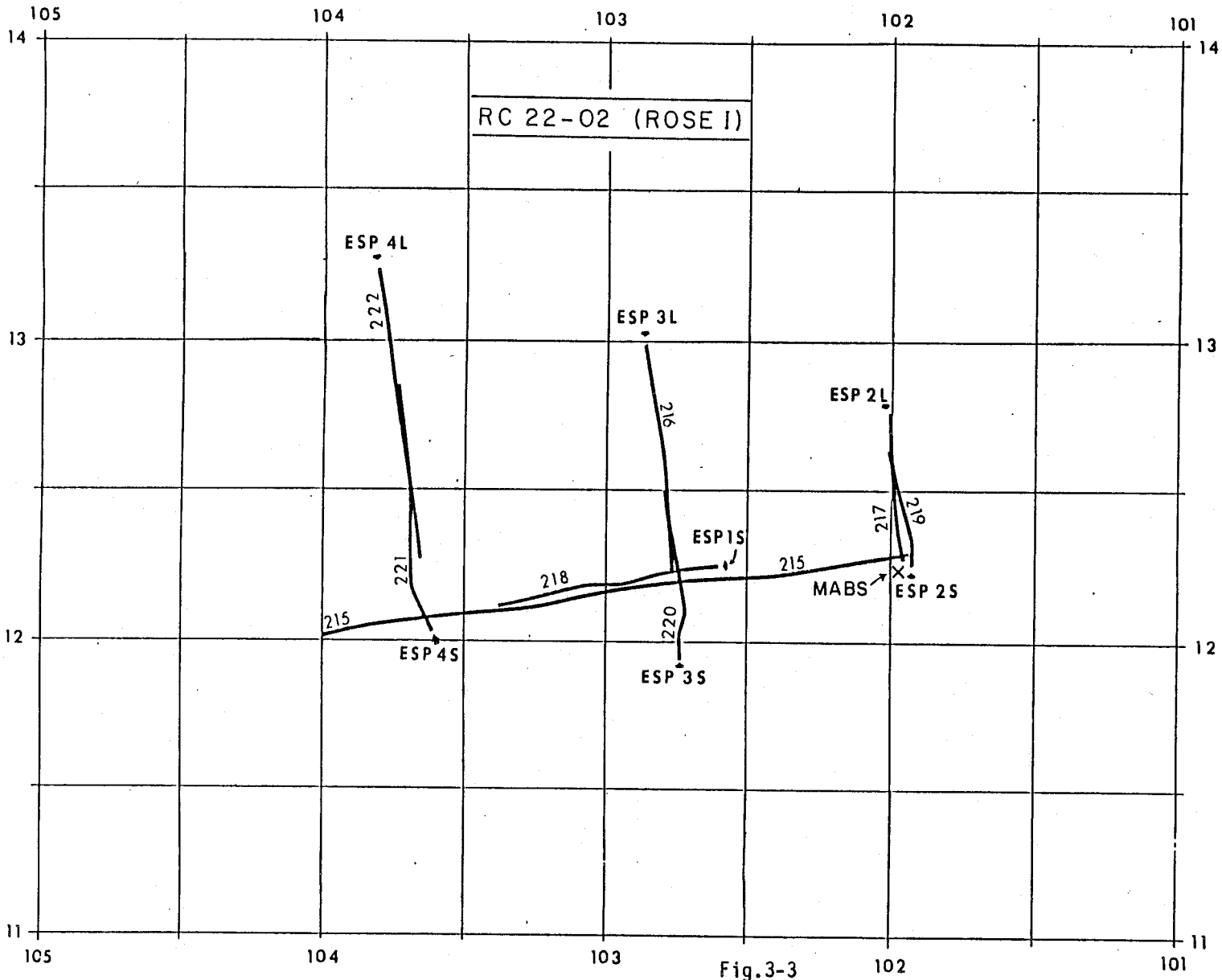

Fig.3-3
Location of ESP lines using horizontal array.

the bottom instruments and to the acoustic arrays. Phase II was primarily a passive earthquake listening experiment with some calibration shots. At Woods Hole, Dr. G. Michael Purdy has been involved with processing and interpreting our OBS data, while Kenneth Prada, Thomas O'Brien, and David Gever of the Signal Processing Group have received and worked on data from the ESP experiments that were recorded on both the vertical (MABS) and horizontal (ESP) arrays. Figure 3-3 shows the tracks of the ESP lines that were shot, and the location of the MABS array. Each ESP line was a two-ship experiment with the shooting and receiving vessels steaming away from each other and from a common midpoint. Figure 3-4 is a schematic of the shooting schedule used in each of the lines. We have been primarily concerned with lines 2L and 2S, in which the midpoint of the ship tracks was in the near vicinity of the MABS array.

The Vertical Array (MABS)

The configuration of the 12 channel vertical array is shown in Fig. 3-5. The data tapes were recorded in analog form and a few transcription difficulties were encountered. The MABS required high amplifier gains for faithfully recording weak refracted arrivals. The subsequent 1W arrivals were then of sufficient strength to saturate the analog recorders, with their limited dynamic range. Our analysis of the MABS data therefore was confined to the ("refracted") arrivals that appear before overload. Also, hydrophones 5,7, and 11 only worked intermittently, while the deepest sensor, 12, did not function at all. Digitization of the data was necessary for use in the

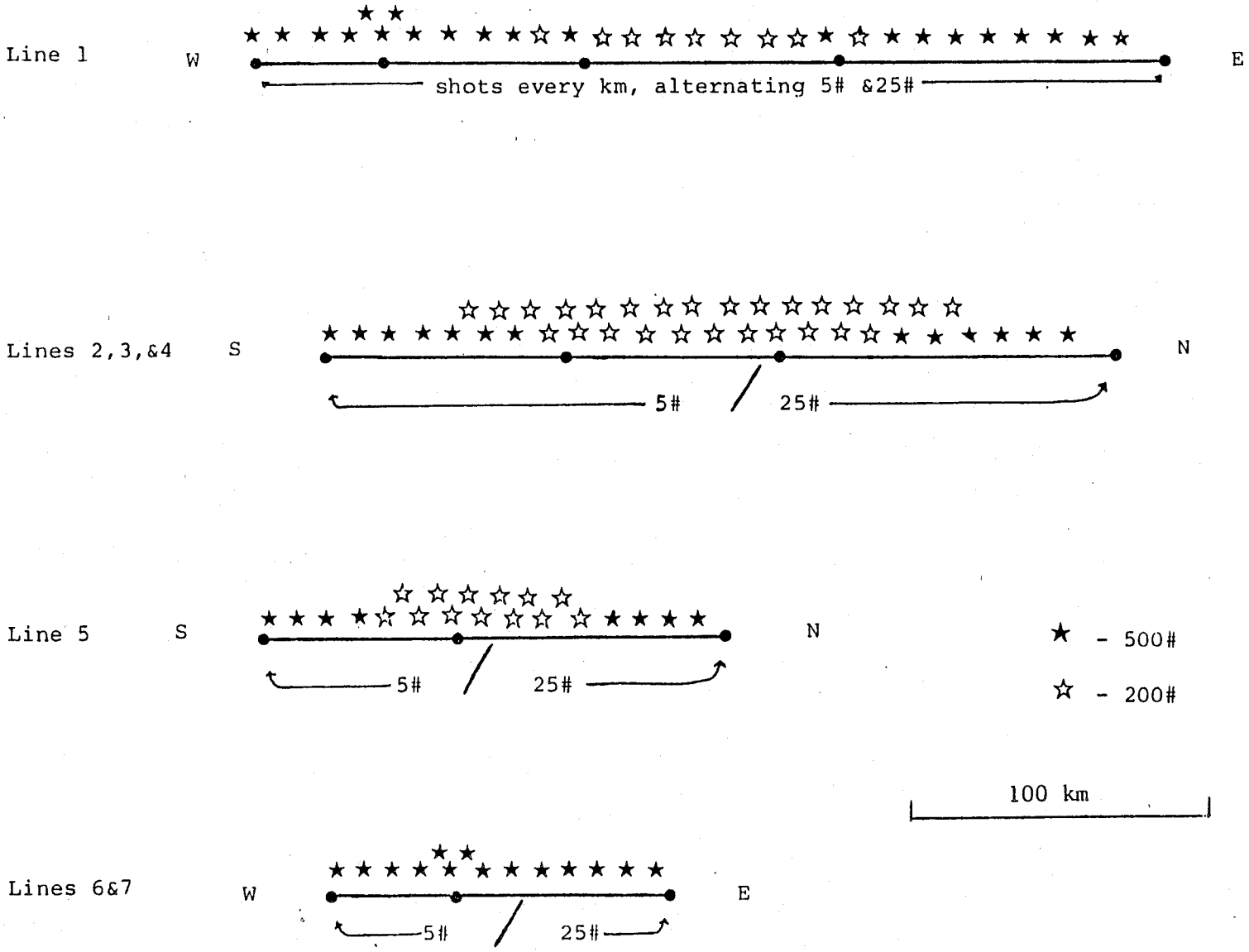

Fig.3-4
Shooting schedule for ESP lines in ROSE experiment.

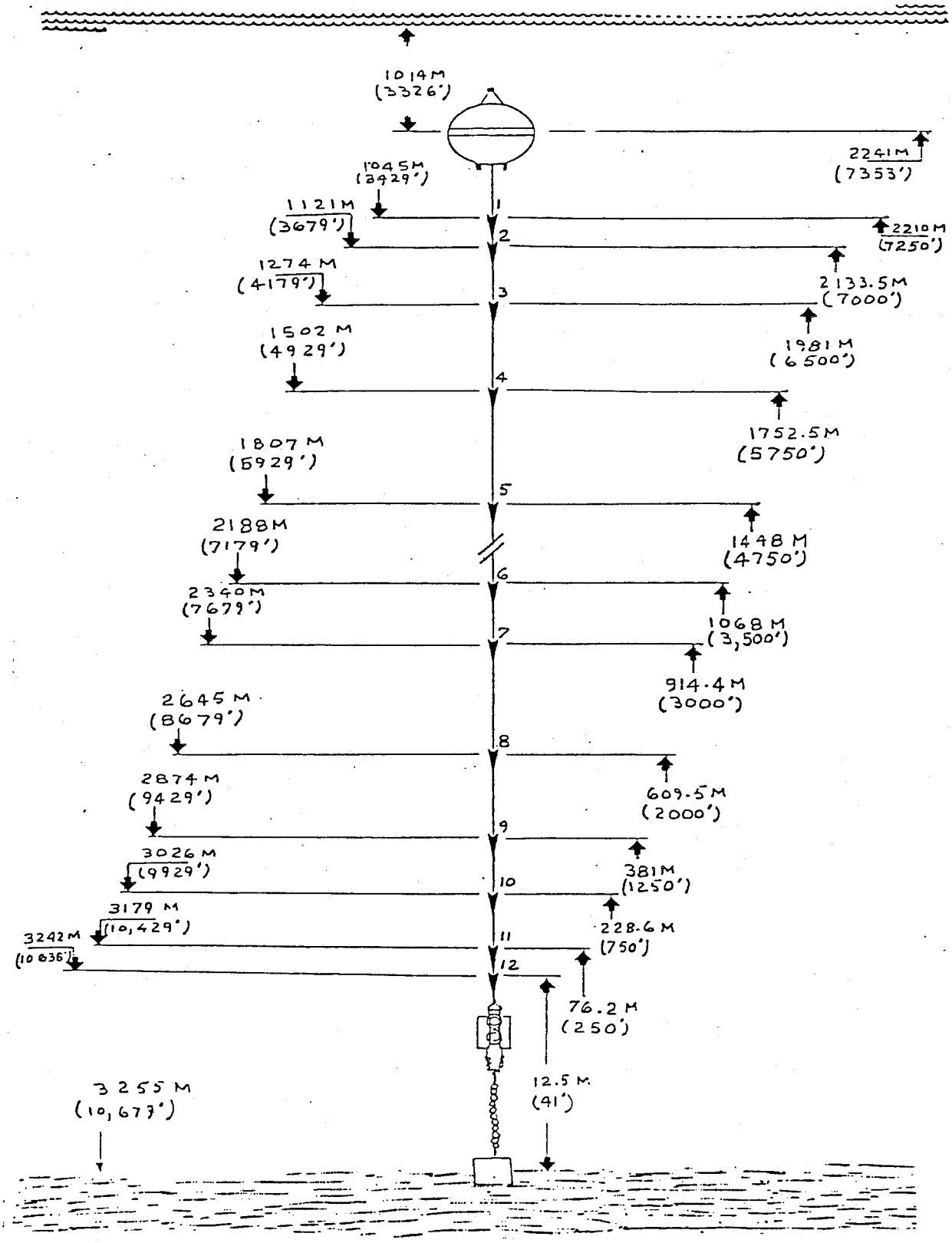

Fig.3-5
Geometry of MABS array during shooting of ESP line 2S.

velocity analysis programs. Using an analog tape recorder, the MABS tapes tapes were played back to the WHOI digital seismic acquisition system (Prada et al, 1974). Due to problems involving the synchronization of the analog tape speed, the recorded time codes on the analog tapes, and the resulting time information on the digitized tape headers, preliminary velocity analysis for MABS data had to be based on relative times calculated from direct water arrivals and the possibly inaccurate vessel positions of the ship logs. This navigation information was based mainly on a SATNAV system which, because of low latitudes, was only updated on the order of once every 90 minutes in an area of strong ocean currents. Estimated position errors were greater than 1 nautical mile. The output of the acquisition system was in WHOI's 12 channel CANBARX format, and this was translated to ROSE format. The CANBARX format with the 8 good data channels was used in the MLM processing of Line 2S MABS data.

The Horizontal Array (ESP)

Better results were experienced with the towed array. In line 2S, the shooting ship was the University of Hawaii's R/V Kana Keoki. It dropped 5 and 25 lb. charges as it steamed away from the area of the vertical array. Lamont-Doherty's R/V Conrad towed the seismic streamer array. Each active section in this array was 100 meters in length, consisting of two 50 meter hydrophone groups connected in parallel, with no taper. The total length of the array was 2400 meters and all 24 channels of the data were good. The tapes were received in Lamont's digitized field format and were translated to the

CANBARX format for processing with the MLM algorithm. At the time line 2S was received, existing computer memory size limited the processing to the use of only twelve channels of data (see Fig. 3-6). By the time line 2L data arrived, the incorporation of an FPS AP120B array processor and the expansion of the system permitted working with all 24 channels in a faster version of the analysis routine. Data was translated from Lamont to the SEGY format, which has become the standard at WHOI. Unfortunately, there were some problems with the ESP data as well. Surface reflections at low frequencies attenuate arrivals from directions parallel to the streamer, due to the LLoyd mirror effect, so direct water waves cannot be seen with the array processing procedure; however, the water bounce arrivals (1W,2W) can be analysed.

The time information given in the digitized ESP data does not include fractions of a second, so that an error of one second is possible in travel times based on this information. Time estimates based on direct water arrivals were therefore more accurate for both the MABS and the ESP data. This is the procedure usually followed in travel time and range calculations, and is the basis for travel time in some T-X plots presented subsequently. For each ESP shot, 40 seconds of data were sent to WHOI. With this data, estimates for all of line 2S were made. Because of the larger extent of the 2L line (beyond 100 km.), however, water arrivals beyond the range of 78 km. were not available. Travel time estimates were therefore not made for the latter part of 2L.

We have shown that the number of channels of data used in processing ROSE data varied as different situations evolved. The bias in the estimated received energy calculated with the MLM programs is dependent on the number of

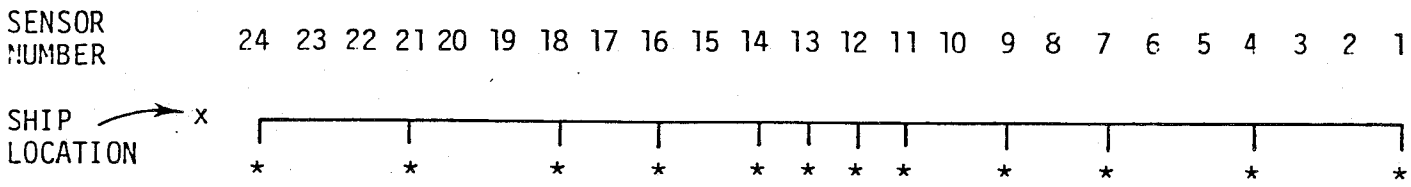

* = SENSORS USED IN TWELVE CHANNEL PROCESSING

SENSOR NUMBER	LOCATION WITH RESPECT TO ORIGIN ON RECEIVING SHIP (meters)
1	2406
2	2306
3	2206
4	2106
5	2006
6	1906
7	1806
8	1706
9	1606
10	1506
11	1406
12	1306
13	1206
14	1106
15	1006
16	906
17	806
18	706
19	606
20	506
21	406
22	306
23	206
24	106

Fig.3-6
24 channel horizontal array geometry and
location of sensors used in 12 channel processing.

channels of data that are used. So that consistent transmission loss estimates would be obtained from sets of ROSE data processed with different array configurations, programs designed for studying MLM bias were run for model arrays with 8, 12, and 24 data channels. These are discussed in Chapter 4, following a description of the MLM algorithm.

CHAPTER IV

FREQUENCY-WAVENUMBER FUNCTION ESTIMATION

This chapter discusses estimation of energy partitioning at the arrays in the ROSE experiment. Waveform characteristics of in situ acoustic sources and paths are not known in detail, so that a received waveform is modelled probabalistically. We define a set of basis functions from the theory of space/time random processes, emphasizing the "frequency/wavenumber" function, $P(f, \underline{\nu})$. This function is based upon a mathematical representation of a spatially homogeneous, temporally stationary random process as a superposition of plane waves, $e^{j2\pi(ft-\underline{\nu}\cdot\underline{x})}$, with temporal frequency f and wavenumber, $\underline{\nu}$. We show that $P(f, \underline{\nu})$ is a measure of the partitioning of energy with f and $\underline{\nu}$, in a process.

In applying random process theory to propagating acoustic waves, a constraint, the "dispersion relation", is imposed upon the relationship of f and $\underline{\nu}$ for plane waves: $|\underline{\nu}| = 1/\lambda = f/c$, where c is the sound speed, and λ the wavelength. The unit vector $\underline{\nu} / |\underline{\nu}|$ is in the direction of propagation. In Chapter II, we discussed the fact that knowledge of the spatial distribution of coherent, propagating energy, having interacted with the crust, can lead to crustal velocity estimates. Given a known source level and a valid crustal model, we also noted that knowledge of the magnitude of energy arriving at a certain spatial angle at a receiver can be used to determine the transmission loss, TL, of the crustal path corresponding to the angle. Specifically, if there is an arbitrary velocity/depth relation in the crust, the vertical angle of a ray, θ, is related to the horizontal phase velocity, c_p, of the

propagating energy at the receiver and to the sound speed in the crust, c_x, at which the ray turns upward:

$$p = \frac{\sin\theta}{c_o} = 1/c_p = 1/c_x \qquad (4\text{-}1)$$

where p is the ray parameter. If the acoustic field in an experiment is modelled as a homogeneous, random process, the estimation of $P(f, \underline{\nu})$ for a range of orientations of the vector, $\underline{\nu} / |\underline{\nu}|$, generates information about the directional character of energy in the field. This is used for crustal velocity estimation. Likewise, the magnitude of the estimated wavenumber function is the basis for TL estimates. However, since impulsive sources are used in most refraction experiments, the received data is not stationary. By employing short segments of data that are treated as samples of a hypothetical stationary process, the concept of the frequency/wavenumber function is made applicable to the ROSE data.

The estimation of the frequency/wavenumber function is done with an array, which essentially measures the apparent phase velocity of coherent waveforms along its geometry. The estimated phase velocity leads to directional information as seen above. From a mathematical viewpoint, the array is treated as a deterministic spatial sampler of random processes: its geometry and temporal frequency response are parameters that can be adjusted to produce a certain "frequency wave-vector response" function, $\mathcal{G}(f, \underline{\nu})$. This function specifies the response of the array to a deterministic plane wave, the design of this response being termed "beamforming". For estimation of $P(f, \underline{\nu})$, the ideal response function will only pass energy in a small spatial angle corresponding to a narrow wavenumber or "spatial frequency"

band, V, and completely reject energy from other areas. The commonly used "conventional" or delay and sum beamformer is first discussed. It is well known that this conventional processor has large sidelobes for sparse arrays with a small number of sensors. An optimal array processor, the MLM beamformer, is then introduced which minimises this sidelobe effect. The output power from this processor is the basis of our estimates of energy partitioning.

Space/Time Random Processes

Stochastic processes for time series have a one-dimensional index set, e.g. t, in x(t). In the array processing problem, the index set may increase to four dimensions as in x(t,x,y,z), or x(t,$\underline{r}$). Most of the concepts involved relate directly back to time series, although the array introduces unique considerations. In particular, for a zero mean, wide sense stationary time series, x(t), that is an input to a pair of ideal linear bandpass filters with responses $H_1(f)$ and $H_2(f)$, as shown in Figure 4-1, the mean square power in the output process, $y_1(t)$, is (from Appendix 4-1):

$$R_y(0) = \mathcal{E}\{y_1^2(t)\} = \int_{f=f_1-W/2}^{f=f_1+W/2} S_x(f)\,df \approx S_x(f_1)\,W \qquad (4\text{-}2)$$

where $\mathcal{E}$ denotes expectation, W is the bandwidth of the filter with center frequency f_1, and $S_x(f)$ is the power spectral density function of the input process:

$$S_x(f) = \int R_x(\tau)\, e^{-j2\pi f\tau}\, d\tau \qquad (4\text{-}3)$$

Since W can be made arbitrarily small, $S_x(f)$ is a measure of the mean square power/unit bandwidth. The cross correlation function of the two output

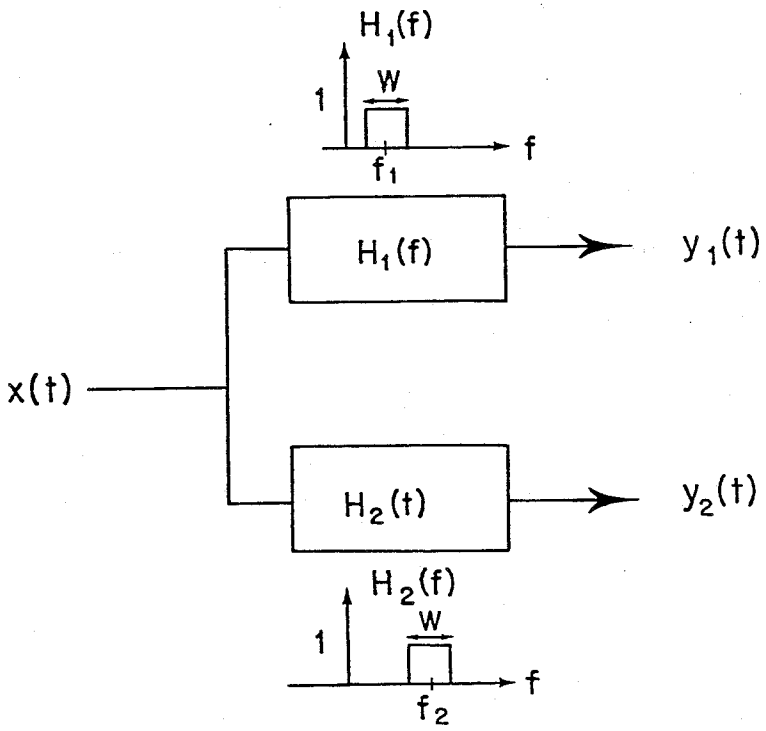

Fig.4-1
Block diagram of time series that is an input to a pair of ideal bandpass filters of width W.

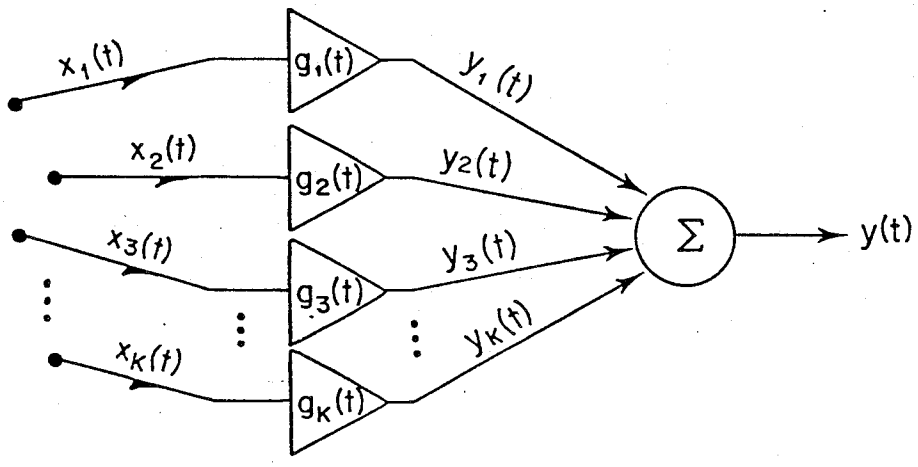

Fig.4-2
A discrete array processor.

processes, $R_{y_1 y_2}(\tau)$, is:

$$R_{y_1 y_2}(\tau) = \int S_{y_1 y_2}(f)\, e^{j 2\pi f \tau}\, df \qquad (4\text{-}4)$$

$$= \int S_x(f) H_1(f) H_2^*(f)\, df \quad \begin{cases} = 0 & \text{if bands are disjoint} \\ \neq 0 & \text{if bands overlap.} \end{cases}$$

Since $y_1(t)$ and $y_2(t)$ are both derived from $x(t)$, this implies that disjoint bands of a stationary times series are statistically uncorrelated. The frequency representation, $(S_x(f))$, provides a powerful and possibly simpler area in which to work with the time series.

We now examine the analog of $S_x(f)$ for space/time random processes. The following functions for a stationary (in time), homogeneous (in space) process, $x(t,\underline{r})$, are defined:

Space/Time Correlation function:

$$R_x(\tau, \Delta\underline{r}) = \mathcal{E}\left\{ x(t,\underline{r})\, x^*(t-\tau, \underline{r}-\Delta\underline{r}) \right\} \qquad (4\text{-}5)$$

Spectral Covariance function:

$$S_x(f, \Delta\underline{r}) = \int d\tau\, R_x(\tau, \Delta\underline{r})\, e^{-j 2\pi f \tau} \qquad (4\text{-}6)$$

Note that, in general, the latter is the cross spectral density function $S_{x_1 x_2}(f)$ for the time series $x_1(t)$ and $x_2(t)$ at $\underline{r}$ and $\underline{r}-\Delta\underline{r}$. If $\Delta\underline{r} = 0$, it is just the spectral density function of the time series at $\underline{r}$.

Frequency/Wavenumber function:

$$P_x(f, \underline{\nu}) = \iiint d\Delta\underline{r}\, S_x(f, \Delta\underline{r})\, e^{j 2\pi \underline{\nu} \cdot \Delta\underline{r}} \qquad (4\text{-}7).$$

where $\underline{\nu}$ is the wavenumber or spatial frequency. The estimation of the frequency/wavenumber function with an array is the object of the MLM algorithm. When based on refraction data, the orientation of $\underline{\nu}$ where the estimate of this function is large indicates the direction of arrival of a

significant event and is used for crustal velocity estimation. This function is defined for stationary, homogeneous space/time processes only. In the analysis of the ROSE data, we model the acoustic field as being short term stationary and homogeneous.

The frequency/wavenumber function is the parallel of the spectral density function in time series. To see this, we next discuss arrays which correspond to the linear filters ($H_1(f)$ and $H_2(f)$) in fig. 4-1.

A discrete array with K sensors at locations $\underline{r}_i$ measuring $x(t,\underline{r}_i)$ is shown in Fig. 4-2. Each sensor is connected to a linear filter $g_i(t)$, and the outputs of all filters are summed to produce the array processor output, y(t):

$$y(t) = \sum_{i=1}^{K} g_i(t) * x(t,\underline{r}_i) \qquad (4\text{-}8).$$

where * is the convolution operation. If x(t) is a simple sinusoidal plane wave of temporal frequency f, and wavevector $\underline{\nu}$: $x(t) = e^{j2\pi(ft-\underline{\nu}\cdot\underline{r})}$, the output y(t) is:

$$y(t) = \left\{ \sum_{i=1}^{K} G_i(f) e^{-j2\pi\underline{\nu}\cdot\underline{r}_i} \right\} e^{j2\pi ft} \triangleq \mathcal{Y}(f,\underline{\nu}) e^{j2\pi ft} \qquad (4\text{-}9)$$

where $G_i(f)$ is the frequency response of the filter at $\underline{r}_i$. The output of the array is just a sinusoid with amplitude and phase determined by $\mathcal{Y}(f,\underline{\nu})$, the <u>frequency/wave vector response function</u> of the array. This is the function that determines the beam pattern of the array.

<u>Delay and Sum Beamformer</u>

If we wish to look in the direction of the unit vector $\underline{\nu}_t/|\underline{\nu}_t|$ for plane waves with speed c, a reasonable impulse response for the linear filters in fig. 4-2 would be:

$$g_i(t) = 1/K\, \delta\left(t - \frac{\underline{\nu}_t\cdot\underline{r}_i}{c|\underline{\nu}_t|}\right) \qquad (4\text{-}10)$$

Only the "correct" plane waves arriving at each $\underline{r}_i$ sum in phase, hence the name "delay and sum beamformer" for this particular processor. The dispersion relation constrains the region in the frequency domain where real plane waves can propagate, and hence the region of interest for the frequency/wavevector response function. Incorporating this relation in eq. 4-9 for the case of the delay and sum beamformer, we obtain the response function:

$$\mathcal{G}(f,\underline{\nu}) = \sum_{i=1}^{K} e^{-j2\pi(\underline{\nu}-\underline{\nu}_s)\cdot\underline{r}_i} \qquad (4\text{-}11)$$

In particular, for an aperture that is a straight line segment of length L, in the direction $\hat{a}_a$, the response function becomes:

$$\mathcal{G}(f,\underline{\nu}) = \text{sinc}\,\frac{\pi L}{\lambda}\left[\cos\theta - \cos\theta_{ta}\right] \qquad (4\text{-}12)$$

where θ_{ta} is the angle between the target and the array directions, and θ is the angle between the actual arriving plane wave and the array. Figures 4.3, 4.4, and 4.5 depict beampatterns for cases in which θ_{ta} is 90° ("broadside"), 45°, and 0° ("endfire"), respectively. Notice that the sidelobes in these figures can pass an appreciable amount of energy coming from directions other than that desired, and that the main lobe can be quite wide, especially at endfire.

Array Response to Random Processes

Having discussed the response of an array to a plane wave, we now look at its behavior in a homogeneous and stationary random space/time field with spectral covariance $S_x(f:\Delta\underline{r})$. For the discrete array in Fig. 4-2, the spectral density function of the output time series, y(t) is (Appendix 4-2):

$$S_y(f) = \sum_i \sum_j G_i(f) G_j^*(f)\, S_x(f, \underline{r}_i - \underline{r}_j) \qquad (4\text{-}13)$$

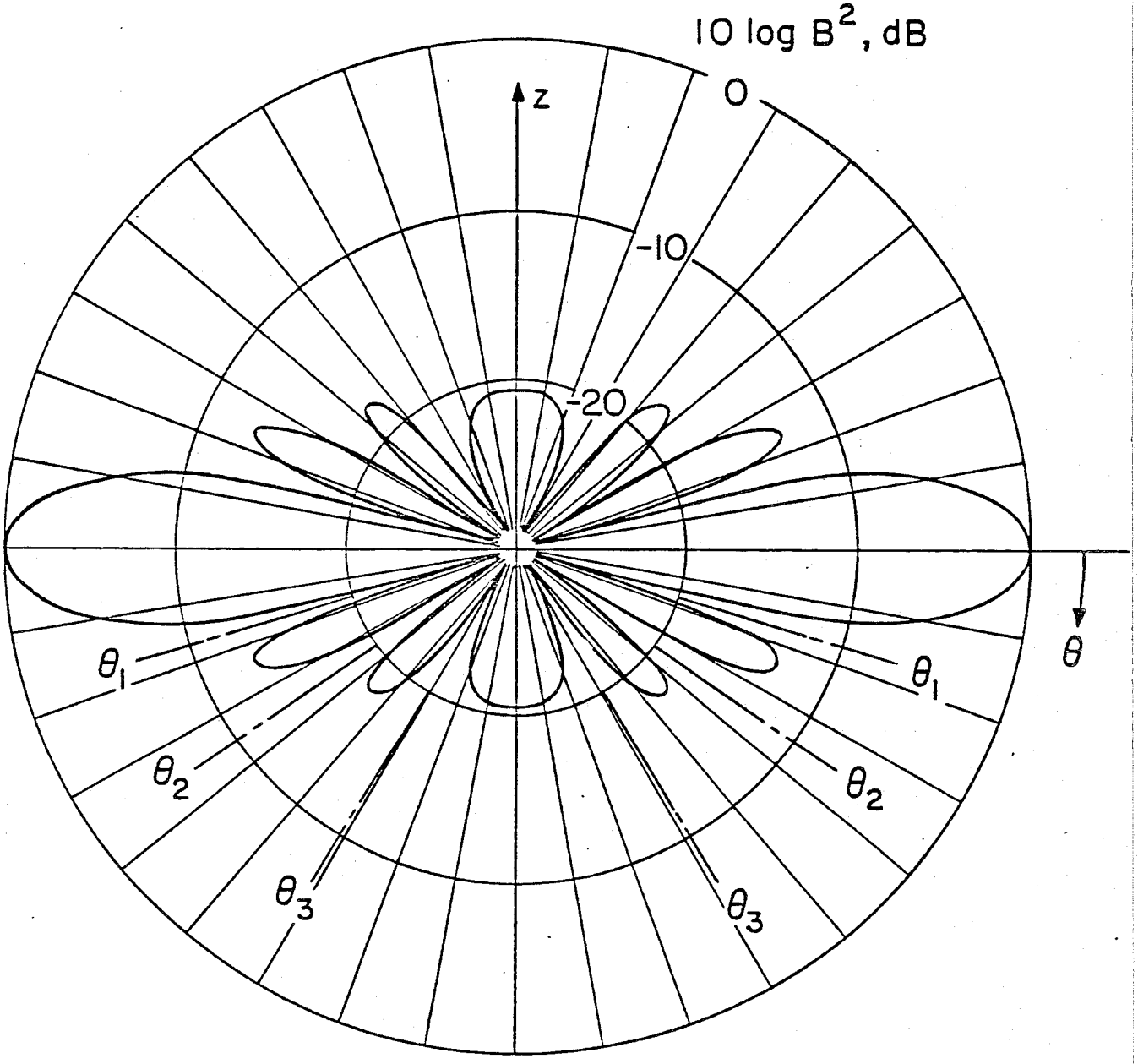

Fig. 4.3 Beam pattern of a uniform line array, $L/\lambda = 3.5$. $\theta_1 = \pm 16.6°$, $\theta_2 = \pm 34.9°$, $\theta_3 = \pm 59.0°$. The pattern is rotationally symmetric about the z axis, (broadside case)

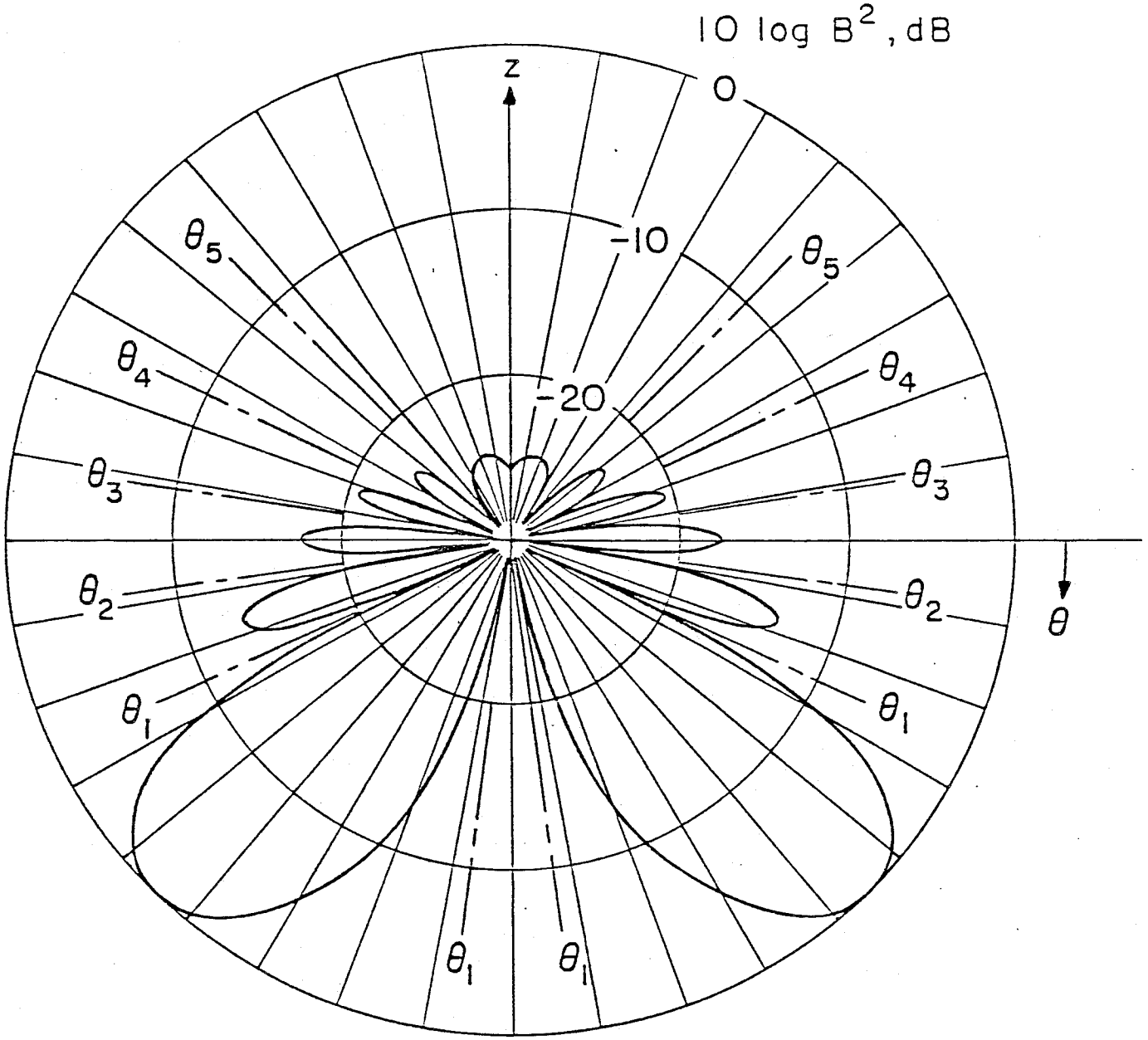

Fig. 4.4 Beam pattern of a line array with uniform amplitude and linear phase-shift, $L/\lambda = 3.5$, $\theta_{ta} = \pi/4$. $\theta_1 = 83.1°$ and $24.9°$, $\theta_2 = 7.8°$, $\theta_3 = -8.6°$, $\theta_4 = -25.8°$, $\theta_5 = -46.2°$. The pattern is rotationally symmetric about the z axis

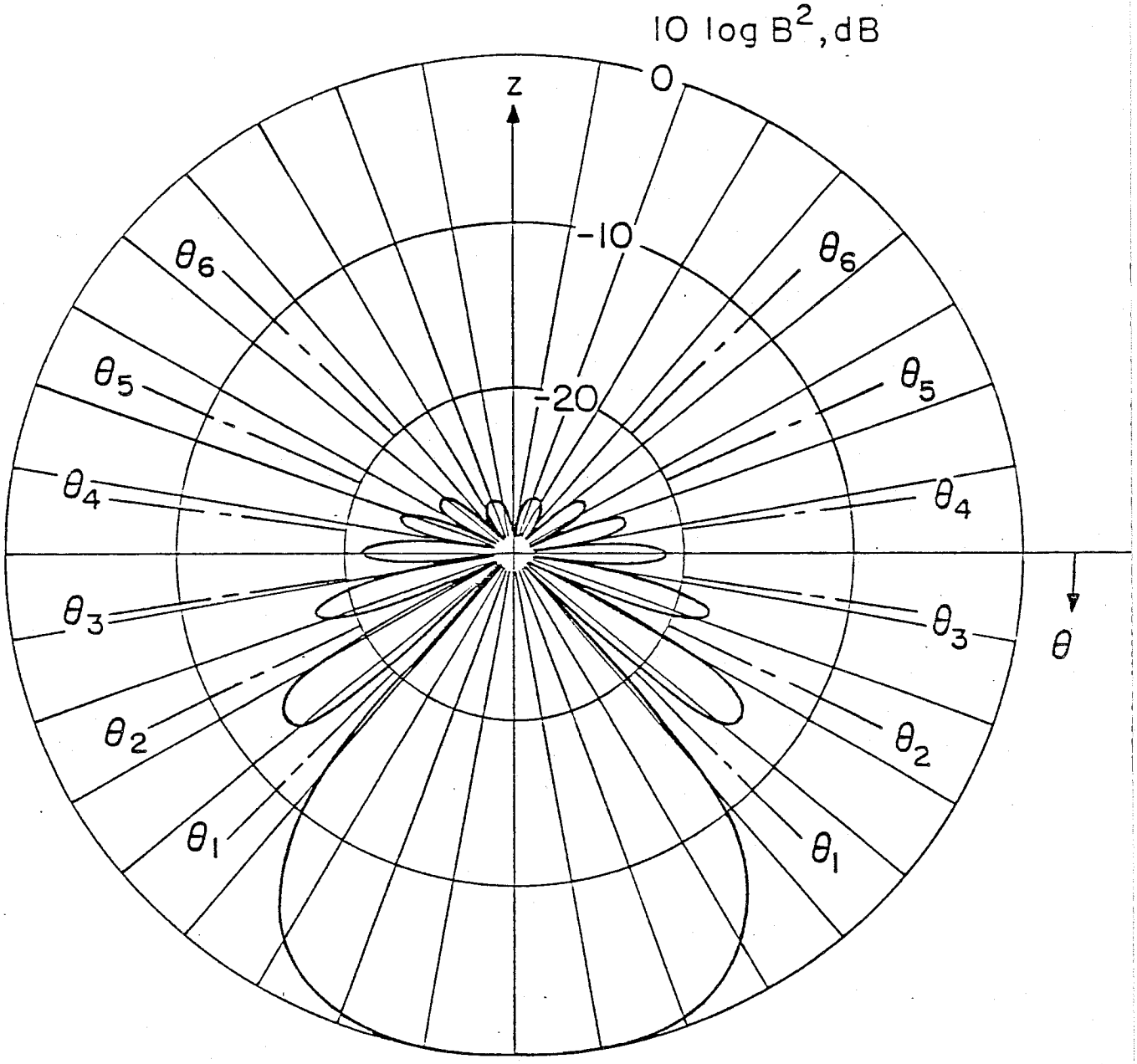

Fig. 4.5 Same array as in Fig. 4.4, but with $\theta_{ta} = \pi/2$.
$\theta_1 = 45.6°$, $\theta_2 = 25.4°$, $\theta_3 = 8.2°$,
$\theta_4 = -8.2°$, $\theta_5 = -25.4°$, $\theta_6 = -45.6°$,
$\theta_7 = -90.0°$ (endfire case)

If we form a vector $\underline{G} = [G_1(f), \ldots, G_K(f)]^T$, and a KxK matrix $[S_{ij}(f)]$, this expression can be written as the quadratic form:

$$S_y(f) = \underline{G}^T [S_{ij}(f)] \underline{G}^* \qquad (4\text{-}14)$$

By expressing the covariance function as the Fourier transform of the frequency/wavenumber function, this can also be expressed as:

$$S_y(f) = \iiint d\underline{v}\, P(f,\underline{v}) \left| \mathcal{Y}(f,\underline{v}) \right|^2 \qquad (4\text{-}15)$$

If $\mathcal{Y}(f, \underline{v})$ is a "pencil beam" response function, having unit magnitude over narrow spatial and temporal frequency bands, V and W, and being zero elsewhere, the array is the counterpart of the ideal bandpass filter in fig. 4-1. This can be seen by evaluating the mean square output power of the processor with this response function:

$$\mathcal{E}\{y^2(t)\} = R_y(0) = \int_W df \iiint_V P_x(f,\underline{v})\, d\underline{v} \qquad (4\text{-}16a)$$

$$\approx P_x(f,\underline{v})\, WV \qquad (4\text{-}16b)$$

This equation is the analog of eq. 4-2 for time series. Conceptually, V and W can be made arbitrarily small so that $P_x(f, \underline{v})$ represents the power per unit spatial and temporal bandwidth for a homogeneous, stationary process. It is the spatial analog of the power spectral density function. For a homogeneous, stationary process, $P(f, \underline{v})$ is a measure of the energy arriving at temporal frequency f, from the direction represented in $\underline{v}$, and it is not influenced by energy arriving from other regions in the frequency domain.

Optimal response function for arbitrary noise

Having discussed the importance of the function $P(f, \underline{v})$, we now turn to the problem of its estimation. From eq. 4-16b, we see that the power at the output of an array processor, with a sufficiently narrow passband with unit

magnitude in temporal and spatial frequency, can be an estimate of $P(f, \underline{v})$. We require a $\mathcal{G}(f, \underline{v})$ that is unity for a desired "target" $\underline{v}_t$, and is minimized in all other frequency regions. In Appendix 4-3, an optimum processor is determined with these specifications for a discrete array of K sensors and an arbitrary stationary process with covariance $S(f, \underline{r}_i - \underline{r}_j) \triangleq S_{ij}(f)$. In matrix notation, the minimised output power density, subject to the constraints mentioned is:

$$S_y(f) = \frac{1}{\underline{E}^T(f, \underline{v}_t)\left[S_{ij}(f)\right]^{-1}\underline{E}^*(f, \underline{v}_t)} \tag{4-17}$$

where the "steering vector" $\underline{E}(f, \underline{v}_t)$ is:

$$\underline{E}(f, \underline{v}_t) = 1/K\left[e^{j2\pi \underline{v}_t \cdot \underline{r}_1}, \ldots, e^{j2\pi \underline{v}_t \cdot \underline{r}_K}\right]^T \tag{4-18}$$

$S_y(f)$ is the estimator for $P(f, \underline{v})$. For a Gaussian space/time process, this is the maximum-liklihood (ML) estimate. The expression in eq. 4-17 is the basis of the MLM algorithm used in the ROSE data analysis. Sidelobe levels and null positions in the optimal $\mathcal{G}(f, \underline{v})$ are adjusted so that noise is optimally attenuated in directions where interference is strong. It is data adaptive in that it requires knowledge of the covariance function $S_{ij}(f)$ of the process that it is operating on. $S_{ij}(f)$ must usually be estimated from the data for each implementation of the estimator, the estimate denoted as $\hat{S}_{ij}(f)$. The MLM estimator for the frequency/ wavenumber function is then:

$$\hat{P}_{MLM}(f, \underline{v}) = \frac{1}{\underline{E}^T(f, \underline{v}_t)\left[\hat{S}_{ij}(f)\right]^{-1}\underline{E}^*(f, \underline{v}_t)} \tag{4-19}$$

We now discuss two examples of mathematical process models for which closed form expressions for the covariance can be written. These examples are used to investigate the behavior of the MLM expression.

Uncorrelated Sensor Noise

Even in situations in which no propagating process exists, with factors such as fluid flow noise, thermal noise, etc, a sensor output is never completely deterministic. A random term, $w(t,\underline{r})$, often considered additive, will be present at each sensor, so that the covariance function of sensor outputs, $w(t,\underline{r})$, is often modelled as:

$$S_w(f, \underline{r}_i - \underline{r}_j) = S_w(f)\,\delta_{ij} \tag{4.20}$$

The notation δ_{ij} signifies that the Kronecker delta is defined at sensor locations only and that noise at $\underline{r}_i$ is independent of noise at $\underline{r}_j$. The process, $w(t,\underline{r})$, is not homogeneous in space and cannot be described by a frequency-wavenumber function. From eq. 4-13, the output density, $S_y(f)$, for an arbitrary array processor in this noise field is just:

$$S_y(f) = \sum_{j=1}^{K} \sum_{k=1}^{K} G_i(f)\, G_j^*(f)\, S_w(f)\, \delta_{ij} \tag{4-21a}$$

$$= \sum_{i=1}^{K} S_w(f)\, |G_i(f)|^2 \tag{4-21b}$$

In Appendix 4-4, the optimal response function for this particular noise process is determined to be:

$$\mathcal{G}(f,\underline{v}) = 1/K \sum_{i=1}^{K} e^{-j2\pi(\underline{v}-\underline{v}_x)\cdot\underline{r}_i} \tag{4-22}$$

This processor is the conventional delay and sum beamformer. It is optimal in this case of spatially uncorrelated sensor noise. The total output power density, and the optimal estimate of $P(f,\underline{v})$, is then:

$$\hat{P}_{MLM}(f,\underline{\nu}) = S_y(f) = \frac{S_w(f)}{K} \qquad (4\text{-}23)$$

In estimating $P(f,\underline{\nu})$ for a mathematical model in which its value for all arguments is undefined, this estimator returns with the noise power, reduced by a factor of K, the "array gain".

If this processor is used as an estimator of $P(f,\underline{\nu}_t)$ in a situation in which the process covariance is arbitrary, the estimate in matrix form can be written as:

$$\hat{P}_{CONV}(f,\underline{\nu}_t) = \underline{E}^T(f,\underline{\nu}_t)\left[\hat{S}_{ij}(f)\right]\underline{E}^*(f,\underline{\nu}_t) \qquad (4\text{-}24)$$

where $\underline{E}(f,\underline{\nu}_t)$ is the steering vector. This expression is often known as the "conventional" estimate of $P_x(f,\underline{\nu}_t)$. Recalling the beampatterns associated with the delay and sum response function in figures 4-3 to 4-5, however, we see that significant energy, from directions other than $\underline{\nu}_t$, is passed in the sidelobes.

Optimal Estimation of Unidirectional Process in Spatially Uncorrelated Noise

The second example of the application of the MLM estimator is a case in which a stationary homogeneous process, $x_o(\cdot)$, propagating from one direction only, $\underline{\nu}_p/|\underline{\nu}_p|$, is added to the model discussed above:

$$x(t,\underline{\ell}) = x_o\left(t - \frac{\underline{\nu}_p\cdot\underline{\ell}}{c\,|\underline{\nu}_p|}\right) + w(t,\underline{\ell}) \qquad (4\text{-}25)$$

This example is particularly important in refraction work, since an arrival is modelled as a windowed sample of this type of random process. Assuming in this case that $S_w(f,\Delta\underline{r}) = \sigma^2\delta_{ij}$, where σ^2 is constant with respect to f ("white noise"), the covariance function of x(t) is:

$$S_x(f,\underline{\ell}_i-\underline{\ell}_j) = P_{x_o}(f)\,e^{-j2\pi\underline{\nu}_p\cdot(\underline{\ell}_i-\underline{\ell}_j)} + \sigma^2\delta_{ij} \qquad ,(4\text{-}26)$$

where $P_{x_o}(f)$ is the power spectrum of $x_o(\cdot)$. It represents the power in the propagating component of the process. In this model, the frequency/wavenumber function, $P(f, \underline{\nu})$ is equal to $P_{x_o}(f)$ at $\underline{\nu} = \underline{\nu}_p$, and is zero elsewhere. We now employ the MLM estimator of $P(f, \underline{\nu})$. For a discrete array, with K sensors, samples of the total covariance function at sensor locations can be written in matrix form as:

$$[\underline{S}_{ij}(f)] = K^2 P_{x_o}(f) \underline{E}^*(f, \underline{\nu}_p) \underline{E}^T(f, \underline{\nu}_p) + \sigma^2 \underline{I} \quad ,(4\text{-}27)$$

where I is the KxK identity matrix, and $\underline{E}(f, \underline{\nu}_p)$ is the steering vector. This covariance matrix can be inverted by using the identity:

$$(A + \underline{u}\underline{v}^T)^{-1} = A^{-1} - A^{-1}\underline{u}\left[I_m + \underline{v}^T A^{-1}\underline{u}\right]^{-1}\underline{v}^T A^{-1} \quad (4\text{-}28)$$

where A is a KxK matrix, $\underline{u}$ and $\underline{v}$ are KxM, and I_m is the MxM identity matrix. We identify A with I, $\underline{E}^*(f, \underline{\nu}_p)$ with $\underline{u}$, and $\underline{E}^T(f, \underline{\nu}_p)$ with $\underline{v}^T$, so that M = 1. If we substitute this into the expression for the optimal MLM estimate at frequencies f and $\underline{\nu}_t$, and recognize that $\underline{E}^T \underline{E}^* = 1/K$, we obtain:

$$\hat{P}_{MLM}(f, \underline{\nu}_t) = \frac{\sigma^2}{K} \frac{1 + \frac{K P_{x_o}(f)}{\sigma^2}}{1 + \frac{K P_{x_o}(f)}{\sigma^2}\left[1 - |\rho|^2\right]} \quad .(4\text{-}29)$$

where:

$$\rho = \frac{1}{K}\underline{E}^T(f, \underline{\nu}_t)\underline{E}^*(f, \underline{\nu}_p) = \frac{1}{K}\sum_{i=1}^{K} e^{j2\pi(\underline{\nu}_t - \underline{\nu}_p)\cdot \underline{\nu}_i} \quad (4\text{-}30)$$

Comparing eq.4-30 with 4-22, we notice that ρ represents the response of the conventional array processor at $\underline{\nu}_p$ when the target is $\underline{\nu}_t$. If $\underline{\nu}_t$ is widely separated from $\underline{\nu}_p$, $\rho \approx 0$, and $P(f, \underline{\nu}_t)$ is just σ^2/K, the estimate we found in a sensor noise field alone. If $\underline{\nu}_t = \underline{\nu}_p$, $\rho = 1$, and we get:

$$\hat{P}_{MLM}(f, \underline{\nu}_p) = P_{x_o}(f) + \sigma^2/K \quad (4\text{-}31)$$

The uncorrelated noise is again reduced by the array gain, K. With this process model, the MLM estimate in the direction of plane wave propagation, results in the correct value, $P_{\kappa_0}(f)$, together with the added noise component reduced by the array gain K. If the noise power, σ^2 can be estimated, by directing the array where no coherent energy is propagating, the value of $P_{\kappa_0}(f)$ follows immediately. This is the procedure used to determine the coherent energy arriving from a particular direction in a refraction experiment, after data is suitably windowed so that this model is approximately valid.

Implementation of the MLM Algorithm

We now present the procedure used in evaluating eq. 4-19 for the ROSE data set. The material discussed to this point is based on a homogeneous, stationary process assumption. Refraction data cannot be modelled as stationary since it changes character with a time constant determined by the source signature. The essential idea behind the implementation is to use the stationary concept we have been discussing over a spatially finite and temporally short analysis window. For an estimate at frequencies f and $\underline{\nu}_t$, we model the data as samples of a random process consisting of a single propagating plane wave at $\underline{\nu}_t$ with added uncorrelated noise, as in the example above. This is usually valid in refraction work if the data segments used are short enough so that only one event, corresponding to a coherent arrival from one specific direction, is fully represented in the windowed data from all sensors. In the implementation, T seconds of data (typically T = 1 sec. in our

application) are used from each channel for an estimation at a certain travel time. For each covariance matrix term, $S_{ij}(f)$, and target direction, $\underline{v}_t / |\underline{v}_t|$, the T seconds are selected for each pair of sensors at points corresponding to the times the hypothetical plane wave would appear at each sensor. The horizontal phase velocity of this wave is related to $\underline{v}_t$ by:

$$c_p = \frac{c_o}{\sin\theta} = \frac{c_o}{\sin\left[\frac{\underline{v}_t}{|\underline{v}_t|} \cdot \hat{i}_z\right]} \qquad (4\text{-}32)$$

where θ is the vertical angle of arrival and $\hat{i}_z$ is a unit vector in the vertical direction. The data within the shaded "windows" in figs. 5.2 are examples of typical segments that would be selected. The traces are received waveforms from 12 of the 24 sensors of the horizontal array in one ROSE experiment. In fig 5.2a, the window at t=2 seconds is almost horizontal, i.e. with little "moveout". Using this data, the estimation procedure models the field as a plane unidirectional process with a relatively high horizontal phase velocity encountering the array almost at broadside. In contrast, in fig. 5-2b, the window shown indicates a relatively larger moveout, so that the segments are considered to be samples in time and space of a plane wave process arriving from a direction closer to endfire.

For the ROSE data, estimates of $P(f, \underline{v})$ were made for vertical target angles of 8° to 90°, and, for ESP experiments, at the azimuthal angle directly behind the receiving ship. In a horizontally layered crustal model, this corresponds to phase and layer velocities of 1.5 to about 10 km/sec. Once T seconds of data, with the proper moveout, is selected for each target, the covariance matrix necessary for evaluating eq. 4-19 is formed. Figure 4-6 is a

block diagram of the procedure used for one matrix term, $S_{ij}(f)$. The segments from sensors i and j are windowed in time with a cosine taper, and fast Fourier transformed (FFT length: N). In the ROSE implementation, the effective data length after windowing is $T \approx .5$ sec. After taking the complex conjugate of the coefficients of the jth sensor, a product is calculated for each coefficient.

To stabilize the covariance estimate at a frequency f, a simple average of the coefficient products over a band of width W Hz centered about f is performed. The frequency region of interest in refraction work extends from near zero to about 20 Hz. Absorption of higher frequency energy at longer ranges sets this upper limit. The bandwidth W must be kept narrow so that frequency selective phenomena within this 20 Hz band can be discerned. The number of significant Fourier components in a band, W, is M = 2WT. With the ROSE data, W was 3 or 4 Hz to maintain a reasonable resolution in frequency. Center frequencies were typically 5, 8, 11, and 14 Hz. Since the selected data is modelled as a unidirectional process in white noise, in keeping with the covariance expression in eq. 4-26, a phase shift: $e^{-j2\pi\nu_k \cdot (\underline{r}_i - \underline{r}_j)}$ is applied to each matrix term to compensate for the moveout. In matrix notation, the estimated covariance matrix is expressed in two forms:

$$\hat{S}(f) = \frac{1}{M} \begin{bmatrix} \underline{x}_1^H \\ \vdots \\ \underline{x}_K^H \end{bmatrix}_w [\underline{x}_1, \ldots, \underline{x}_K]_w \qquad (4\text{-}33a)$$

$$= \frac{1}{M} \sum_{k=1}^{M} \underline{\xi}_k \underline{\xi}_k^H \qquad (4\text{-}33b)$$

where H denotes the conjugate transpose, w expresses the fact that FFT was done on windowed data, K = number of sensors, M = number of frequency

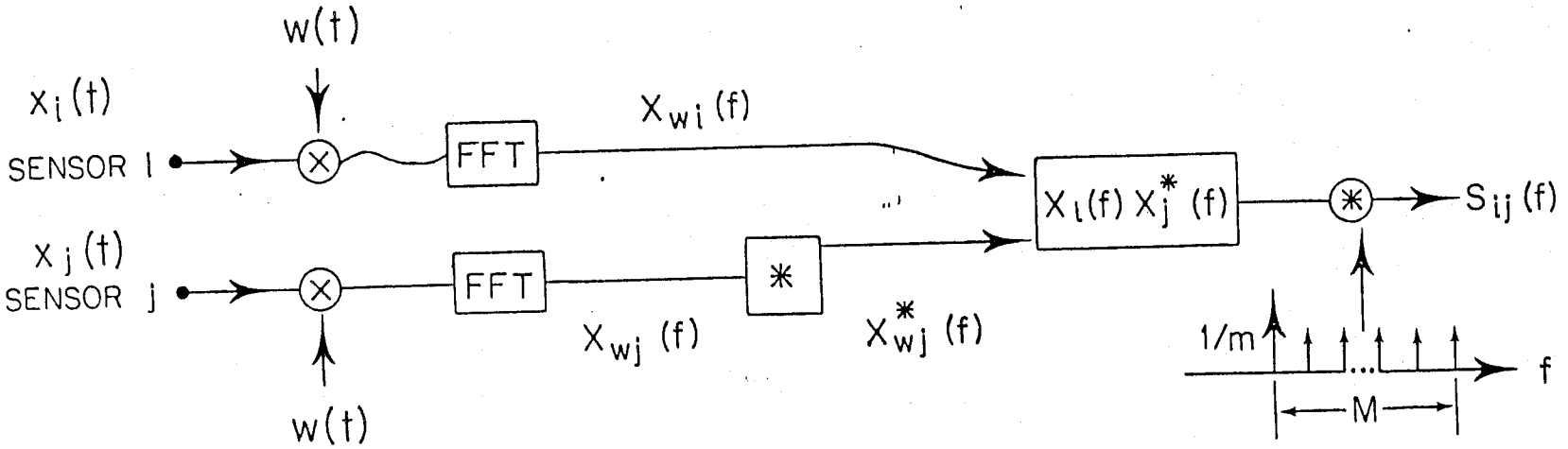

Fig.4-6
Block diagram depicting the formation of one term of the estimated covariance matrix.

components averaged, and:

$$\underline{x}_j^H = \left[X_{wj}^*\left(f-\frac{M/2}{NT}\right), \ldots, X_{wj}^*\left(f-\frac{M/2-k}{NT}\right), \ldots, X_{wj}^*\left(f+\frac{M/2}{NT}\right)\right] e^{j\frac{2\pi f}{c}\underline{r}_j} \quad (4\text{-}34)$$

for sensor j, and:

$$\underline{\xi}_k^H = \left[X_{w1}^*\left(f-\frac{M/2-k}{NT}\right)e^{j\frac{2\pi f}{c}\underline{r}_1}, \ldots, X_{wK}^*\left(f-\frac{M/2-k}{NT}\right)e^{j\frac{2\pi f}{c}\underline{r}_K}\right] \quad (4\text{-}35)$$

for the kth frequency coefficient in W.

The term in (4-43a) expresses the KxK $\hat{S}(f)$ matrix as a product of a KxM and its transpose. The maximal rank of S(f) must then be the lesser of M or K. Thus if M< K, the matrix will not be of full rank and will not be invertible so that eq. 4-19 cannot be implemented. Since narrow bandwidths were desired, this was the case in all the ROSE experiments processed. We now discuss the steps that were necessary so that the MLM expression could still be evaluated with S(f) less than full rank.

A third, algebraic, expression for the estimated covariance matrix term (i,j) is:

$$\hat{S}(i,j) = \frac{1}{M}\sum_{k=1}^{M} X_i(k)X_j^*(k)e^{j[\phi(i,k)-\phi(j,k)]} \quad (4\text{-}33c)$$

where M is the number of frequency components and ϕ (i,j) is the phase shift due to moveout at sensor i, frequency k. In the implementation, the matrix is normalized:

$$\hat{S}_{NORM}(i,j) = \frac{\hat{S}(i,j)}{\sqrt{\hat{S}(i,i)\ \hat{S}(j,j)}} \quad (4\text{-}36)$$

and the geometric mean, CVAV, of the original diagonal elements calculated so that the levels can be restored afterward:

$$CVAV = \sqrt[K]{\hat{S}(1,1)\ \hat{S}(2,2)\ldots\ \hat{S}(K,K)} \quad (4\text{-}37)$$

Experimentally, this scaling and normalization produced better results, making $\hat{P}(f, \underline{\nu})$ estimates less sensitive to varying gains in the sensor electronics. The diagonal elements of the normalized matrix $\hat{S}_{NORM}(i,j)$, which is still singular if $M < K$, are unity. A pseudo-inverse of the matrix is formed by adding a small term, γ, to all "ones" on the diagonal and then inverting. The addition of this term to the normalized matrix made it possible to add the same relative amount of artificial noise to matrices estimated from data with varying levels of energy. In practice, γ ranged from .01 to .04.

Following the calculation of steering vectors, $\underline{E}(f, \underline{\nu}_t)$ for each $\underline{\nu}_t$ desired, the MLM expression, eq, 4-18, is evaluated. After restoring levels with CVAV, the resulting estimate can be written as:

$$\hat{P}(f,\underline{\nu}) = \frac{CVAV}{\sum_{i=1}^{K}\sum_{j=1}^{K} E^{*}(i,\underline{\nu}_t)\, Q(i,j)\, E(j,\underline{\nu}_t)} \qquad (4\text{-}38)$$

where Q(i,j) is the (i,j) term of the inverse of the matrix with (i,j) term:

$$\hat{S}_{NORM}(i,j) + \gamma\,\delta_{ij} \qquad (4\text{-}39)$$

MLM Bias

The MLM expression, eq. 4-19, produces an estimate of the coherent energy across the array (P) together with a reduction by K of the measured incoherent energy for the random process upon which the ROSE data is modelled. The estimator is well behaved. We have just shown, however, that the actual implementation of the MLM used does not follow eq. 4-19 exactly. Since estimates of energy partitioning use both the directional and amplitude

information in $P(f, \underline{\ell})$, it is important that the estimated magnitude be accurate. A bias problem can appear because of the following:

1) As we have described, the covariance of the process is estimated from the data itself, collected in a finite duration of time and over a spatially limited extent. We never know the actual covariance of a process appearing at an array. The MLM estimate using this "covariance" is biased.

2) The covariance matrix in many situations may turn out to be singular and not invertible, as with the ROSE data. With the addition of "white noise" terms on the diagonal of the matrix so that a pseudoinverse can be formed, the behavior of the actual estimator does not lend itself to analysis as easily as eq. 4-19.

Capon and Goodman Bias Expression

We return to the second expression for the initial covariance estimate, eq. 4-33b, before artificial diagonal terms are added. From a probabalistic viewpoint, this equation is recognized as the sample mean estimate of the expectation: $[S_{ij}(f)] = \mathcal{E}\{\underline{\underline{\xi}}\,\underline{\underline{\xi}}^{H}\}$,i.e. the covariance matrix of a K-variate random vector $\underline{\underline{\xi}}$. Let the vector $\underline{\underline{\xi}}$ be zero mean, complex Gaussian and let sample vectors $\underline{\underline{\xi}}_{\ell\ell}$ be normally distributed also, with independent components for different frequencies. In this case, there are M independent, identically distributed vector terms in the sample mean. Goodman (1963) shows that, under these conditions, the joint distribution of all real and imaginary components of $\hat{MS}(f)$ has a complex Wishart density function designated as: CW(M,K, S(f)), if the matrix is of full rank (M >K).

For a scalar b with density CW(M,1,1), the distribution is identical to that of a chi-square variable with the degree of freedom parameter equal to 2M. Thus:

$$\mathcal{E}\{b\} = \mathrm{var}\{b\} = M \qquad \text{for b CW(M,1,1)} \quad (4\text{-}40)$$

Capon (1970) shows that the quantities:

$$b_1 = \frac{M\hat{P}_1(f,\underline{\nu})}{\underline{E}^T(f,\underline{\nu})[S_{ij}(f)]\underline{E}^*(f,\underline{\nu})} \qquad \text{is CW(M,1,1)} \quad (4\text{-}41)$$

and

$$b_2 = \frac{M\hat{P}_2(f,\underline{\nu})}{\left[\underline{E}^T(f,\underline{\nu})[S_{ij}(f,\underline{\nu})]^{-1}\underline{E}^*(f,\underline{\nu})\right]^{-1}} \qquad \text{is CW(M-K+1,1,1)} \quad (4\text{-}42)$$

where $\underline{E}(f, \underline{\nu})$ are the steering vectors defined in Appendix 4-3, and $P_1(f, \underline{\nu}) = \underline{E}^T[\hat{S}_{ij}(f)]\underline{E}^*$ and $P_2(f, \underline{\nu}) = \left[\underline{E}^T[\hat{S}_{ij}(f)]^{-1}\underline{E}^*\right]^{-1}$, are the conventional and MLM estimators, respectively. Rearranging and taking expectations, we obtain:

$$\mathcal{E}\{\hat{P}_1(f,\underline{\nu})\} = \frac{1}{M}\mathcal{E}\{b_1\}\underline{E}^T[S_{ij}(f)]\underline{E}^* = \underline{E}^T[S_{ij}(f)]\underline{E}^* \quad (4\text{-}43)$$

for the conventional estimate, and:

$$\mathcal{E}\{\hat{P}_2(f,\underline{\nu})\} = \frac{1}{M}\mathcal{E}\{b_2\}\left[\underline{E}^T[S_{ij}(f)]^{-1}\underline{E}^*\right]^{-1} = \frac{M-K+1}{M}\left[\underline{E}^T[S_{ij}(f)]^{-1}\underline{E}^*\right]^{-1} \quad (4\text{-}44)$$

for the MLM estimate. Even if the covariance matrix has full rank, there is a bias term: $\frac{M-K+1}{M}$ in the MLM estimate due to the fact that we use a windowed estimate of the actual covariance. Although this bias term is tractable, two facts make it unsuitable for the present use, except as a point of reference:

i) For $M < K$, the expression loses its validity. Even for $K = 8$ sensors, as in the MABS array, the bias expression above is meaningless, since $M = 3$ or 4. Also, as we have mentioned, the resultant covariance estimate is not directly invertible.

ii) The bias term is based on the assumption that the terms in the sample vectors, $\underline{\underline{\Sigma}}_{ik}$, are normally distributed and independent in frequency. Appendix 4-5 outlines a calculation of the correlation function of two components of these vectors: $\mathcal{E}\{X_{i\omega}(f_1) X_{j\omega}^*(f_2)\}$, with the result that:

$$R_{X_{i\omega}(f) X_{j\omega}(f)}(f_1 - f_2) = \begin{cases} 0 & |f_1 - f_2| > BW \\ S_{x_i x_j}(f_1) \int_{-\infty}^{\infty} d\nu\, W(\nu)^* W(\nu - (f_1 - f_2)) & |f_1 - f_2| < BW \\ S_{x_i x_j}(f_1) \int_{-\infty}^{\infty} |W(\nu)|^2 d\nu & f_1 = f_2 \end{cases} \quad (4\text{-}45).$$

The components $X_{i\omega}(f_1)$ and $X_{j\omega}(f_2)$ are uncorrelated only if they are separated by an interval larger than BW, the effective bandwidth of the window function used to reduce the variance of our estimate. For a 1 second cosine window, as implemented with ROSE data, BW is on the order of 2.5 Hz., but for T=1 second, coefficients are spaced at about 1 Hz. Because of the short data segments that must be used with refraction data, the frequency components are therefore correlated. The bias expression due to Capon and Goodman is not valid. We can estimate that the effective number of degrees of freedom of the chi-square variables b_1 and b_2 in Eq. 4-41 and 4-42, is reduced from the full 2M because of this, so that the "M" term in the bias expression is effectively decreased.

Model Program

We have shown that Capon's expression for MLM bias cannot be used with the ROSE data. Although we can speculate on the effect of correlated vectors, $\underline{\xi}_k$, no analytic results are available for this or, particularly, for the effect of the artificial diagonal terms, γ, added to the covariance matrix. To study the influence on MLM bias by the added artificial noise, a Monte Carlo simulation was done. For any given array geometry specified by the user, an MLM estimate was computed that was based on the process model consisting of a sinusoidal plane wave of amplitude $\sqrt{P}$ and random phase, together with additive, normally distributed, spatially independent noise. The Fourier component at sensor i and frequency k is modelled as:

$$X(i,k) = W(i,k) + \sqrt{P}\, e^{j[\zeta(k) - \phi(i,k)]} \qquad (4\text{-}46)$$

where: ζ (i) is the random phase term from a number generator with a flat distribution from 0 to 2π.

W(i,k) is the complex "sensor noise" term generated with a zero mean Gaussian distribution with variance σ^2.

ϕ(i,k) is the moveout phase shift.

The bandwidth W and number of coefficients (M) in the band are chosen so that, upon averaging, the i,j term in the simulated covariance matrix is:

$$S_{ij}(k) = 1/M \sum_{k=1}^{M} X(i,k)\, X^*(j,k) \qquad (4\text{-}47)$$

This expression is similar to the corresponding term in the actual implementation (eq. 4-33c). In practice, M ranged from 1 to 76 coefficients with special attention given to trials with M=3 or 4, numbers actually used

with the ROSE data. A constant, α^2 is added to all diagonal terms to replicate the procedure used with real data. A conventional and MLM estimates for a range of $\underline{v}_t$ is then performed with the final result expressed in decibels: 10 log $P(f, \underline{v}_t)$. The output of each simulation is a random variable. Several trials, usually ten or more, are averaged for statistical stability.

Figures 4-7 through 4-9 show results for a case in which the model plane wave arrives at an angle of 75 to a 24 channel, 2400 meter line array (modelled after the ESP array). This angle corresponds to a horizontal phase velocity of 1550 m/sec, so that results are for a near endfire geometry. The number of frequency components employed was decreased progressively from 29 to 11 to 6 in a one Hz. band centered at 8 Hz. The amplitude P and noise levels σ^2 and α^2 were adjusted so that an unbiased estimate at the target direction is 15 db, based on the process model and eq. 4-29. For both the conventional and MLM curves, the envelope of the mean estimate $\pm$ one sample standard deviation is plotted. In all of these figures, at the plane wave angle, the conventional estimate is considerably less biased than the MLM estimate which decreases steadily as the number of components used becomes smaller. However, at directions away from target, the MLM estimate is sharper and performs on the order of 5 to 10 db better in sidelobe rejection

Since we simulated the space/time process of a unidirectional plane wave in uncorrelated (sensor) noise, the theoretical value of the estimate at $\underline{v}_t = \underline{v}_p$, is (from eq 4-31):

$$\hat{P}_t(f, \underline{v}_p) = P + \frac{\sigma^2 + \alpha^2}{K} \qquad (4\text{-}48)$$

where K is the number of sensors. Diagonal terms of an estimated covariance

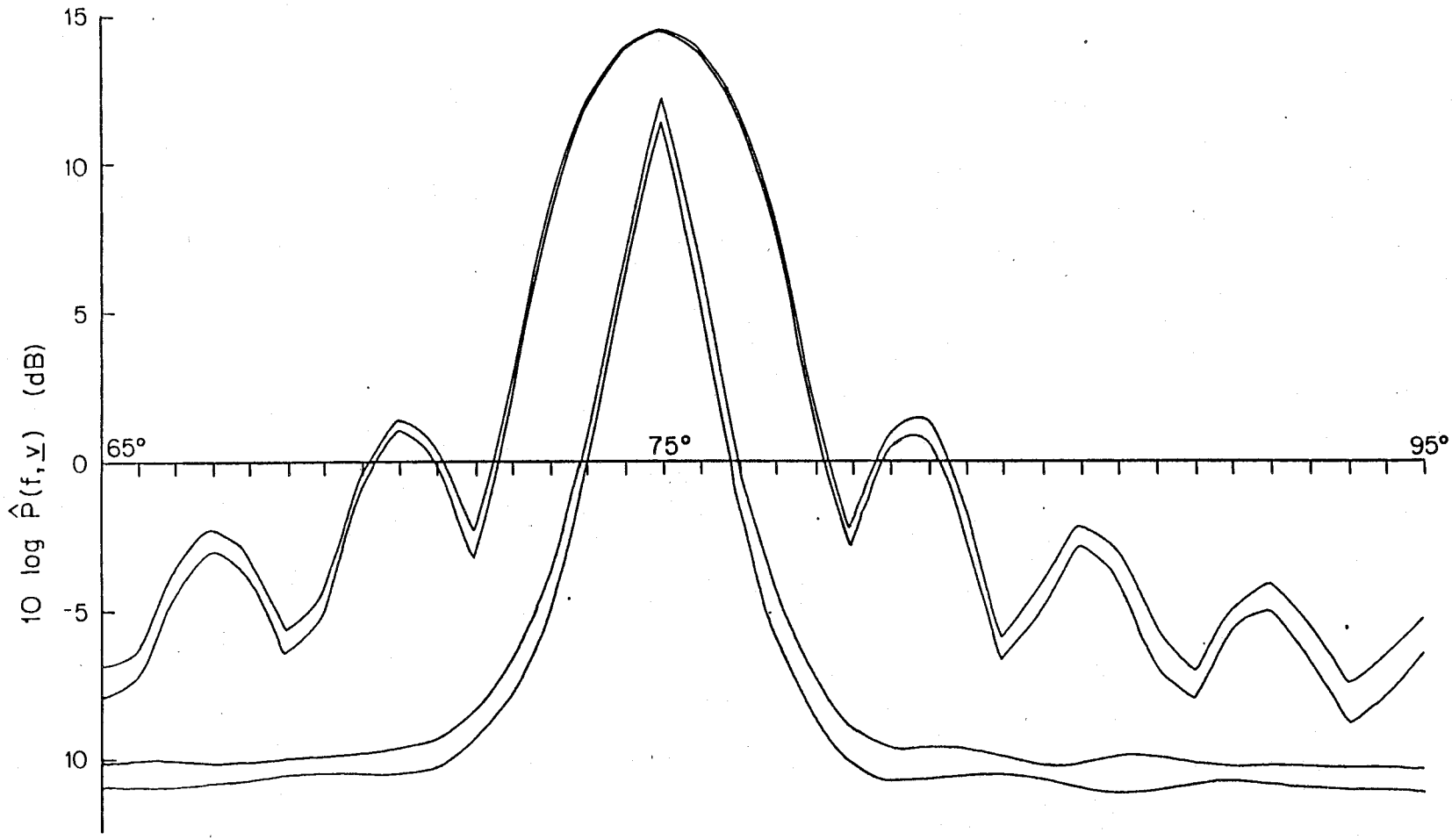

Fig.4-7
Results of simulation program for plane wave arriving at 2400 meter array at 15 off endfire (75). Upper band is conventional and lower band is MLM estimate of P. Unbiased estimates would be 15 db. Number of frequency components averaged in this example is 29.

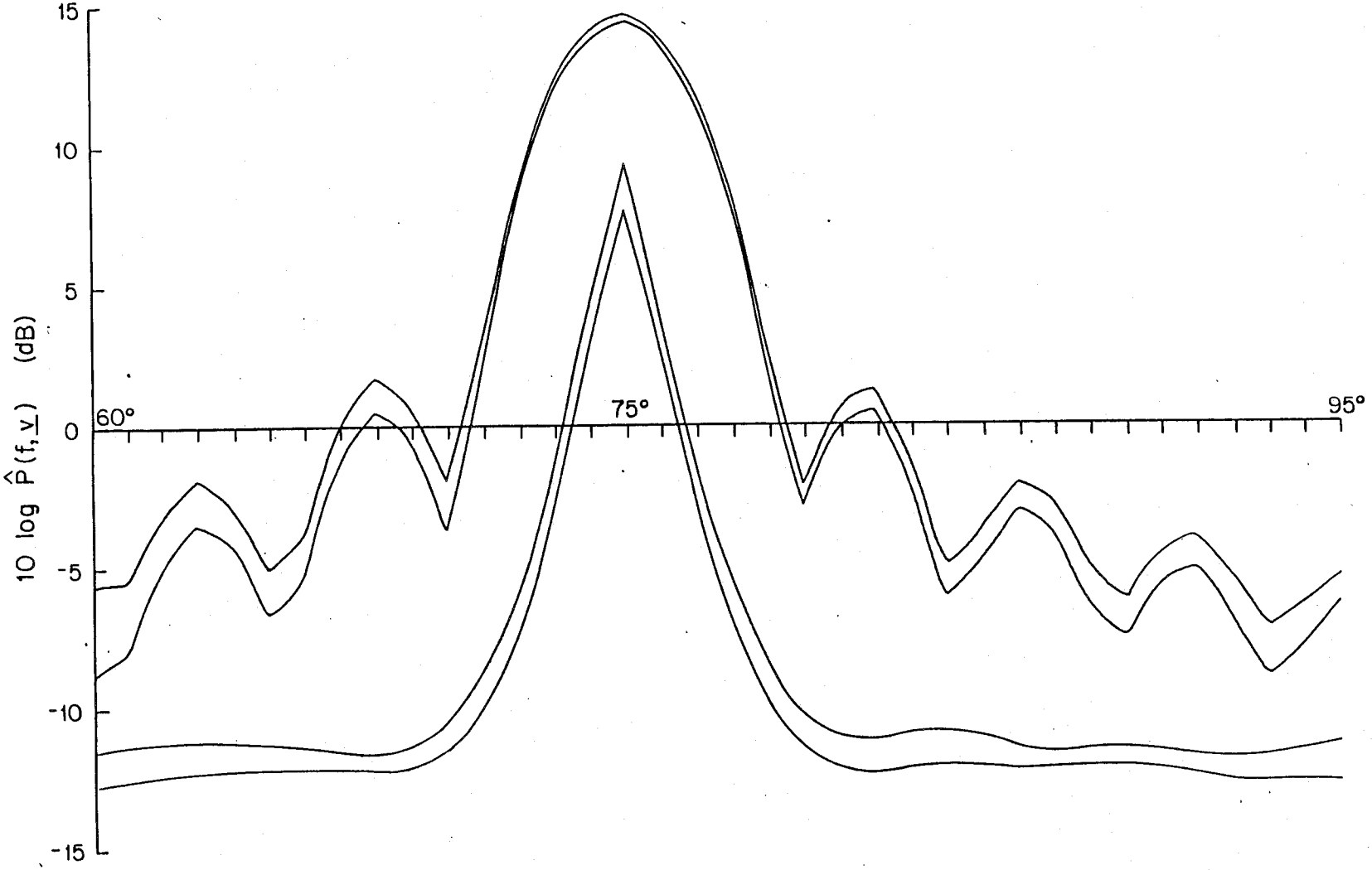

Fig.4-8
Same as fig.4-7 except number of frequency components averaged is 11.

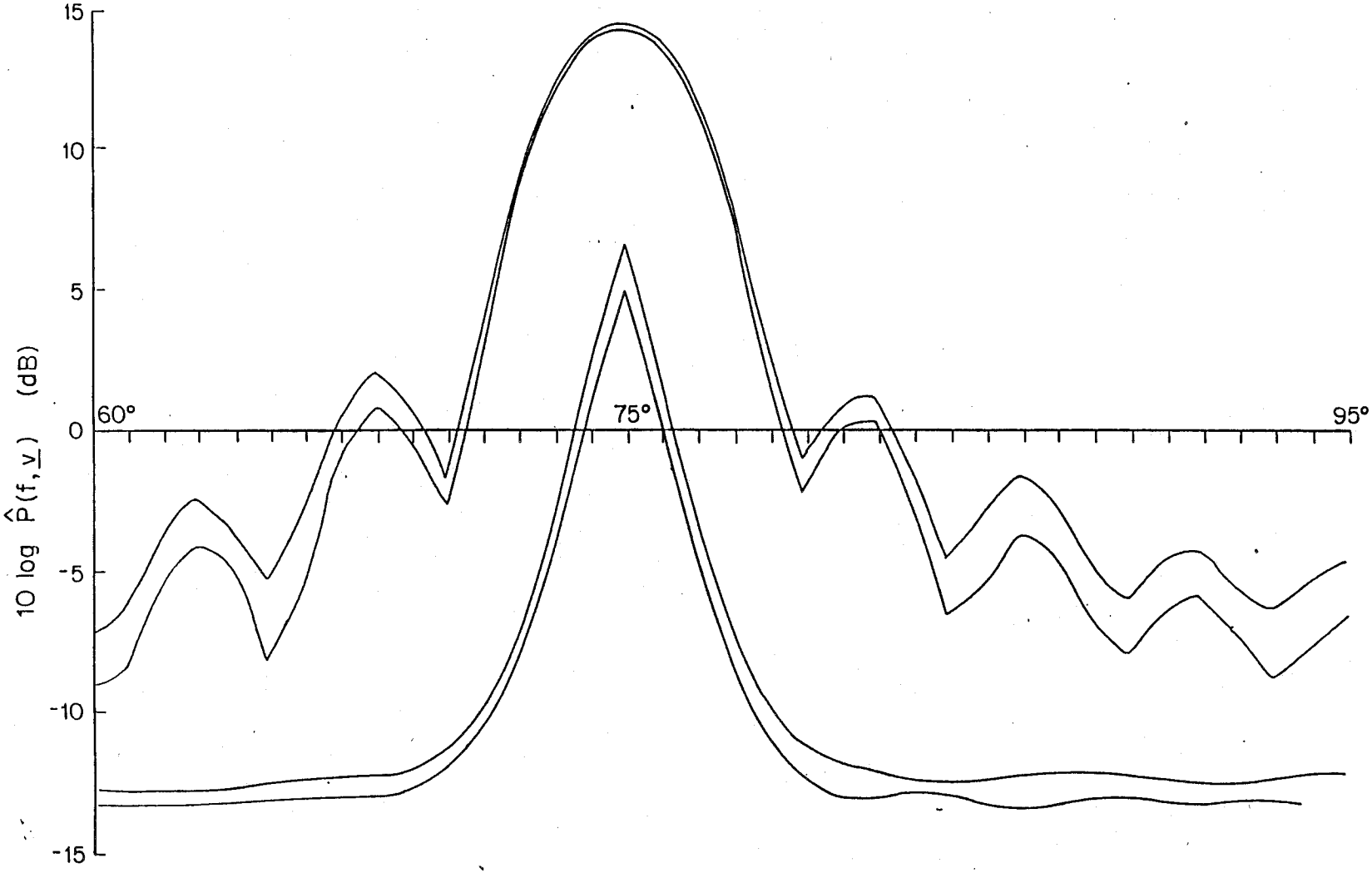

Fig.4-9
Same as fig.4-7 except number of frequency components averaged is 6.

matrix are the only locations in the matrix where the variance of the zero mean noise component appears. The deterministic α^2 term, added to the diagonal alone, is therefore included with the actual variance, σ^2, in eq. 4-48. This expression proved to be experimentally correct since conventional, unbiased estimates generated with the simulation routine were generally centered at $P_x(f, \underline{v})$. The actual mean MLM estimates were always less than this value. Reasoning that bias effects were associated with random variables in the algorithm, we model the actual estimate as:

$$\hat{P}_a(f, \underline{v}_p) = \beta\left[P + \sigma^2/K\right] + \alpha^2/K \qquad (4\text{-}49)$$

where $\beta[P, \alpha^2, \sigma^2, M, K]$ represents an unknown bias coefficient that does not effect the deterministic white noise term. We then define:

$$A[P, \alpha^2, \sigma^2, M, K] = 10 \log \frac{P_x(f, \underline{v}_p)}{P_a(f, \underline{v}_p)} \qquad (4\text{-}50a)$$

$$= 10 \log \left[\frac{1 + \frac{\alpha^2/\sigma^2}{1+SNR}}{\beta + \frac{\alpha^2/\sigma^2}{1+SNR}} \right] \qquad (4\text{-}50b)$$

where $SNR = \frac{KP}{\sigma^2}$. The quantity A represents the deviation in db of the actual results from the theoretical, unbiased estimate. Each time the program was run, a value for A was formed. We estimate a $\hat{\beta}$ from each A by using:

$$\hat{\beta} = 10^{-A/10} + \frac{\alpha^2/\sigma^2}{1+SNR}\left[10^{-A/10} - 1\right] \qquad (4\text{-}51)$$

which is a rearranged version of 4-50b. Figures 4-10 through 4-12 show a summary of the results of this procedure for a model line array 2400 meters long with 8, 12, and 24 channels respectively and for $\underline{v}_x$ about 30° off broadside, corresponding to a horizontal phase velocity of 3000 m/sec. The computed quantity: 10 log $\hat{\beta}$ is plotted versus σ^2/α^2. Each plot contains

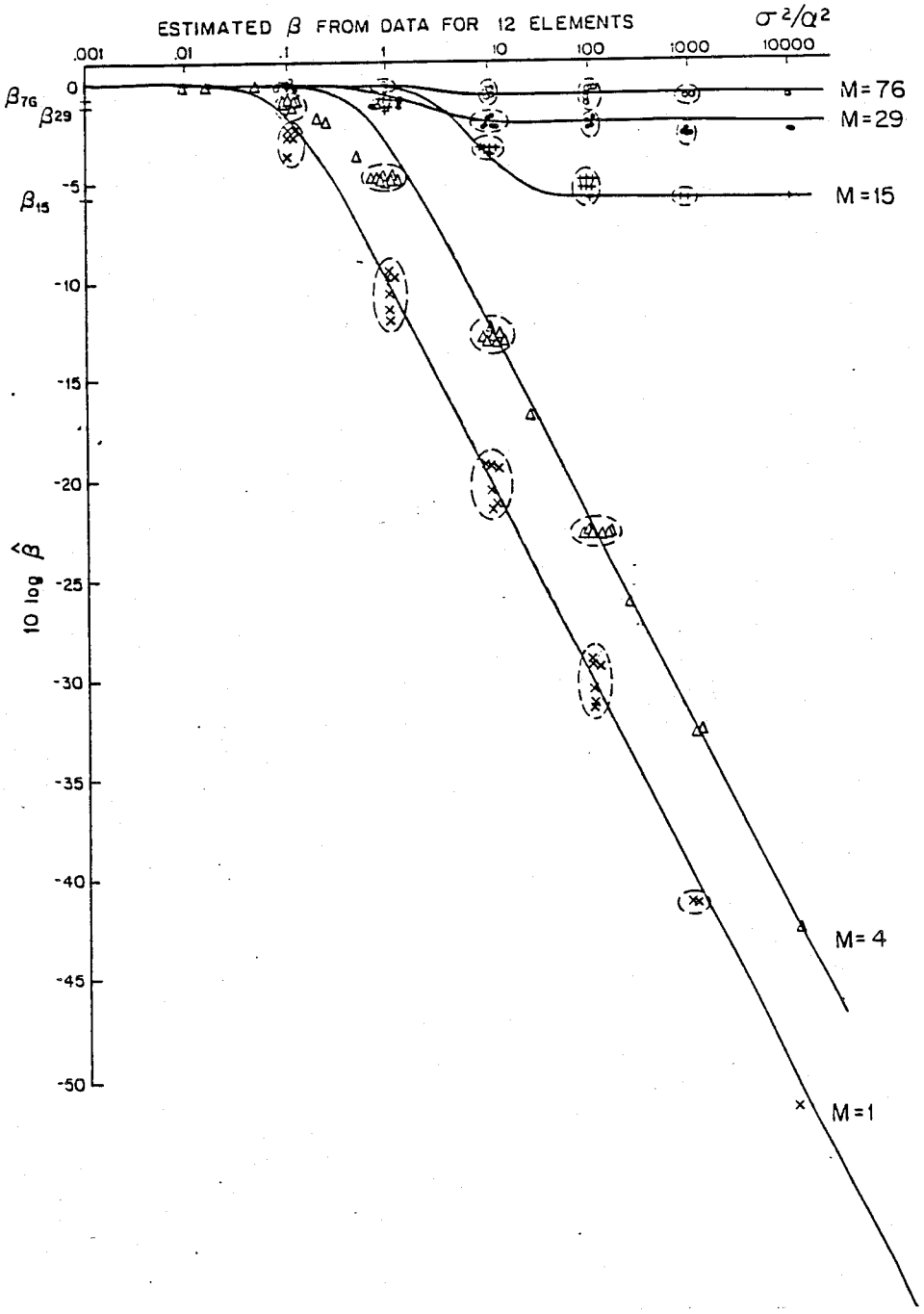

Fig.4-10

Points indicate the estimated value of 10 log , the MLM bias coefficient for different values of / , the ratio of "real" to artificial noise. M is the number of frequency components averaged and, in this figure, the number of sensor elements, K, is 12. The groups of points circled are obtained from one value of / with different levels of SNR. is the theoretical value of the bias coefficient from Capon's formula at M = 76.

Lines drawn through points are obtained from equations in text.

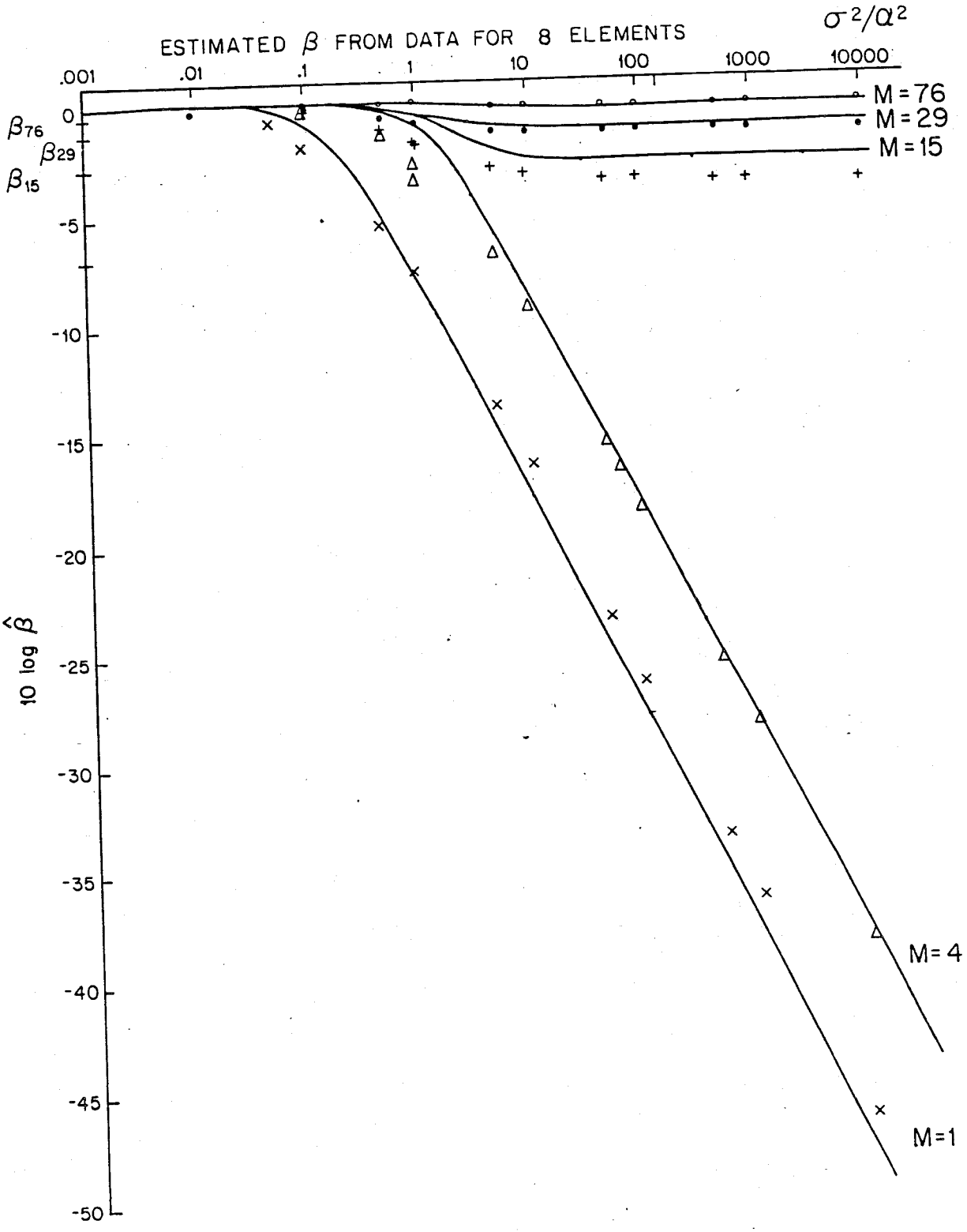

Fig.4-11
Same as fig. 4-10 except number of sensors, K, is 8.

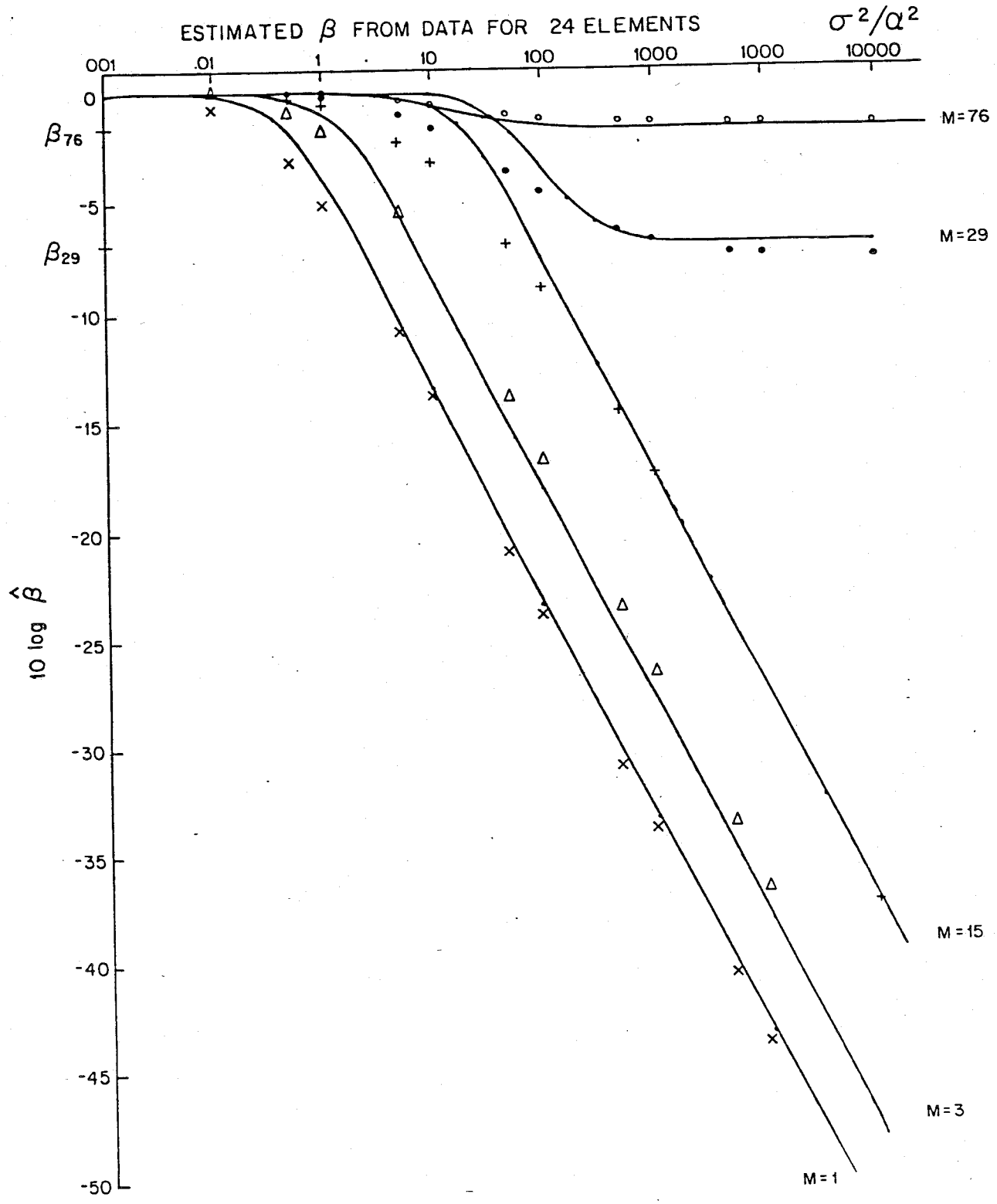

Fig.4-12
Same as fig. 4-10 but number of sensors, K, is 24.

results for a number of frequency coefficients, M. The bias term in Capon's formula loses validity, and the covariance matrix becomes singular, when M-K+1 < 0, or when M < 23 for 24, M < 11 for 12, and M < 7 for 8, sensors. We find in the empirical results that, for M above these cutoffs, the bias estimate approaches a constant value for large σ^2/α^2 and that $\tilde{\beta} \approx \frac{M-K+1}{M} \triangleq \beta_M$ at these values. Capon's formula is approximately the asymptotic result as α^2/σ^2 decreases. Below the cutoffs, however, the bias increases steadily for large σ^2/α^2. The model program was run for a variety of different ratios of SNRs. For the twelve channel case in fig. 4-10, the closely spaced groups of points shown correspond to estimates at one value of σ^2/α^2, but with different SNRs. In all cases, the calculated bias was found to be largely a function of σ^2/α^2, with relatively small sensitivity to SNR. The curves drawn through the points in figures 4-10 to 4-12 were calculated from the following expressions:

$$10 \log \hat{\beta} = 5 \log \left[\frac{1+\varepsilon^4 x^2}{1+\varepsilon^2 x^2} \right] \qquad \text{for } M > (K-1) \qquad (4\text{-}52)$$

$$10 \log \hat{\beta} = -5 \log \left[1+\varepsilon^2 x^2 \right] \qquad \text{for } M \leq (K-1) \qquad (4\text{-}53)$$

where $x = \sigma^2/\alpha^2$ and $\varepsilon = \frac{M-K+1}{M}$. These expressions were determined after noticing the resemblance of figs. 4-10 to 4-12 to frequency response curves of linear filters. They fit the bias data quite well and were valuable for simplifying the bias correction process.

Bias Corrections

We now describe the procedure followed in determining bias corrections

necessary for ROSE data estimates.

1) In order to fit the actual data to the basic model used in the simulation routine, we are assuming that, in correcting an estimated level for a significant event, the background noise behaves as temporally white, spatially uncorrelated sensor noise. In order to apply the empirical results, an unknown of importance when working with real data is the value of σ^2, the power in this uncorrelated noise component in the data. We evaluate the output of the MLM program in directions where no obvious coherent signal is present and find an average background level: 10 log $\hat{P}_{AMB}$. In this direction, the original $\hat{S}(i,j)$ matrix, as implemented in the MLM program, has estimates of σ^2 on the diagonal, and, after normalization, the γ term added to the unity diagonal of $\hat{S}_{norm}(i,j)$ is a <u>percentage</u> of σ^2, so that:

$$\alpha^2 = \gamma \sigma^2 \qquad (4\text{-}54)$$

Again, this expression for α^2 is valid only in directions away from any significant propagating noise.

2) Letting $\sigma^2/\alpha^2 = \gamma$ in this case, $\hat{\beta}$ for this ratio can be evaluated either from figs.4-10 to 4-12 or from the expressions in eqs 4-52, 4-53. This $\hat{\beta}$ is a function of the number of sensors and frequency coefficients used in the estimation at the particular event being corrected.

3) For this "ambient" noise case, P = 0, and eq. 4-49 becomes:

$$\hat{P}_{AMB} = \hat{\beta}\left[\frac{\sigma^2}{K}\right] + \frac{\alpha^2}{K} \qquad (4\text{-}55)$$

Using eq 4-55, we determine σ^2 :

$$\sigma^2 = \frac{K \hat{P}_{AMB}}{\beta + \gamma} \qquad (4\text{-}56)$$

4) After finding σ^2, we are in a position to calculate biases in cases where $P \neq 0$. In the actual implementation, the diagonal terms of $\hat{S}_{NORM}(i,j)$ become estimates of $P + \sigma^2$ in the model, so that the α^2 terms in the model are related to γ by:

$$\alpha^2 = \gamma (P + \sigma^2) \tag{4-57}$$

5) Graphs of $\hat{P}$ vs. P were desired for particular values of σ^2, α^2, K, and M that were relevant to the ROSE data. For each desired P, with γ and σ^2 being known, the values of α^2 and σ^2/α^2 is determined from 4-57. A new $\hat{\beta}$ is then evaluated from the graphs or the formulas.

6) Using eq 4-50, the biased P for each P is found:

$$\hat{P} = \hat{\beta}\left[P + \sigma^2/K\right] + \alpha^2/K \tag{4-58}$$

Examples of final graphs of 10 log P vs. 10 log P are shown in figures 4-13 and 4-14. Note that for large values of P, estimates were fairly unbiased. This is the case since, for large diagonal terms, the effective constant, α^2, added to the diagonals is relatively large. The ratio σ^2/α^2, then, is smaller and the bias coefficient, $\hat{\beta}$, is near unity. For lower levels, the bias can become quite large. A rough average bias in the ROSE data for major events with energies significantly higher than the background level, was found to be on the order of 5 to 10 db.

We have described the fundamental ideas behind the MLM algorithm. To illustrate its behavior with refraction data, results obtained in the estimation of arrival phase velocities from ROSE data are presented in the next chapter. We then discuss estimation of energy partitioning in Chapter VI.

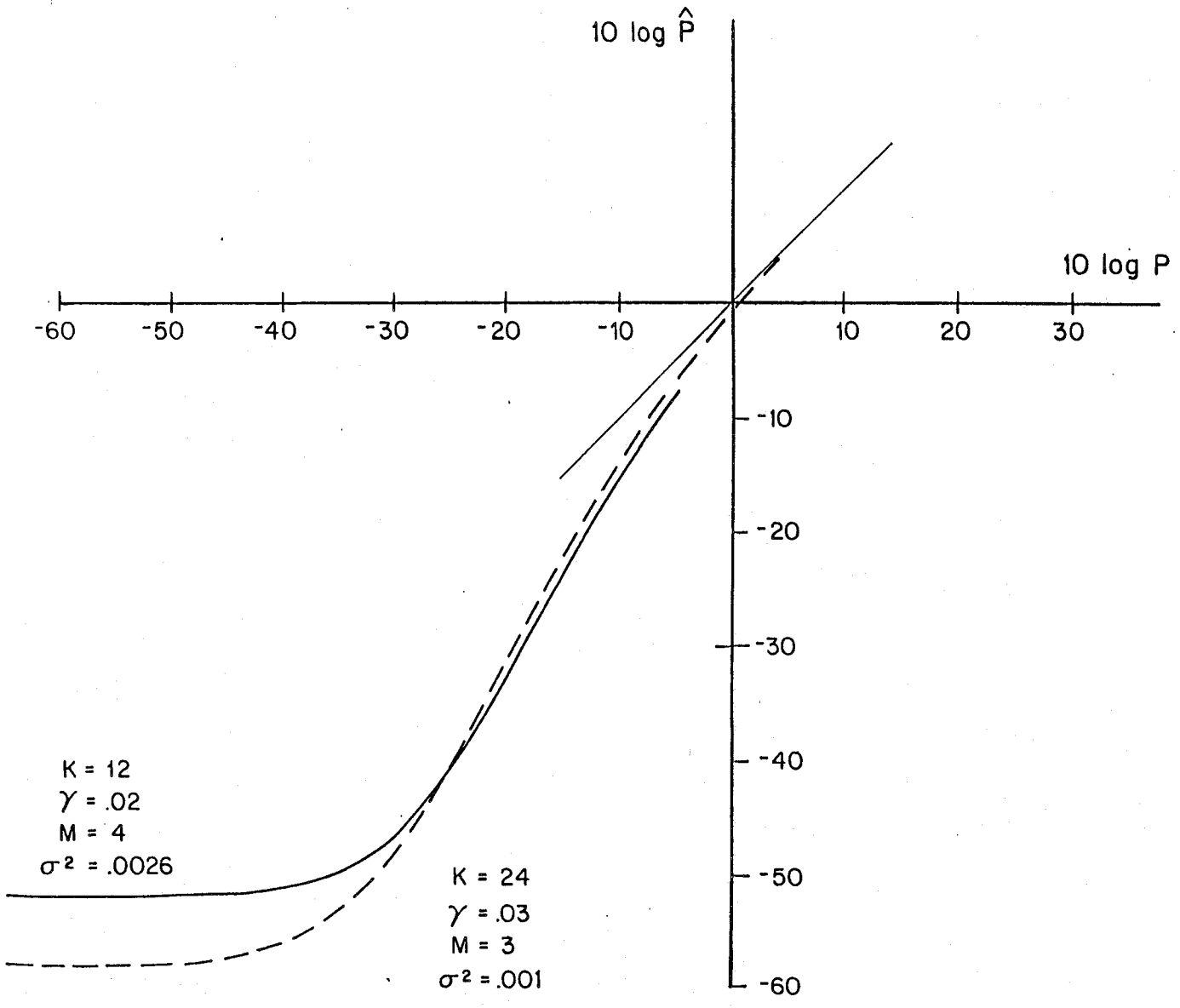

Fig.4-13
Example of P versus P curve (actual versus estimated value of coherent energy for different values of K, σ^2, M, and γ.

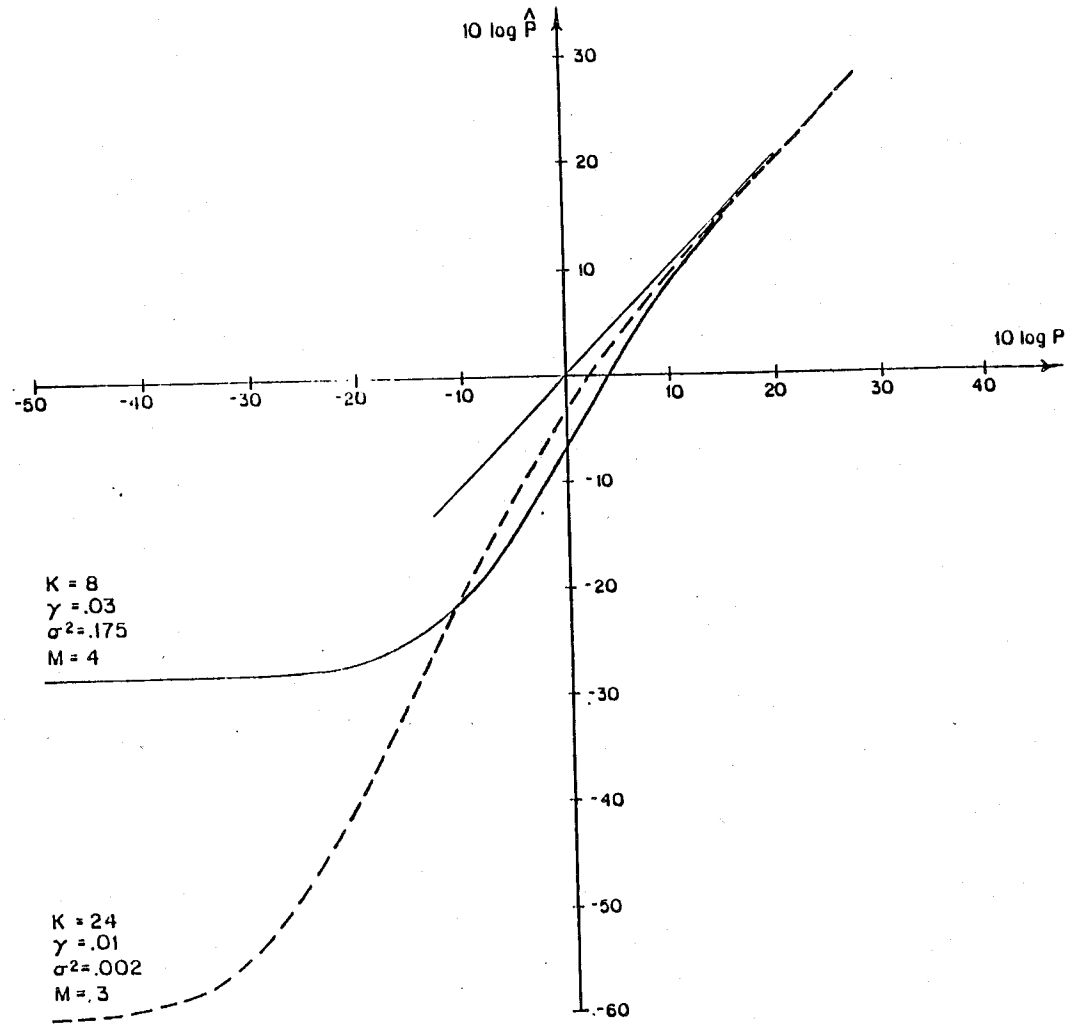

Fig.4-14
Same as fig.4-13.

CHAPTER V

VELOCITY ESTIMATION FROM ROSE DATA

Before discussing crustal transmission loss estimates calculated from ROSE data, we first examine the use of the MLM algorithm as an estimator of crustal velocities. This will serve as an illustration of the behavior of the estimator with actual refraction data. The algorithm resolves received energy with respect to temporal frequency bands and horizontal phase velocities (or angles of arrival) at an array. If the relationship between the horizontal phase velocity of coherent energy at the sensors and the velocity structure of the crust is known, than the algorithm effectively produces crustal velocity estimates as well. For a horizontally layered crustal model, the relationship is quite simple. The layer sound speed will be numerically equal to the horizontal phase velocity at the array, which is:

$$C_p = \frac{c_o}{\sin\theta} = 1/p \qquad (5\text{-}1)$$

where θ is the vertical angle of arrival, c_o is the water sound speed, and p is the ray parameter or "slowness" of the arrival. In chapter II we showed that a more realistic view of the crust is based on a model with continuous velocity gradients with respect to depth. The horizontal phase velocity of coherent events in this case is equal to the sound speed in the medium at which a ray turns upward.

Lines 2S and 2L of the ROSE experiment took place over thinly sedimented areas with a crustal age of approximately 5 M.Y (Ewing & Purdy, 1982). Based on a compilation of data from 529 ocean basin refraction

experiments, Christensen and Salisbury (1975) show that, in relatively young regions such as this, anomalously low mantle refraction velocities (7.1 to 7.8 km/sec) are frequently observed and also that, at offsets less than 35 km, "layer 3" velocities in the range of 6.7 to 6.9 km/sec predominate. First arrivals with estimated velocities in these bands are the most prevalent in the MLM analyses. A consistent set of second arrivals, with lower phase velocity estimates, which may be converted shear or, more probably, "layer 2" events are also seen in line 2S.

In analysing ROSE velocity estimates, two considerations must be kept in mind. Bathymetry is very complex near spreading centers and velocities estimated from array data are influenced by topography to the extent that, without appropriate corrections, errors on the order of 1 km/sec may occur. Bathymetric data with sufficient resolution for correcting this problem is not available for the ROSE experiment because of navigation failure. Secondly, ESP lines 2S and 2L crossed at least two fracture zones (see fig. 5-1 from Purdy (1982)). Results obtained by Purdy (1982) from OBS data near these fracture zones are compatible with an increased thickness of low velocity material in the uppermost crust, a feature of fracture zone troughs (Ludwig & Rabinowitz, (1980); Detrick and Purdy,(1980). This non-homogeneity in the structure must be taken into account in viewing the MLM results from the standpoint of "normal" crustal models.

In this chapter, following illustrations of some time profiles of horizontal and vertical array data, contoured plots of the relative strength of arrivals with respect to phase velocity and travel time are presented. A summary plot of all experiments in one shooting line is then discussed with

special attention given to arrivals beyond the first. Despite the effects of rough topography mentioned above, we show that the ability of the array to discriminate arrivals with different relative phase velocity can still be applied. A travel time-offset plot with events labelled with respect to their approximate phase velocity range is presented for both ESP lines.

Time Profiles

We first look at some of the raw data as it was entered into the velocity analysis program. In figures 5-2a and 2b, 12 of the 24 channels of data, arranged sequentially, from the horizontal array (ESP) are plotted versus travel time (vertical axis). Horizontal offset for this data was 26 km. and each tick mark represents one second. The first arrival, at about two seconds into the record, appears almost simultaneously on all the sensors, i.e. with little "moveout". Since it appears coherently across the array, this high phase velocity event is a "refracted" arrival (1P) emitted from the seabed, meeting the array almost broadside (i.e. at a vertical angle close to zero, or a "grazing" angle near 90°). The next visually apparent arrival occurs about 4.5 seconds later and displays the same small moveout across the elements. This is a "refracted/ reflected" arrival (2P), as defined in Chapter II. The water depth in this area is about 3 km so that the round trip time from the seabed to the water surface and back is on the order of 4 seconds. Turning to figure 5-2b, two stronger arrivals occur at T=17 and T=19 on channel 1, the sensor closest to the receiving ship and furthest from the shot. Unlike the previous two, these are displaced in time across the array,

Fig. 5-2b
see caption for fig.5-2a.

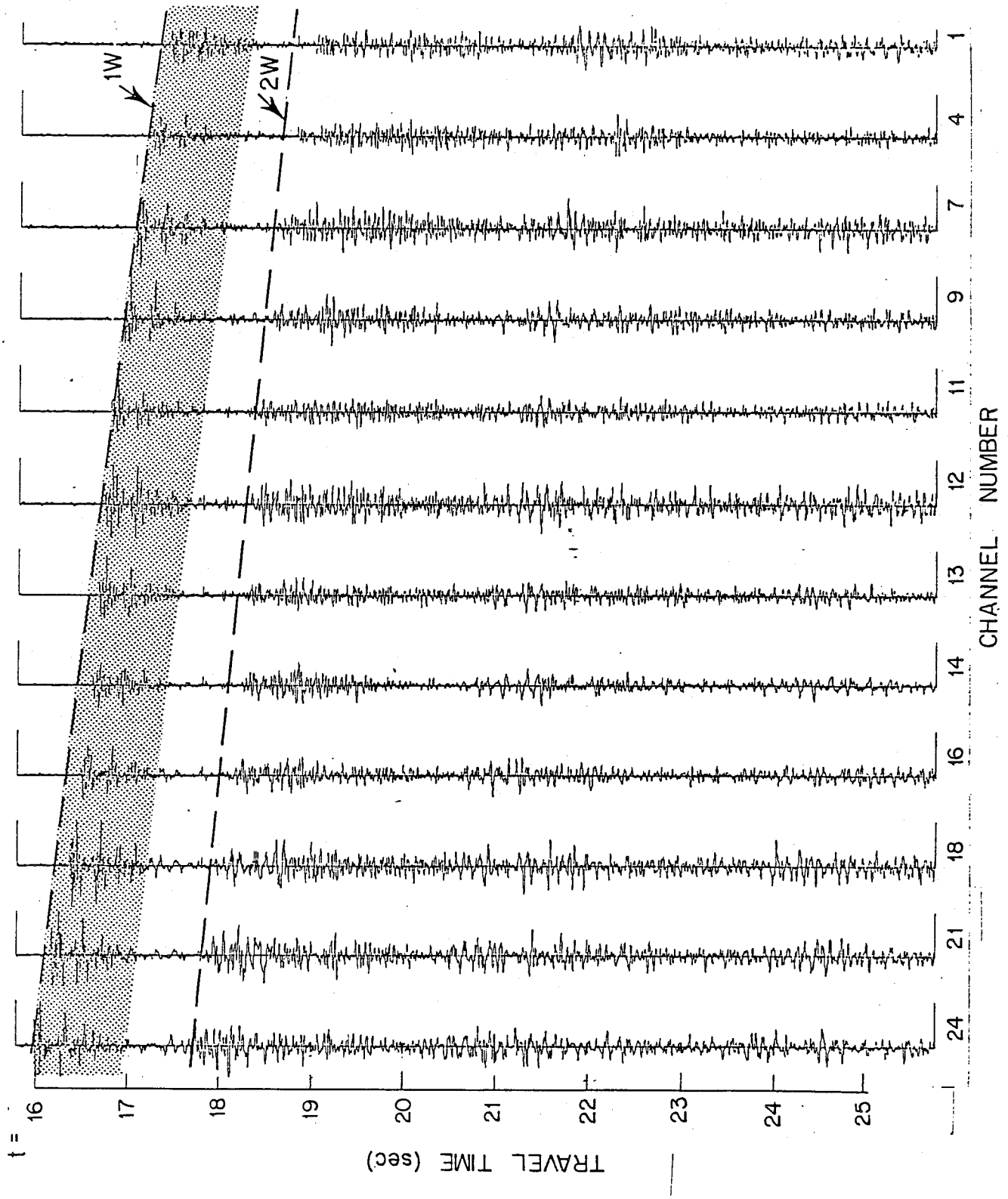

Fig. 5-2b
see caption for fig.5-2a.

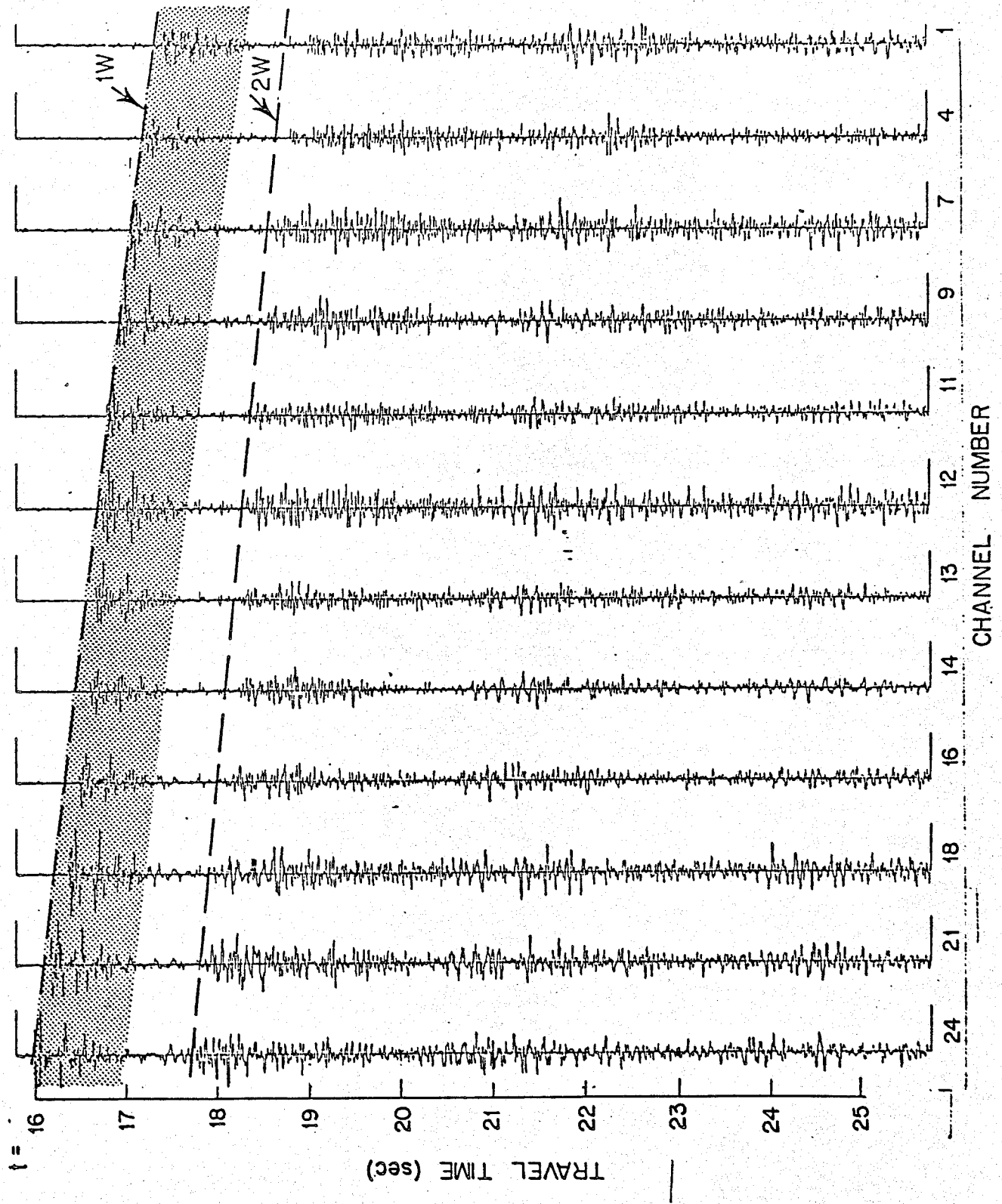

i.e. with larger moveout. They arrive at a smaller grazing angle, i.e. more from the shot direction than the seafloor. These are water arrivals: 1W and 2W, with low horizontal phase velocities.

Figure 5-3 shows data from the 12 channel vertical array (MABS) at a range of 17 km. As we have discussed, channels 5, 7, 11, and 12 were malfunctioning. Unlike the ESP case above, the first arrivals here, at T=6.3 sec on the shallowest channel, #1, have the greatest moveout. This is expected for energy coming from the sea floor direction and arriving almost endfire. Another set of arrivals appears at T= 7.8 seconds on channel 1. This event also has a large moveout, but it propagates in the opposite direction. The shallowest channel in the deployment was at a depth of about 1 kilometer. If we were to "continue" the locus of first points at each sensor for both of these events up to a hypothetical sensor at the surface, as indicated by the dashed lines in the figure, the lines intersect. Both arrivals result from the same crustal "refraction" (1P) with the later one being caused by reflection at the surface. At about 9 seconds into the data on channel 1, another endfire set of arrivals can be seen across the sensors. Occurring at a 4.5 second interval after 1P, this is again a refracted/reflected 2P. Finally, a set of arrivals that appear almost horizontally across the data is seen at T =11.2 seconds. Because of their large amplitudes, the tape recorders saturated at this point, and there is no usable information beyond. Since there is no moveout for this set, however, it is clearly a direct water arrival.

Fig. 5-3
Time profile of vertical (MABS) array data.

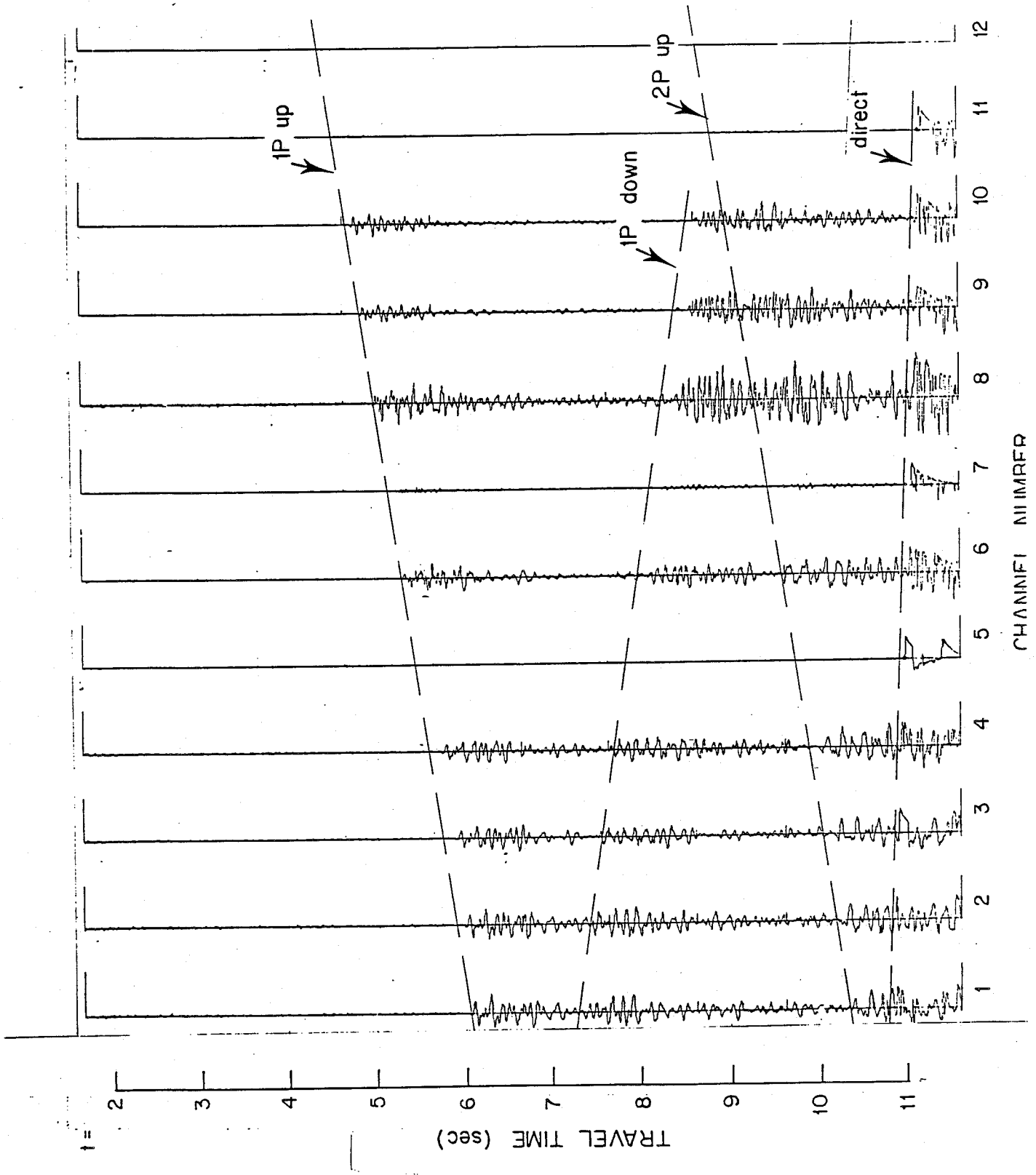

RESULTS OF VELOCITY ANALYSIS PROGRAM

We now present some results of the MLM procedure applied on the data just discussed. Figure 5-4 is a contoured plot of the estimated wavenumber function, in a three Hertz band centered at 8 Hz, versus phase velocity (vertically) and travel time (horizontal). These estimates were calculated from the horizontal array data shown in figs. 5-2. At each time T, the target angle, looking downward, was stepped over a range of 0° to about 80° (grazing) in increments which correspond to equal slowness (p) intervals of about 5.8 μs/meter. The range of phase velocities is 1.5 to 8.8 km/sec. The contouring of the levels was done at 2 db. intervals. Proceeding from left to right, a background level of -50 db. quickly changes to a sharp peak about two seconds into the figure. This peak, at a phase velocity of 6.8 km/sec corresponds to the first arrival (1P) observed on the profile in fig. 5-2. The maximum level here is at about -15.5 db. The value of the level estimates has not been corrected for the effects of MLM bias. A second event (" 1P' "), not visually apparent in fig. 5-2, occurs a fraction of a second later at a slightly lower c_p. This "doublet" phenomenon is seen frequently in the ROSE data. One possible explanation is the existence of a low velocity zone at the base of the crust (Lewis and Snydsman, 1977). Evidence of a low velocity region in lower crust, from an OBS experiment conducted near the East Pacific Rise, is also presented by Orcutt (1976).

The next prominent arrival, at T =11.2 seconds, was also not discernable on the time profile. With a phase velocity of about 4.5 km/sec, and a level about 13 db lower than 1P and 1P', it is either a late arrival

Fig.5-4a

Results of velocity analysis of data in figs. 5-2. Horizontal axis is travel time. Vertical axes are: 1)apparent phase velocity across array, 2)equivalent slowness (p) of arrival, and 3) equivalent grazing angle at array for plane waves. Amplitude of estimates are contoured in 4 db increments.

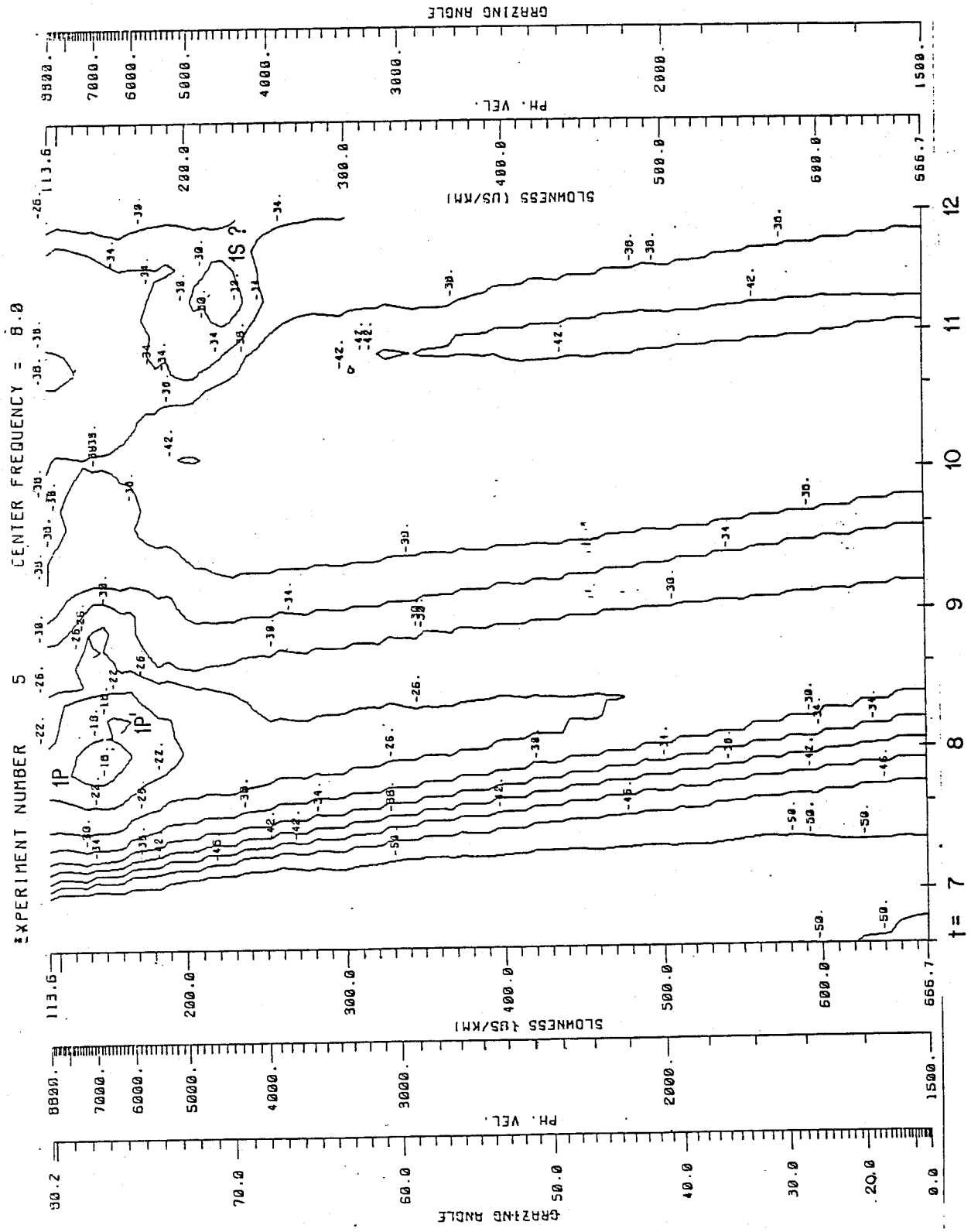

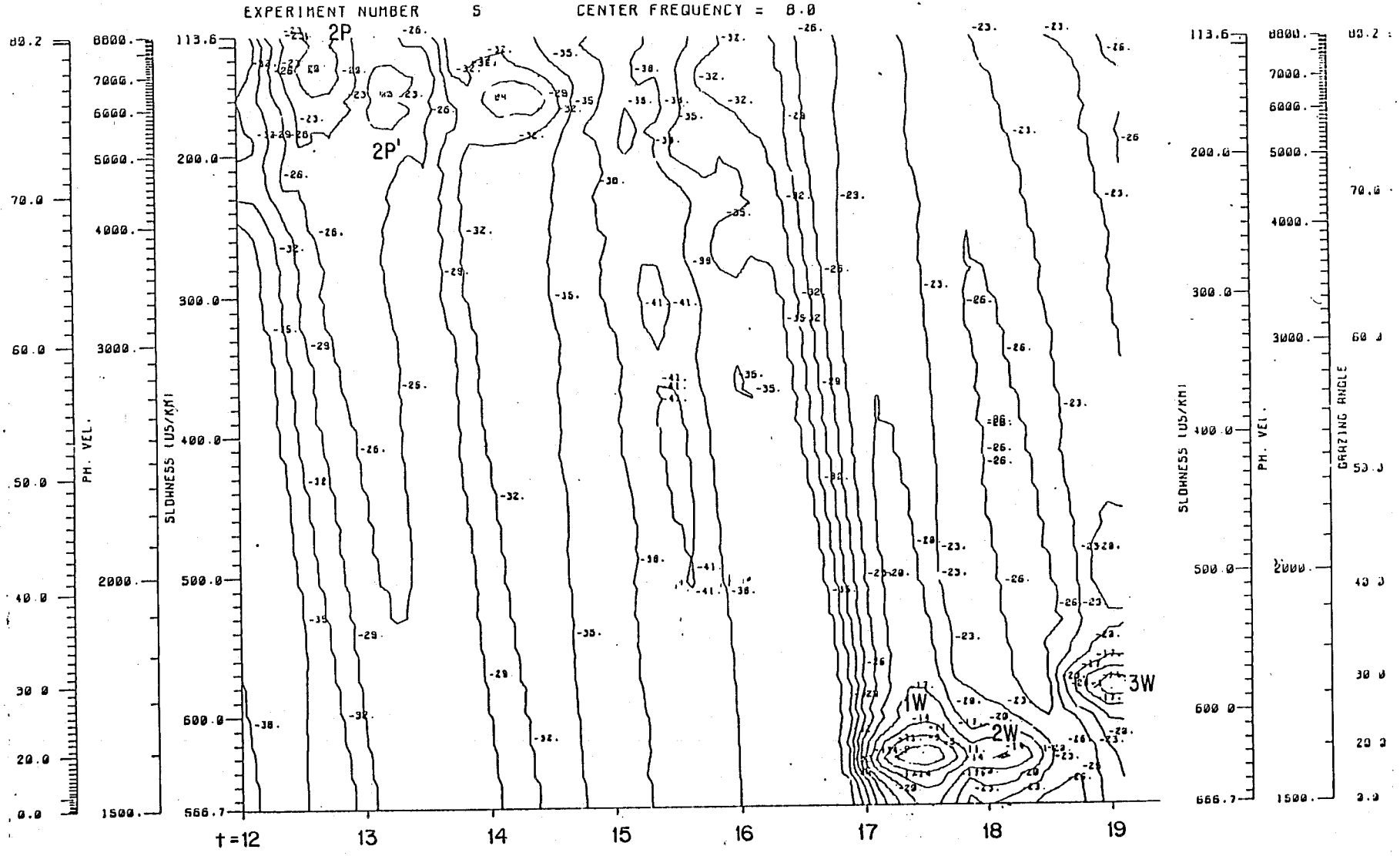

Fig.5-4b
See caption for fig.5-4a.

from an area with a lower sound speed ("layer 2", if we use the Raitt model), or a converted shear wave (1S), although the phase speed is somewhat high for the latter case. The next peak, 4.5 seconds after 1P, is the refracted/reflected 2P with a level of about -18 db and a velocity of 7.3 km/sec. The level of this arrival here is not higher than that of 1P, although this is often the case. An echo of 1P' appears next at T=12.7 followed a second later by a weaker (-27 db) event at 6.2 km/sec. Again, these last two, although considerably stronger than the background level, were nevertheless not visually discernable. Finally, a progression of arrivals begins after T=17 seconds at very shallow grazing angles. The fact that each of these progressively increases in angle is in accord with the interpretation of these as water bounces with higher order reflections encountering the array at larger angles.

Before turning to MLM estimates of the MABS data, we first present results from a Line 2S shot at a 31 km offset in fig. 5-5. The resolution in phase velocity of prominent events is not as great as in the preceeding case. This is due to the fact that only 12 of the 24 data channels were used when processing line 2S. For this experiment, the doublet phenomenon is again seen at T=8.2 and T=9 seconds, as well as the 2P arrival 4.5 seconds later. With the increased offset, a "3P" arrival also occurs at T=17.5 followed by 3 water arrivals at T=20, 21, and 24.5.

In Figs. 5-6a and 5-6b, we look at MLM estimates obtained with the vertical (MABS) data of fig. 5-3. This data was obtained from the same shot as the ESP data just discussed, although the offset to the MABS was only 17 km.

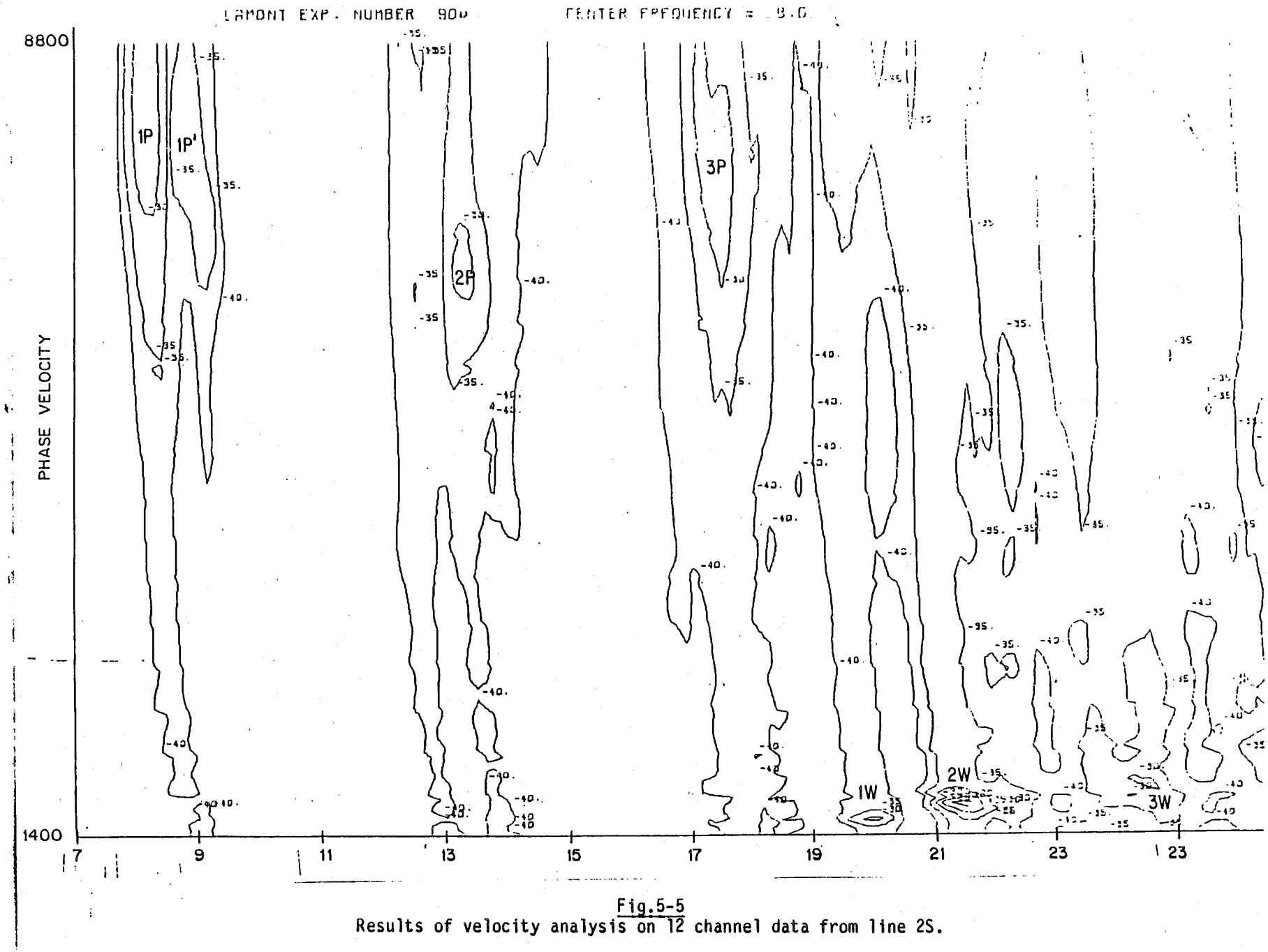

Fig.5-5
Results of velocity analysis on 12 channel data from line 2S.

Again, vertical resolution (in phase velocity) is not as sharp as in the ESP 2L results due to the smaller number (8) of sensors, and the fact that, for high phase velocity arrivals, the energy encounters the array close to endfire The 1P arrival at 6.2 seconds on channel 1 of fig. 5-3 is represented as the peak at T =6.8 sec. on the contour plot. Since the mathematical origin of the array geometry used in the algorithm is at the surface, for a channel at depth z_i and a target angle looking below the vertical array, an estimate at time t uses data that appeared on channel i at:

$$t - \frac{z_i \cos\theta}{c_o} \qquad (5\text{-}2)$$

For channel 1, at 1 km depth, this is .66 sec at a phase velocity of 7000 km/sec. At T=11 seconds, the event at phase velocity 5 km/sec, with amplitude 20.6 db, is the upgoing 2P arrival observed in fig 5-3. In this case, the 2P level is indeed higher than that of the 1P. In fig 5-3, we saw that beginning at T≈11 seconds, the recorded MABS data was not usable for velocity analysis. The 2P event estimated at this time, however, is still based on earlier, coherent data. Using eq 5-2, the approximate locus of invalid data is indicated in the shaded region.

Although the horizontal offset in this data is, respectively, 9 and 14 km less than the offset of the 2L and 2S data discussed above, the higher level (+17.3 db) of 1P in these estimates is partly due to a decreased MLM bias for the smaller number of channels used. In the next chapter, compensations for this effect are calculated so that levels are made insensitive to channel number for the 8, 12, and 24 sensor data.

In figure 5-6b the target angle used in the MLM algorithm was set for

Fig.5-6a

Results of velocity analysis on 8 channel vertical array data, with target angle looking down. Shaded area is approximate locus of invalid data.

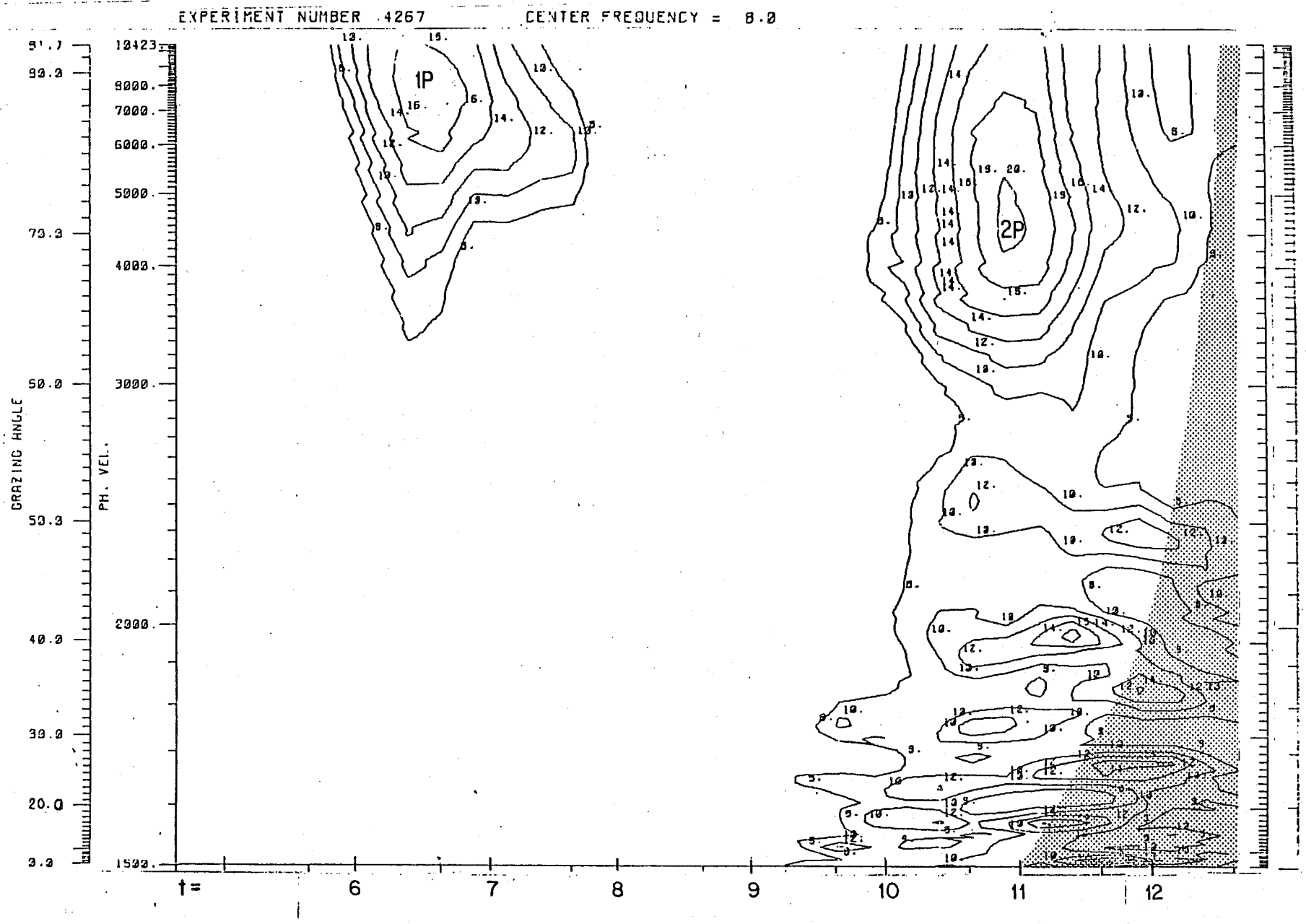

Fig.5-6b
Same as fig. 5-6a except target angle set for looking up.

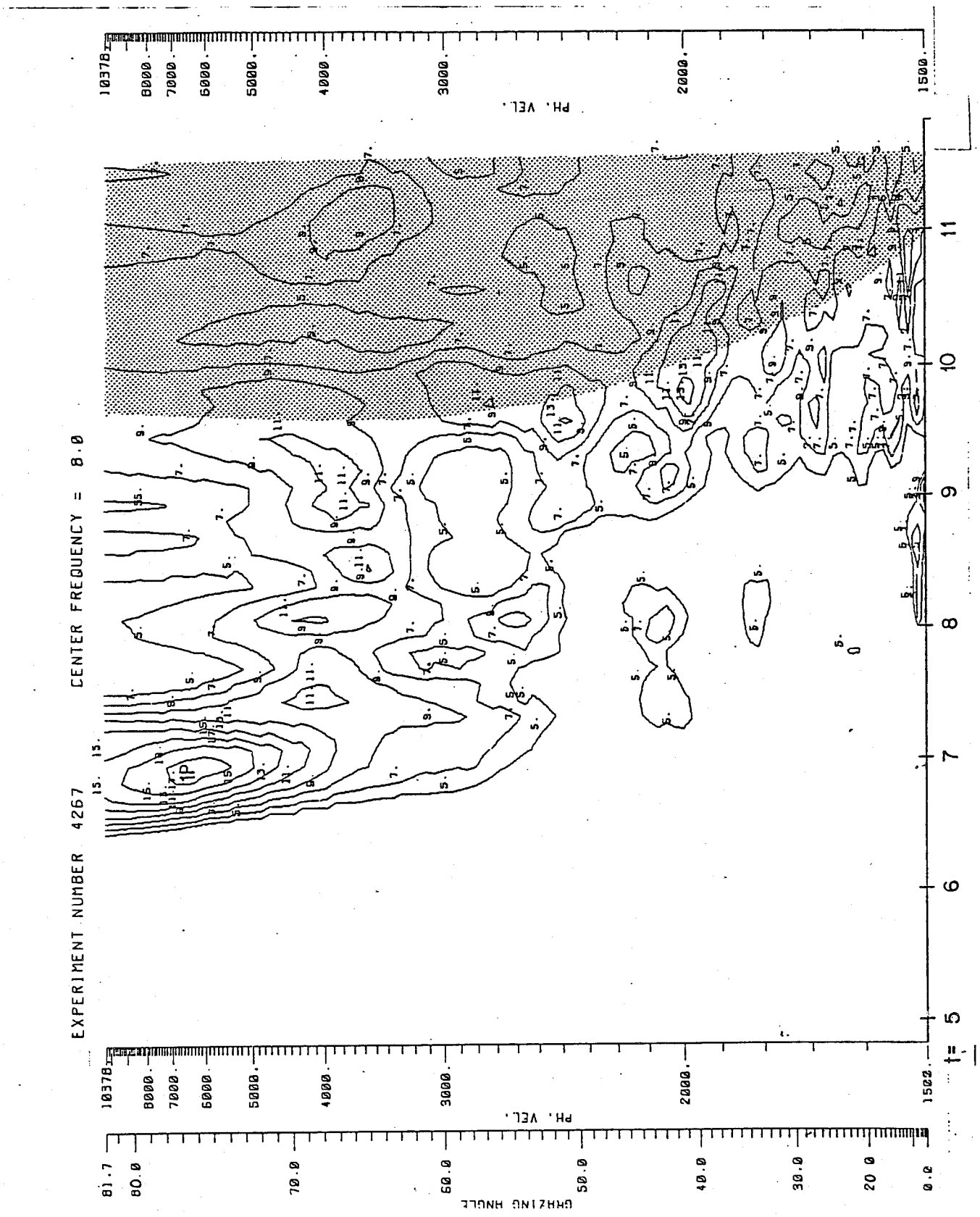

estimation in the same phase velocity range as above, except that the array looks upward. Arrivals from the surface are contoured. The 1P reflected arrival appears earlier in this case since data subsequent to the estimation time is used. The locus of invalid data has increased in this case, as indicated in the shaded region The peak level of 1P here is about 3db higher than that of the corresponding event in 5-6a., due to interference effects at the surface and statistical fluctuations.

For an overall view of the behavior of the velocity estimates generated by the routine at different offsets, figure 5-7a and 5-7b are schematic outlines of the main events from contour plots of ten shots in one ESP refraction line (2S) at the 8 Hertz center frequency. Each of the ten bands gives a summary of one experiment with the prominent events plotted horizontally with travel time after the first arrival, and vertically with estimated phase velocity from zero to ten km/sec. The estimated levels and path designations (where possible) are annotated at each peak. All ten shots appear with first arrivals alligning vertically. The appearance of 1W in each band (indicated by the dashed lines) occurs at the first event with relatively low (1.5 to 2 km/sec) estimated velocity. Preceeding 1W, most of the energy is seen to concentrate at time intervals of 4.5 seconds and at high estimated velocities, due to refraction/reflection. There is a "splitting" of 1P into distinct multipaths in most experiments and this phenomemon is also seen in the 2P regions. "Medium" velocity arrivals (in a 4 to 6 km/sec band) occur two to three seconds after 1P in four of the bands. The level of peaks in the 2P

Fig.5-7a

Schematic outline of results of MLM analysis on line 2S ESP data. Each band indicates results from one shot. The vertical axis is phase velocity in each band and the horizontal axis is travel time. Each band begins with the first significant event for the shot.

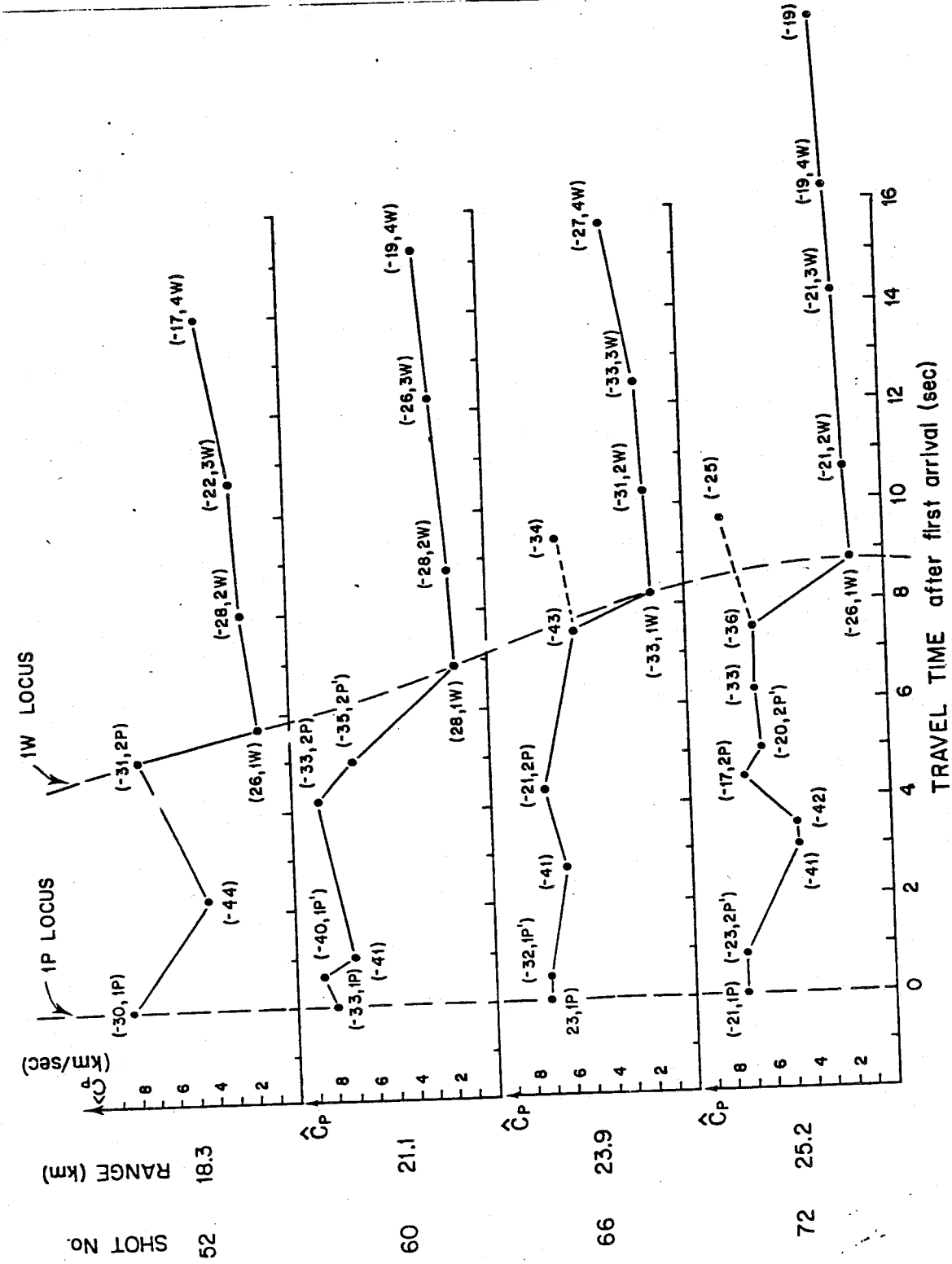

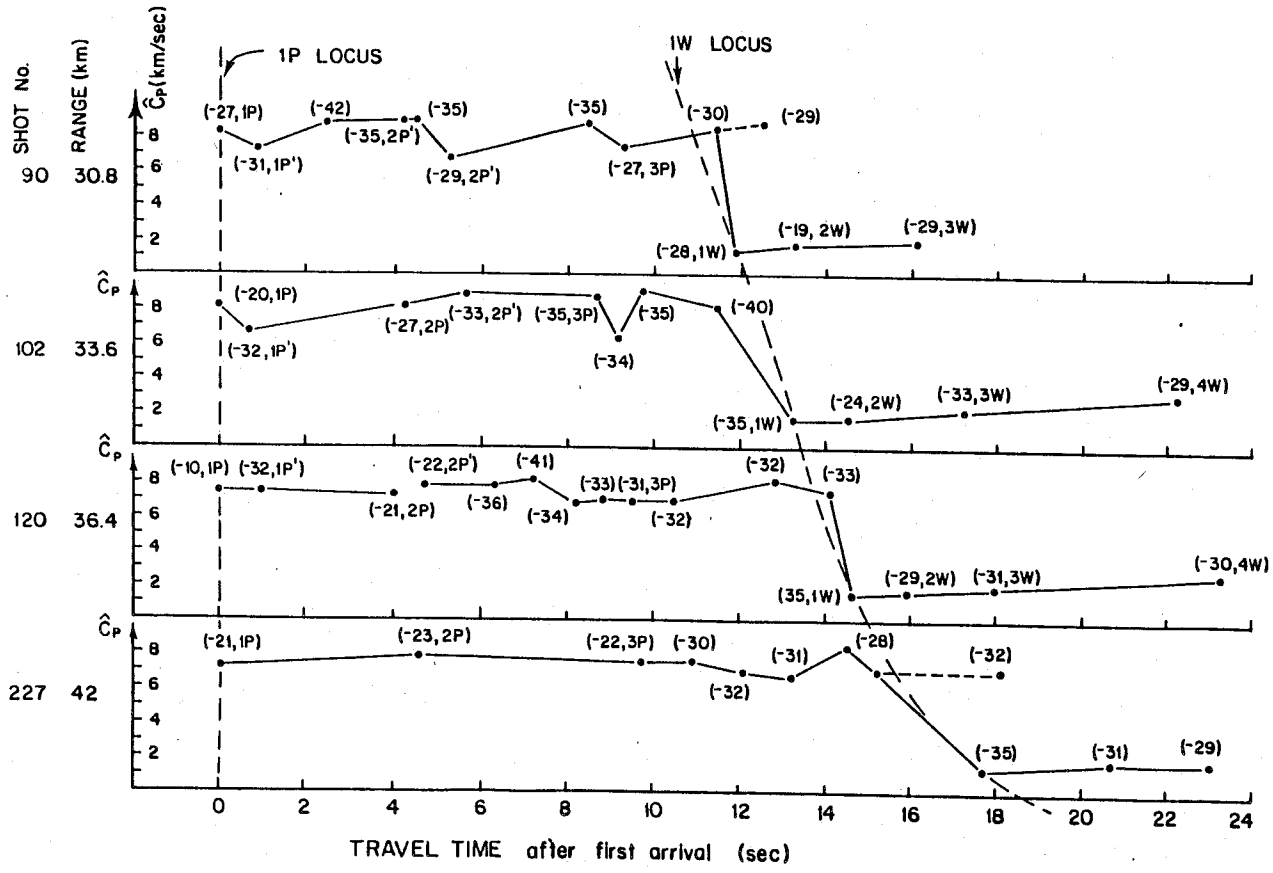

Fig.5-7b
See caption for fig.5-7a.

regions is not consistently higher or lower than the 1P levels. This could be due to interference, varying from constructive to destructive, due to bathymetric variations which were on the order of a wavelength (200 meters). After the water wave arrivals, most shots exhibit the multiple structure we have discussed, gradually increasing in "velocity" and separation from the preceding multiple.

Within each shot band, the estimates give a good indication of the relative variation in phase velocity of coherent arrivals. This has made it possible to identify different types of arrivals in one experiment. Actual numerical velocity estimates from an array, however, are suspect in regions where the horizontal layer model is not valid due to rough topography. For instance, if we take the simple one inteface model and allow the boundary to be slightly inclined from the horizontal by $\Delta\phi$, the variation of estimated phase velocity in the water with the inclination, via eq. 5-1, is:

$$\Delta c_p = c_p \cot\theta \, \Delta\phi \qquad (5\text{-}3)$$

The sensitivity for this simple model is large for events with high phase velocities. At $c_p \cong 7$ km/sec, for instance, an inclination of one degree would change the estimated velocity by 500 m/sec. If, in an expanded model, a gently varying layer at the seabed was above a set of strictly horizontal layers, than phase velocity estimates at the array could be corrected by adequately sampling the bathymetry along the line and using eq. 5-3 to correct for various inclinations encountered. Because of the proximity of the experiment to the East Pacific Rise, however, the bathymetry in the ROSE area was extremely complex. Figure 5-8 is a diagram of sampled depths for line 2S, at the locations of the emerging rays, with approximate bottom inclinations.

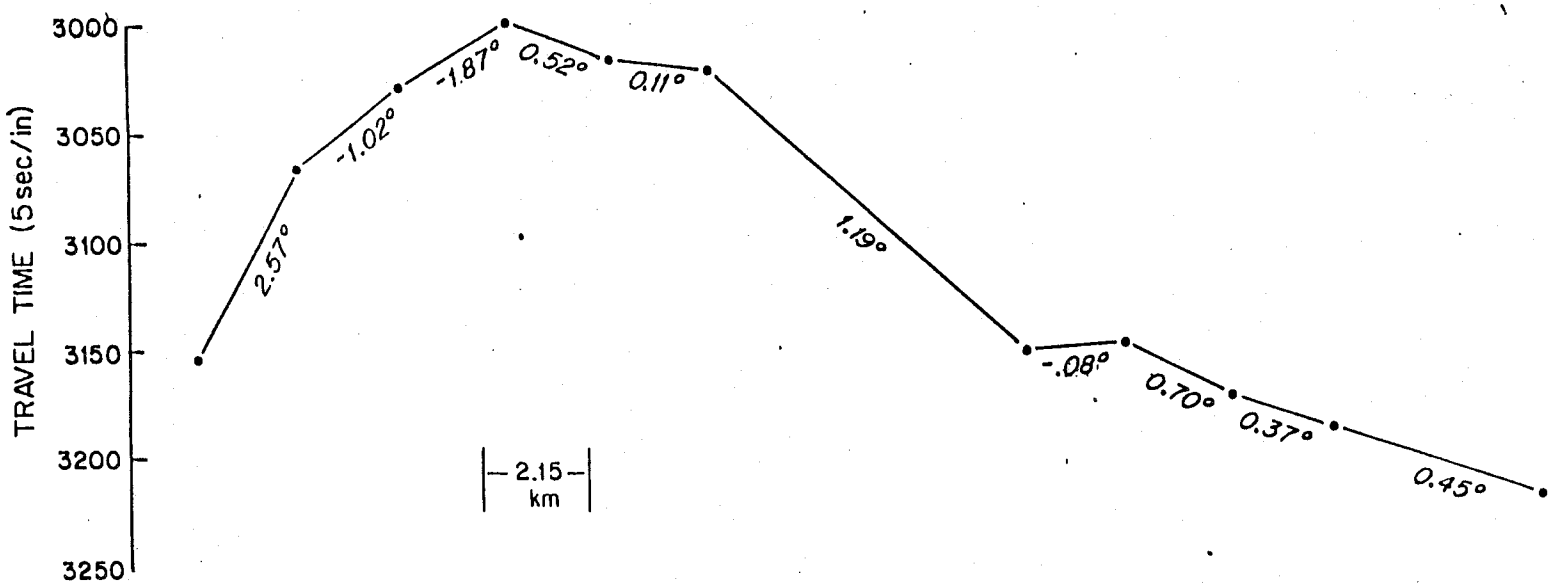

Fig.5-8
Sampled depths below receiving ship during ROSE experiment line 2S
with approximate inclinations at locations of emerging rays

Bottom slopes in the 2° to 3° range were not uncommon and phase velocity estimates with the simple model just mentioned, could be more than 1 km/sec in error. Unfortunately, we obtained depth samples only at intervals of 1 km or more (on the order of the ESP array length), and attempts to correct the velocity estimates have not been fruitful.

In this situation, although raw velocity estimates from the velocity spectral analysis routine are suspect, the ability to discern the relative difference in phase velocities of sequential events is still of use. In figures 5-9a and 5-9b, travel time/offset plots for two ESP lines (2S and 2L) are shown. These figures were constructed from range information generated by the RAYDIST unit and travel times based on the first water arrival (1W). Although a more accurate system for measuring arrival times would be required for in depth analysis, the ability to discriminate relative phase velocity at the array did produce fruitful results. Estimated velocities are divided into three categories: low (1500 to 3500 km/sec), medium (3500 to 5500), and high (5500 and above). The suite of prominent arrivals in time are plotted vertically. The "doublet" (and sometimes "triplet") phenomenon of closely spaced high velocity events are indicated in the circles. In fig. 5-9a, with fairly dense shot spacing, we were able to discern two distinct first arrival slopes. The first at 6.6 km/sec would correspond to the approximate sound speed in layer 3 while the slope (7.8 km/sec) at the largest offset indicates a MOHO refraction. Since upper mantle velocity is normally 8.2 km/sec (Lewis, 1978) in older regions, this lower estimate is in accord with the "anomalous mantle" in fig. 23 of Christensen & Salisbury (1975).

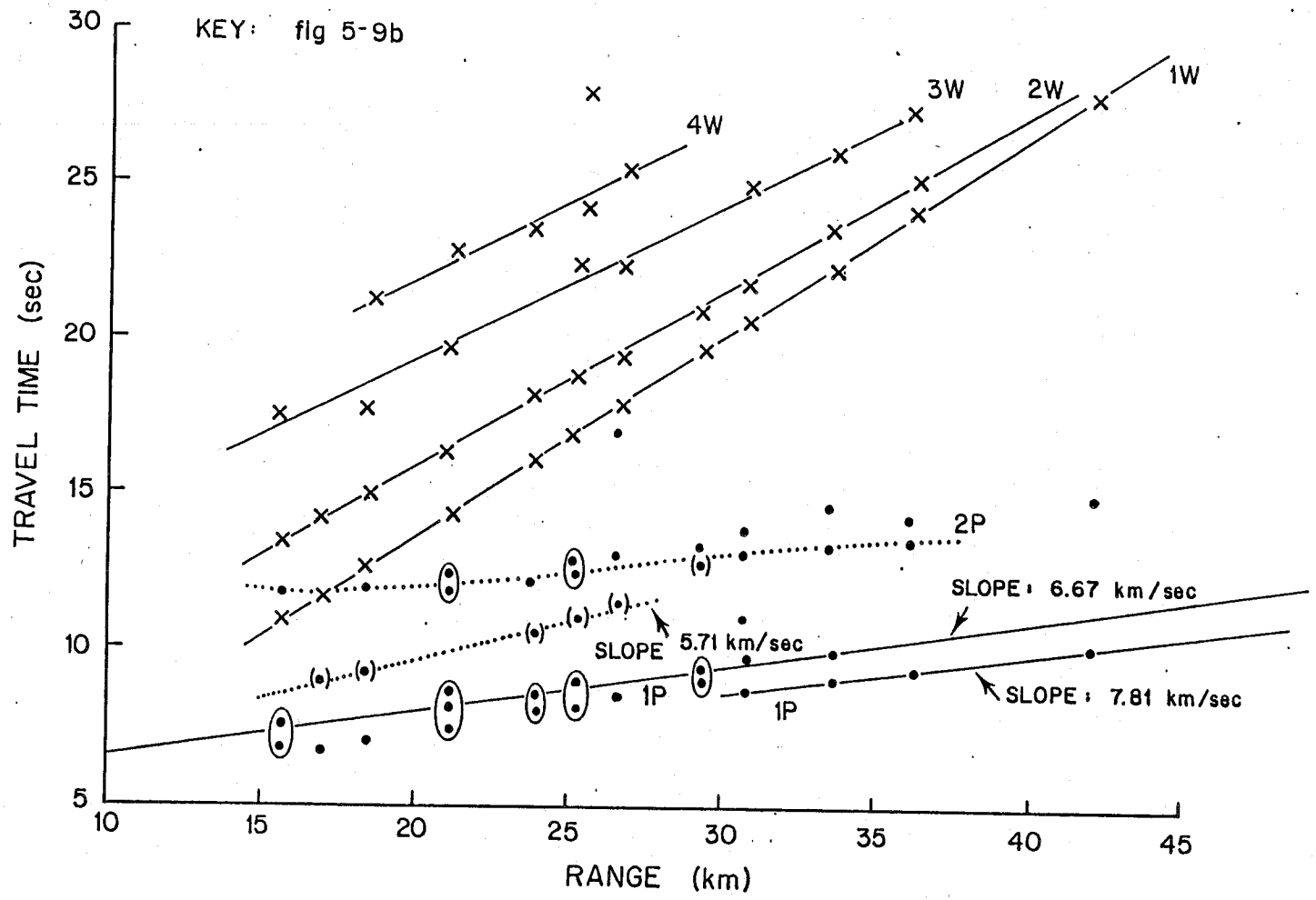

Fig.5-9a
Travel time/ offset diagram for ROSE line 2S using relative phase velocity information obtained with MLM routine.

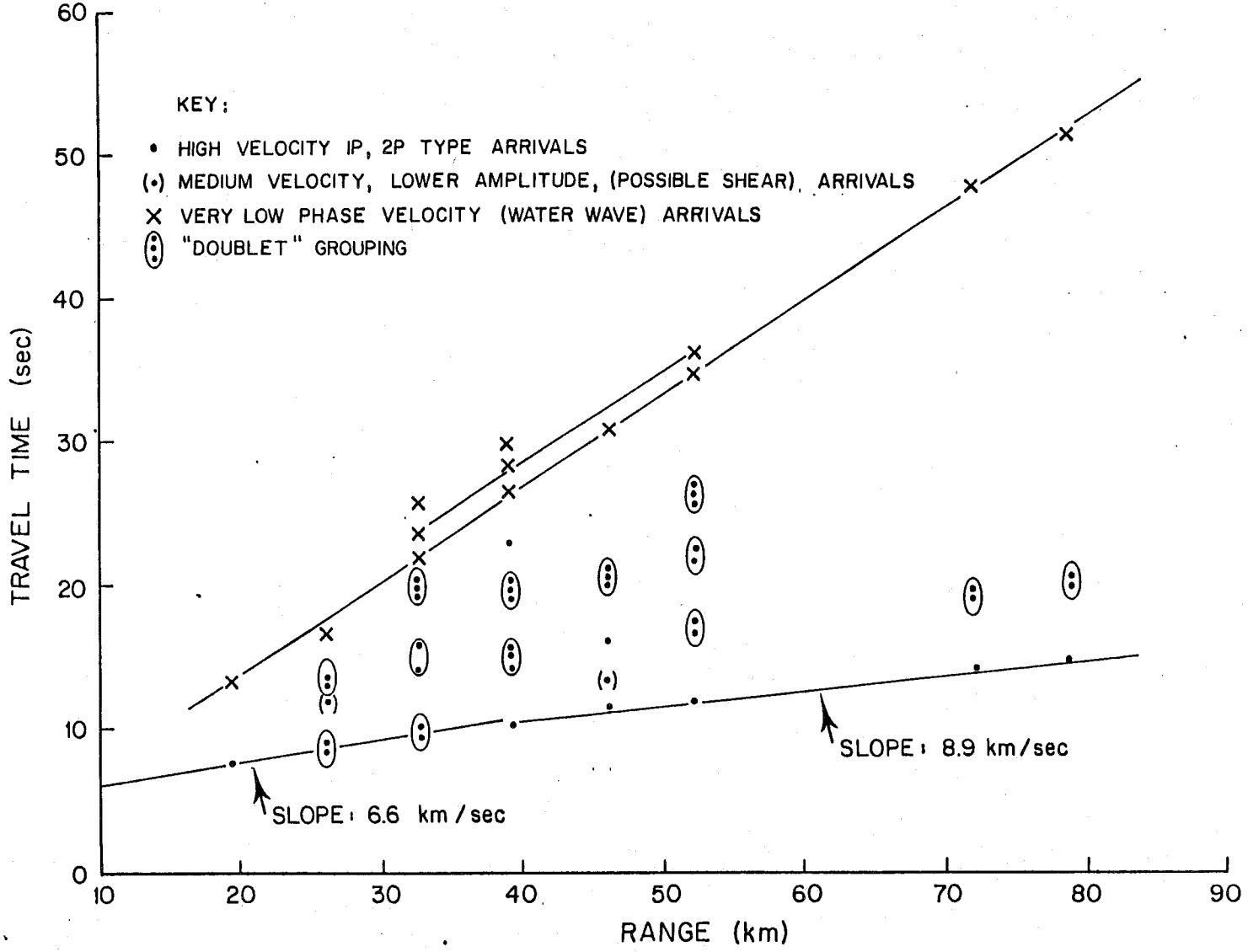

Fig.5-9b
Travel time/ offset diagram obtained for line 2L.

A consistent set of "medium" MLM estimates, occurring after the first arrival with an approximate slope of 5.7 km/sec, confirms the presence of "layer 2" events . Because average crustal shear velocity is about 4 km/sec, the possibility of these "medium" velocity events being converted shear arrivals is ruled out. The refraction/reflection (2P) events are seen in the line parallel to the locus of first arrivals. As many as four low phase velocity water arrivals can also be seen, the lines formed by these events on the T-X diagram all tending to converge at large offsets.

In figure 5-9b, although the refraction line was actually run out to ranges in excess of 100 km, water wave data was not available to us beyond 80 km, at which point travel time calculations could not be continued. First arrivals indicate both a 6.6 km/sec, and a higher (8.9 km/sec) slope, intersecting at a range of 30 km. This extremely high mantle velocity estimate is due to errors caused by calculating first arrival slopes from sparsely sampled data. In this line there is only one "medium" velocity event, at 26 km, that may be a layer 2 arrival. The "doublet" phenomena is especially prominent in 2P and 3P refraction/reflections, and, at 40 & 52 km, a "4P" arrivals occur.

Although extremely rough bathymetry and errors in position information lessen the accuracy of velocity estimates from one shot alone, we have shown that knowledge of the relative values of velocity estimates in one experiment can still aid in the interpretation of a travel time-offset diagram of refraction data. Furthermore, we have been able to identify events beyond the

first arrival and can discriminate arrivals from different trajectories that appear simultaneously at a receiver.

The interpretations of the MLM estimates of the first arrivals in the T-X plot are supported by the fact that, at a range of 30 to 40 km, the replacement of layer 2 events as first arrivals by higher velocity mantle refractions is a common occurrence. An increase in amplitude at this distance occurs frequently, as discussed in Chapter II. In chapter VI, we use level estimates from the MLM routine, calculate crustal transmission losses, and determine estimates of this energy focusing at these ranges.

CHAPTER VI

TRANSMISSION LOSS CALCULATIONS

We now describe the procedure followed in taking values of $\hat{P}(f,\underline{\nu})$ generated by the MLM algorithm and calculating numerical estimates of transmission loss for ROSE refraction events. We have shown that the frequency/wavenumber estimates represent energy arriving at the array partitioned with respect to both temporal and spatial frequencies (power per Hertz per steradian). The relation between the estimates and the acoustic quantities defining transmission loss is first presented. We then discuss five corrections that are applied to $\hat{P}(f,\underline{\nu})$ so that valid TL estimates are produced. The method followed in the calculation of source level (SL) for each shot is also described. Estimates of transmission loss versus range are then presented for ESP lines 2S and 2L. The particular paths for which transmission losses are calculated are 1P, 2P, 1W, and the "layer 2" arrivals.

Relation of Transmission Loss and Frequency/Wavenumber Estimates

Transmission loss at a point $\underline{r}$ is defined as (from Clay & Medwin,1977):

$$TL(\underline{r}) = SL - SPL(\underline{r}) \qquad (6\text{-}1)$$

SL denotes the source level:

$$SL = 10 \log \frac{\widetilde{p^2}(R_{ref})}{p^2_{ref}\, R^2_{ref}} \qquad (6\text{-}2)$$

where $\widetilde{p^2}(R_{ref})$ is the mean square pressure at reference distance R_{ref}. SPL($\underline{r}$) is the sound pressure level at $\underline{r}$:

$$SPL(\underline{r}) = 10 \log \frac{\widetilde{p^2}(\underline{r})}{p^2_{ref}} \qquad (6\text{-}3)$$

In this chapter, the reference distance used is R_{ref} = 1 meter, and the root mean square reference pressure is p_{ref} = 1 μPa. The mean square pressure is related to the spectral density, $\mathcal{S}_p(f,\underline{r})$ by:

$$\tilde{p}^2(\underline{r}) = \int_0^\infty df\, \mathcal{S}_p(f,\underline{r}) \tag{6-4}$$

If the sound field is modelled as a stationary random process, then $\mathcal{S}_p(f,\underline{r})$ is equivalent to the spectral covariance function of the random pressure process: $\mathcal{S}_p(f,\underline{r}) = S_p(f, \underline{r}_i - \underline{r}_j)$ at $\underline{r}_i = \underline{r}_j = \underline{r}$. Both describe the density of energy with respect to temporal frequency, f, at location $\underline{r}$.

For a homogeneous process, the covariance function can be written as:

$$S_p(f,0) = \int d\underline{\nu}\, P_p(f,\underline{\nu}) \tag{6-5}$$

where $P_p(f,\underline{\nu})$ is the frequency/wavenumber function of the random pressure process. The mean square pressure can then be written as:

$$\tilde{p}^2(\underline{r}) = \int df \int d\underline{\nu}\, P_p(f,\underline{\nu}) \tag{6-6}$$

$P_p(f,\underline{\nu})$ thus represents the density of energy per Hz. per steradian.

In Chapter IV, an acoustic event resulting from an explosive source in a refraction experiment was modelled as a windowed segment of a unidirectional plane wave $p_o(\cdot)$, propagating in a direction $\underline{\nu}_p / |\underline{\nu}_p|$. The frequency/wavenumber function of this model process is impulsive, i.e. $P_p(f,\underline{\nu}) = P_o(f)\,\delta(\underline{\nu} - \underline{\nu}_p)$, where $P_o(f)$ is the power spectrum of $p_o(\cdot)$. By substitution, eq. 6-6 can then be rewritten as:

$$\tilde{p}^2(\underline{r}) = \int_0^\infty df \int d\underline{\nu}\, P_o(f,\underline{\nu})\,\delta(\underline{\nu} - \underline{\nu}_p) = \int_0^\infty df\, P_o(f,\underline{\nu}_p) \tag{6-7}$$

In the MLM algorithm, estimates of the frequency/wavenumber function are made for a set of center frequencies, f_o, in bands of width W. We assume the estimated function is approximately constant over W so that:

$$\tilde{P}^2_{f_o,W}(\underline{r}) \approx P_o(f, \underline{\nu}_p)\, W \tag{6-8}$$

$\tilde{P}^2_{f_o,W}(\underline{r})$ is the mean square pressure in a frequency band centered at f_o with width W.

In estimating transmission loss, we choose an event represented by a large value of the estimated wavenumber function, $\hat{P}(f, \underline{\nu}_t)$ and consider the event as an arrival of the model process at $\underline{\nu}_t = \underline{\nu}_p$. The transmission loss for the chosen event at $\underline{\nu}_t$ is then:

$$TL_{f_o,W}(\underline{r}) = SL - SPL_{f_o,W}(\underline{r}) \tag{6-9}$$

where:

$$SPL_{f_o,W}(\underline{r}) = 10\log \frac{\tilde{P}^2_{f_o,W}(\underline{r})}{p^2_{ref}} = 10\log \frac{\hat{P}_p(f, \underline{\nu}_t)\, W}{p^2_{ref}}$$

$$= 10\log \frac{\hat{P}(f_o, \underline{\nu}_t)\, \Delta f_{ref}}{p^2_{ref}} + 10\log \frac{W}{\Delta f_{ref}} \tag{6-10}$$

We choose $\Delta f_{ref} = W$ so that:

$$TL_{f_o,W}(\underline{r}) = SL - 10\log \frac{\hat{P}_p(f_o, \underline{\nu}_t)}{p^2_{ref}} \tag{6-11}$$

This is a modified version of eq 6-1 with $TL_{f_o,W}(\underline{r})$ representing the loss in a specific frequency band arriving at the receivers at the angle $\underline{\nu}_t / |\underline{\nu}_t|$

Corrections to MLM Estimates

Before eq 6-11 can be implemented, we must relate $P_p(f, \underline{\nu_t})$, the frequency/wavenumber function of the model pressure field with $P_x(f, \underline{\nu_t})$, the quantity actually estimated in the MLM algorithm from the sampled data points on the magnetic tapes. Five corrections to $P_x(f, \underline{\nu})$ are needed to remove effects of: i) sampling in time and frequency; ii)artifacts of receiver location (Lloyd mirror effect); iii) array gain, iv) hydrophone sensitivity, and v) MLM bias.

Sampling Correction

In Appendix 6-1, it is shown that the spectral density function, for windowed segments of length T, sampled at the Nyquist interval ΔT, can be written as:

$$\mathcal{S}(f_0, \underline{r}) = \frac{(\Delta T)^2}{T} \left[\sum_{k=k_0 - M/2T}^{k=k_0 + M/2T} \frac{|P(k\Delta f)|^2}{M} \right] \quad (6\text{-}12)$$

M is the number of Fourier coefficients, $P(k\,\Delta f)$, in W. k_o is the coefficient number corresponding to f_o. If we compare eq 6-12 with eq 4-34c, the term in the above bracket is recognized as the implemented expression for the diagonal elements of the estimated covariance matrix, $\left[\hat{S}_{ij}(f)\right]$. In order that the estimated matrix be equivalent to the spectral density function, $\mathcal{S}(f, \underline{r})$, a correction due to sampling: $e = \Delta T^2 / T$, is applied to the matrix. This same correction must be applied to the MLM frequency/wavenumber estimates.

In the ROSE data set, T = .004 sec., and the effective data length (after windowing) was T ~ .5 sec. so that a correction of:

$$10 \log e = 10 \log \frac{(.004)^2}{.5} \approx -45 \text{ db}$$

was subtracted from 10 log P(f,) for all of the experiments.

Lloyd Mirror Correction

The Lloyd mirror effect is important in characterizing the sound field near a free surface, especially at low frequencies, where wavelengths are greater than the dimension of the average surface roughness so that reflection is specular. A correction for this effect was necessary for data received with the horizontal (ESP) array. At an approximate depth of 10 meters, surface reflections, when added to arrivals from below, significantly alter the amplitude of the waveform at a sensor. Referring to Fig. 6-1, EDA represents a pure sinusoidal plane wavefront with frequency f, arriving at a sensor at point A at time t. The vertical angle is α and hydrophone depth is BA = d. The sensor will also be influenced at this moment by a surface reflected arrival that has traversed the extra distance DC + CA. The necessary correction for this effect, as shown in Appendix 6-2, is:

$$20 \log \left| 2 \sin \left(\frac{2\pi f d \cos \alpha}{c_o} \right) \right| \qquad (6\text{-}13)$$

Typical correction curves for different frequencies, f, versus vertical angle, α ,are shown in fig. 6-2. Since estimates were performed across a 3 or 4 Hz band, corrections were averaged across each band. For high phase velocities, this factor is on the order of 3 db at 8 Hz. For each event, the estimated angle of arrival obtained with the MLM algorithm was used in eq. 6-13. The frequency averaging is particularly important at large vertical angles (water arrivals) since corrections are large and sensitive to frequency

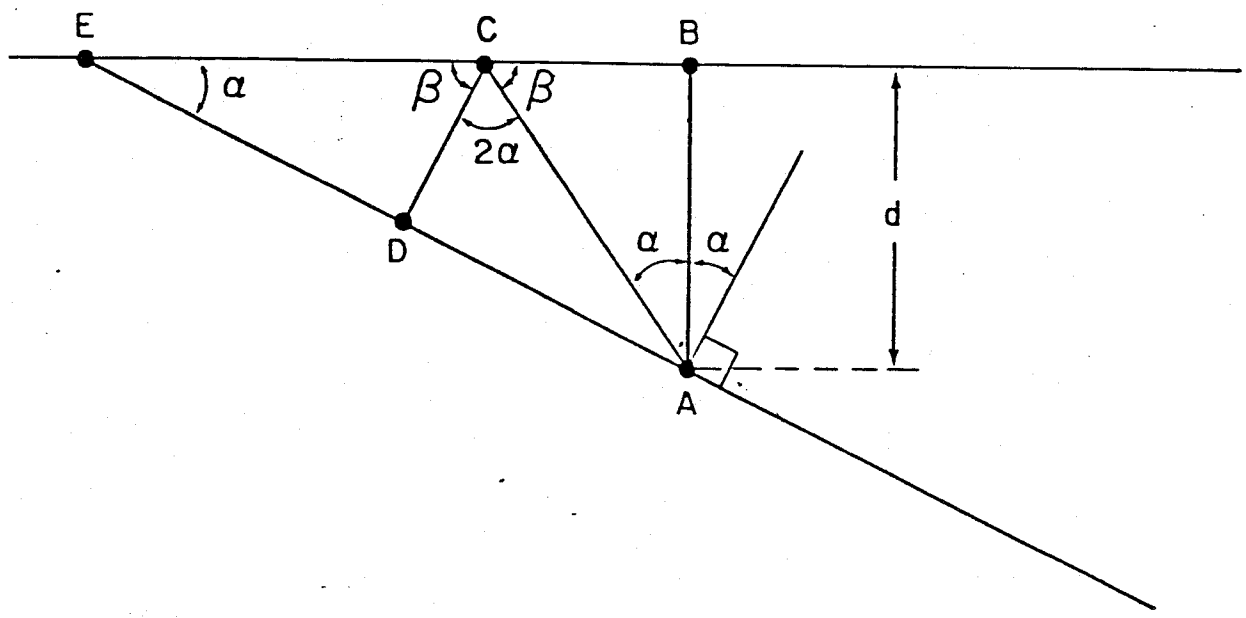

Fig.6-1
Geometry used in discussion of Lloyd mirror effect.

$$20 \log \left| 2 \sin \left(2\pi \frac{fd \cos \alpha}{C_o} \right) \right|$$

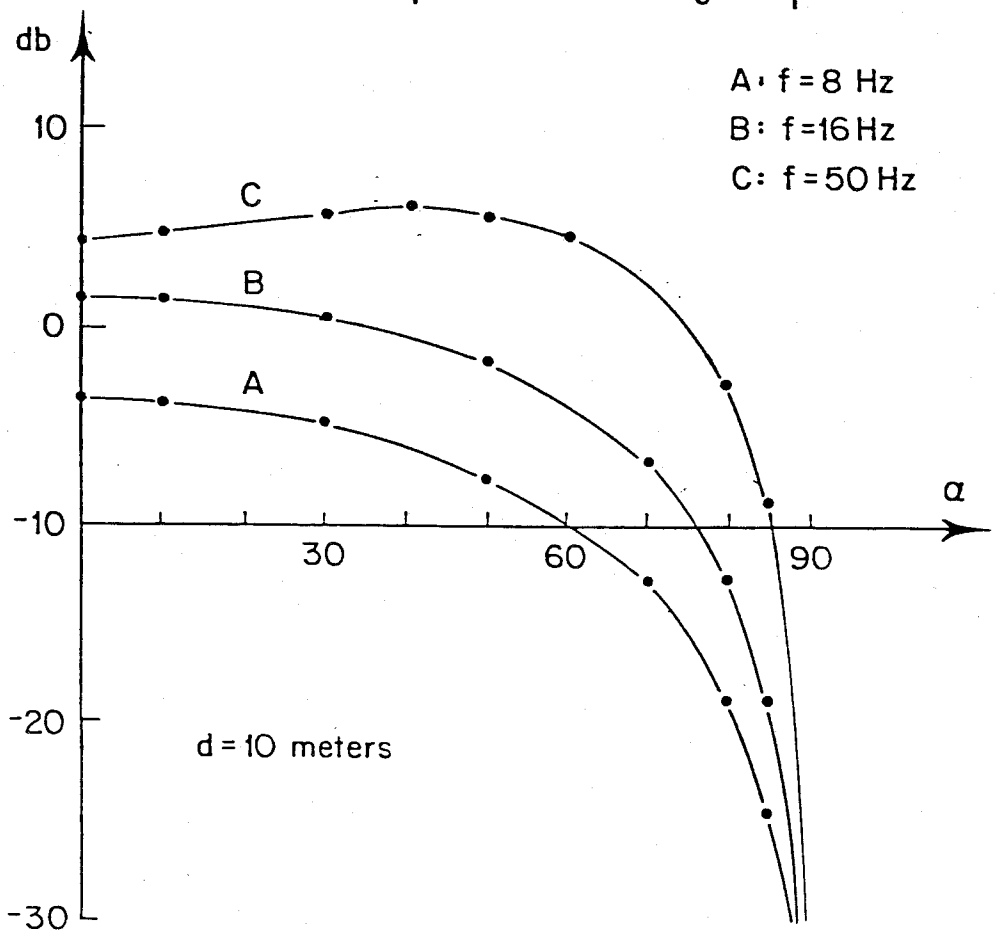

Fig. 6-2
Lloyd mirror effect versus vertical angle for 3 frequencies.

where predicted amplitudes are small. Because of this severe attenuation near endfire, the bottom reflected water wave, rather than the essentially unobservable, higher angle direct arrival, is observed in ESP data.

Array Directivity

Another correction applicable to the ESP array only is due to the fact that each of the 24 "sensors" was actually composed of two fifty meter streamer sections connected in parallel. To correct for directivity effects of each of these small "arrays", each channel is modelled as an unphased 100 meter long line array with beam pattern, from eq. 4-12:

$$\text{sinc}\left[\frac{\pi L}{\lambda}\sin\alpha\right] \qquad (6\text{-}14)$$

where α is the vertical angle. The correction applied to the data due to this effect is:

$$20\log\left[\text{sinc}\ \frac{\pi L}{\lambda}\sin\alpha\right] \qquad (6\text{-}15)$$

which is plotted in fig. 6-3. As with the mirror effect, high velocity arrivals at low angles are not heavily affected by this correction. but they are quite sensitive for water arrivals. Frequency averaging across the estimation band was done for all events.

Hydrophone Sensitivity

The data recorded on the ESP and MABS tapes are the voltages that were present at the output of the acquisition systems. Hydrophone sensitivity corrections are necessary to convert this data into units of sound pressure.

Figure 6-4 is a schematic illustration of the results of a calibration

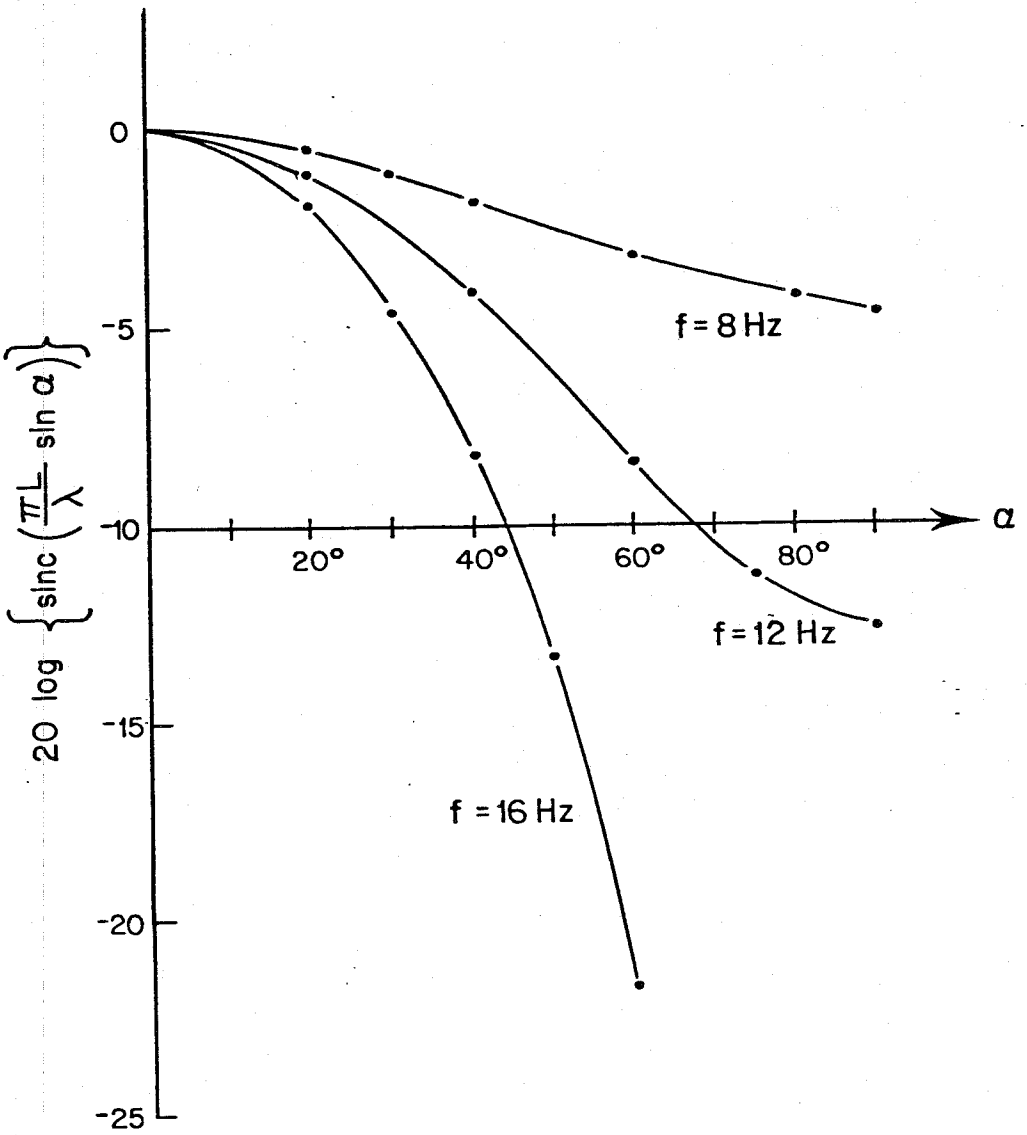

Fig. 6-3
Array directivity effect for 100 meter line array at 3 frequencies.

TABLE 6-1

EXPERIMENT	ARRAY	K	CENTER FREQ	M	γ
2S	MABS	8	8	4	.03
			12	4	.03
			16	4	.03
2S	ESP	12	8	4	.02
			12	4	.02
			16	4	.02
2L (to 45km)	ESP	24	5	3	.03
			8	3	.03
			11	3	.03
			14	3	.03
2L (at 52.5 km)	ESP	24	5	3	.04
			8	3	.04
			11	3	.04
			14	3	.04
2L (52.5 to 104km)	ESP	24	5	3	.01
			8	3	.01
			11	3	.01
			14	3	.01

performed on the MABS array prior to deployment. By averaging over the eight functioning channels, sensitivities of about -125 and -121 db re 1 volt/μPa were found for the 8 Hz., and the 12 & 16 Hz bands, respectively.

The sensitivity of the phones of the ESP array were given as -185 db re 1V per μPa. For impedance matching purposes, the coupling of each streamer section to the ship made use of a 9:1 (18 db) step down transformer, so that the effective sensitivity was about -203 db. Values appearing on the final tapes sent to Woods Hole are in millivolts so that, for data processing purposes, the effective sensitivity for the ESP array is:
(-203 + 60) = -143 db re 1V/μPa.

MLM BIAS

Table 6-1 outlines the important parameters that were used in the MLM processing and bias calculation for the ROSE data. The "white noise" factor, γ was varied during the processing of line 2L.

Using the correction procedure discussed in Chapter IV, we first used the background levels of each shot to provide us with an estimate of σ^2. This was done for all experiments and in all the various frequency bands. The results were then averaged to provide the following values of σ^2 used for bias correction:

Line 2L, ESP array:	σ^2 = .004	at 5 Hz
	" = .0035	at 8 Hz
	" = .003	at 11 Hz
	" = .002	at 14 Hz
Line 2S, ESP array:	σ^2 = .0035	at 8 Hz
	" = .003	at 12 Hz
	" = .002	at 16 Hz

Fig. 6-4
MABS hydrophone sensitivities.

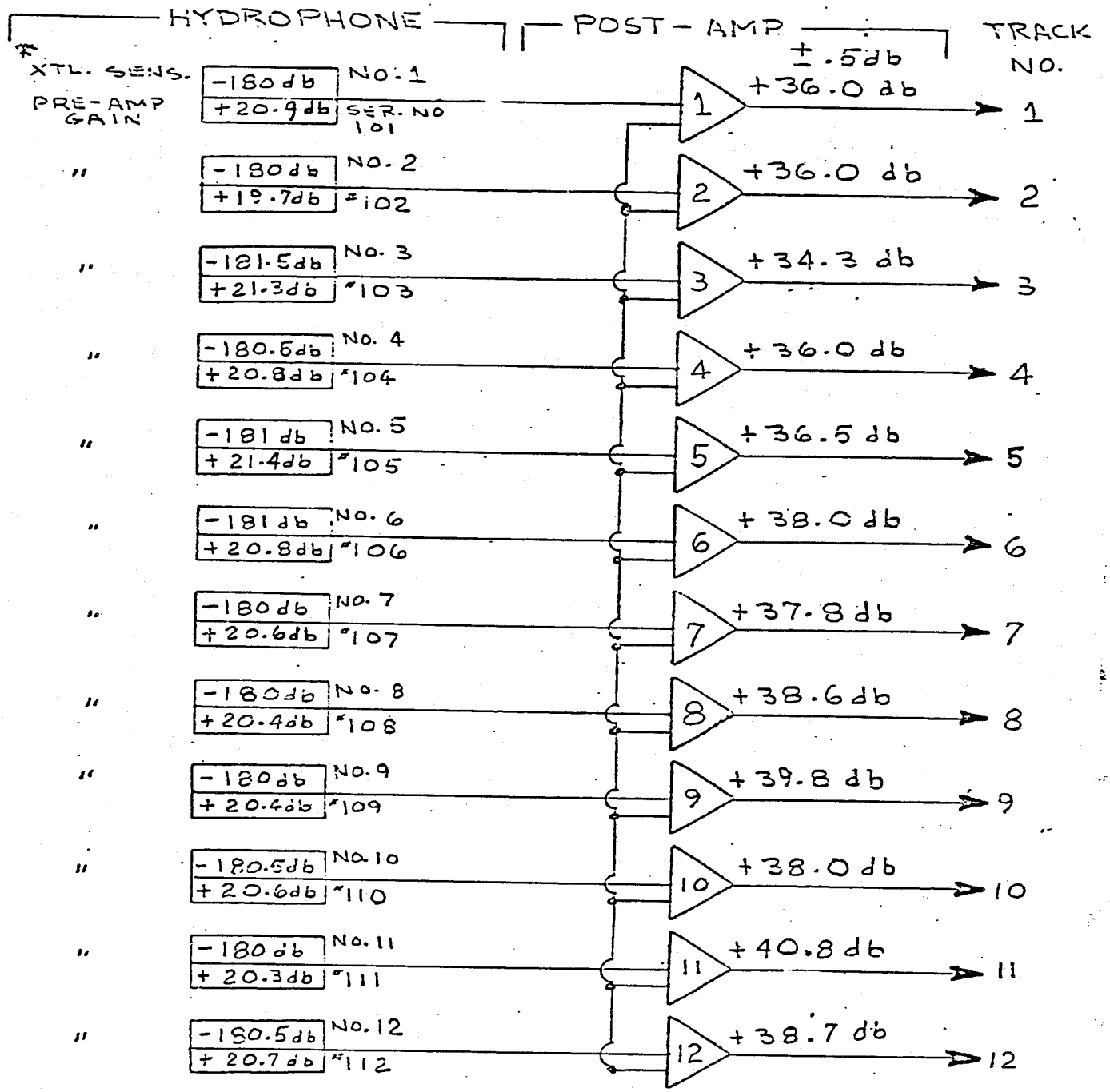

* NOTE:
CRYSTAL SENSITIVITY - db // 1 V / μ Pa AT 5 HZ
PRE-AMP GAIN - db // 1 V AT 5 HZ
POST-AMP GAIN - db // 1 V AT 15 HZ

Line 2S, MABS array:	σ^2 = .175	at 8 Hz
	" = .175	at 12 Hz
	" = .175	at 16 Hz

The difference in σ^2 levels between the MABS and ESP is about 17 db corresponding to the difference in hydrophone sensitivities. With σ^2 known, $\hat{P}$ versus $\hat{P}_{corr}$ curves (as in figures 4-15 and 4-16) were drawn for all necessary combinations of γ , M, σ^2, and K needed in Table 6-1. and the necessary corrections were found from these curves.

Since MLM bias is a function of γ , a test of the bias correction procedure was performed with actual data using different values of this parameter. The MLM routine was run five times on a two second set of data that included the 1P arrival at 8 Hz in Figure 5-4a. For each run, γ was changed, its value ranging from .01 to .05 in increments of .01. The results, 10 log $\hat{P}$, plotted in figure 6-7, varied by 5 db, due to bias dependence on γ . With bias corrections, the corrected levels, 10 log $\hat{P}_{corr}$, remain within 1 db of each other.

Source Level

For each shot point in the Rose experiment, the explosive weight and an estimated shot depth, based on sinking rate and source monitor times, were known. Employing this information in an empirical relation (Wakely, 1977), an expression for the pressure waveform at a range R was computed. The model waveform includes four bubble pulse periods following an initial shock pulse. The waveform was Fourier transformed and the squared magnitude of the resulting components were averaged across the estimation bands in the data.

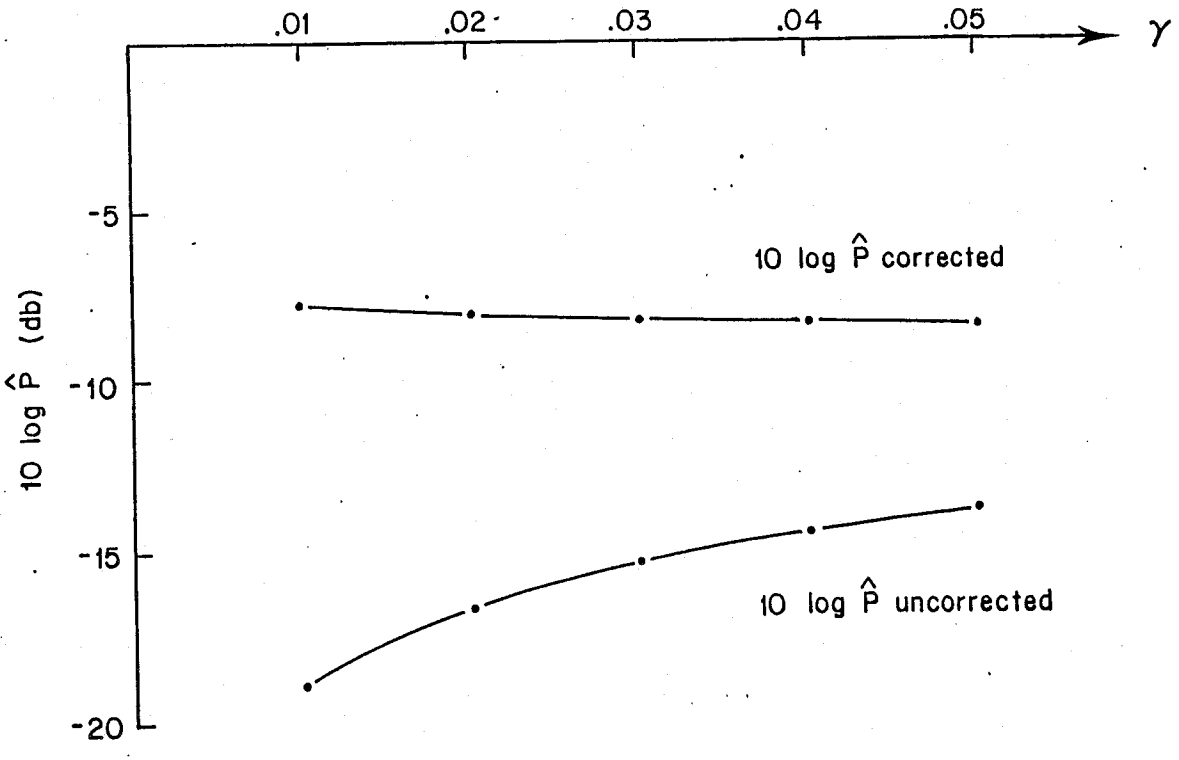

Fig. 6-5
Variation of MLM estimates with added artifical "white noise" term, γ , and the reduction of this variation after bias corrections are applied.

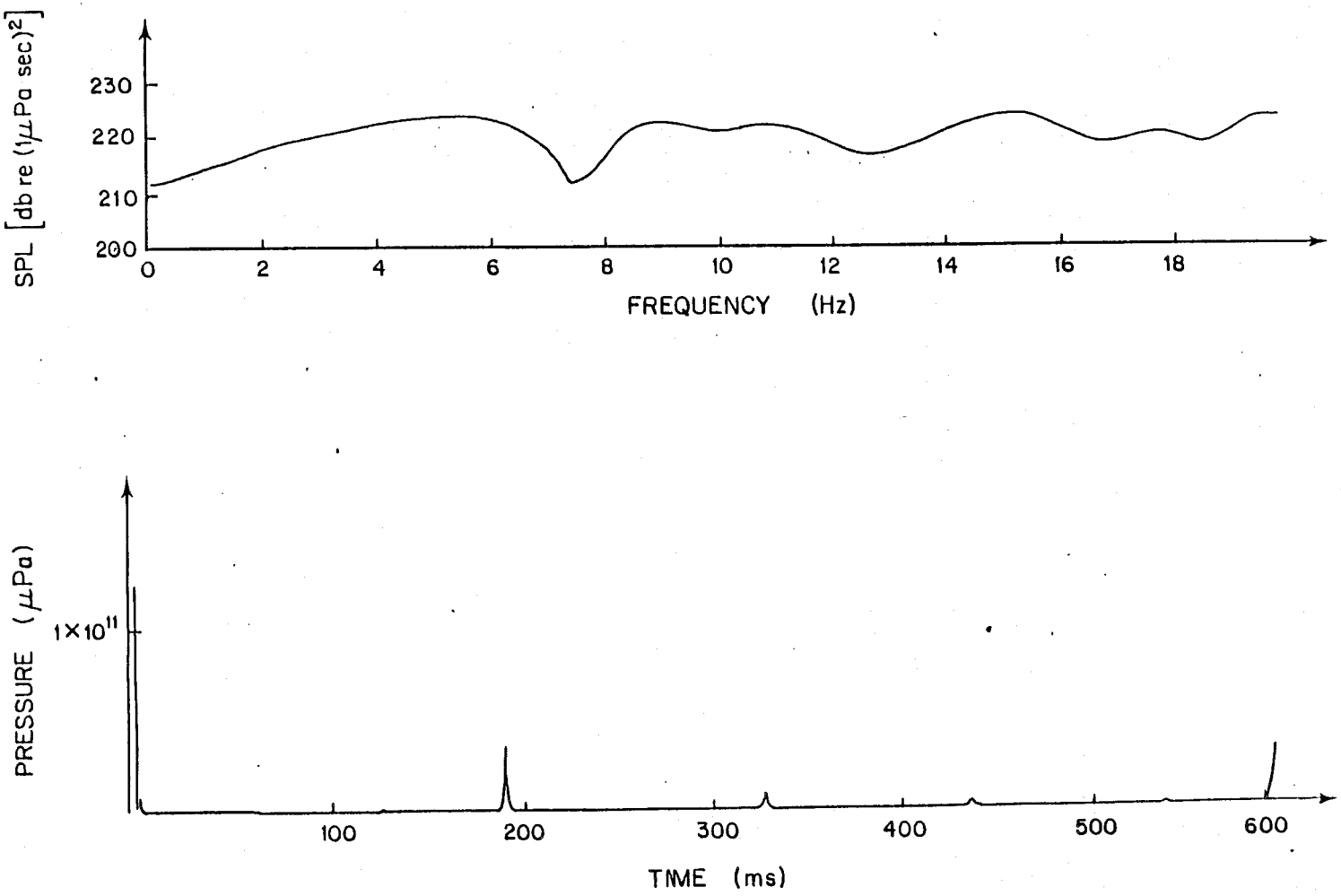

Fig. 6-6
Typical source signature and source spectral level for
25 pound charge detonated at 35.9 meters obtained with Wakely formula.

After correcting back to a 1 meter range, the results became the source pressure levels used in the TL calculations. In Fig. 6-5, representative temporal and spectral profiles for a 25 lb charge detonated at 35.9 meters are shown. For this shot, the averaging in frequency was particularly important in the 8 Hz band because of a 10 db dip in the level near 7.5 Hz. Since the shock wave intensity in all shots used in our work was above the cavitation limit, the energy near the sources was incoherent and a Lloyd mirror correction at the shot points would not be valid. Source level behavior from a cavitating shock wave at the surface is a nonlinear acoustics problem which still needs analysis.

Implemented transmission loss equation

Applying the five corrections outlined above, the expression for partitioned transmission loss in eq. 6-11 can be rewritten as:

$$TL_{f_o,w}(\underline{r}) = SL(f_o) - \left[10\log \hat{P}_x(f,\underline{\nu}) - 20\log S + 10\log e - 20\log LM - 20\log AD\right] \quad (6\text{-}16)$$

where S denotes hydrophone sensitivity, e is the sampling correction, and LM and AD are the mirror effect and array directivity corrections, respectively. LM and AD effects were not applicable to the vertical array (MABS) estimates. $\hat{P}_x(f, \underline{\nu})$ represents the magnitude of the frequency-wavenumber estimate after bias correction. Results obtained from the use of this expression are now presented.

Transmission Loss Estimates for 1P events

In figure 6-6, TL estimates at 8 Hz for the first major event (1P) in both MABS and ESP data from lines 2S and 2L are shown up to an offset of 42 kilometers. Line 2S shots consisted of alternating 5 and 25 lb charges. Only 25 lb shots are used in the processing of MABS data from this line, but both sizes are included in the estimates for the ESP data, with the 5 lb shots being indicated in the figure. Line 2L at these offsets used 180 lb charges exclusively. The following points should be noted:

i) Line 2S shots with 5 lb charges generally have higher TL estimates than those using 25 lbs. A bolder line is drawn through points corresponding to 25 lb charges only. The approximate 5 db difference in the calculated TL for 5 and 25 lb shots is probably due to errors in source level estimates. The depths at which both size charges detonated were roughly the same (40 m.), so that Lloyd mirror corrections on the source levels, even if they were valid, would not change the relative difference in the estimates.

ii) If we ignore the 5 lb data and note that line 2L was processed with 24 channels, the ESP 2S data with 12, and the MABS with 8, we can see a steady progression in the TL curves with the data with the least number of sensors having the least loss. The difference in the estimates for line 2L data and 2S data could again be due to error in source level estimates, line 2L having used 180 lb charges. The approximate 5db mean difference of the 25 lb. MABS and ESP 2S data, however, cannot be caused by the use of erroneous source levels. The discrepancy may be attributed to: a) the fact that, geographically, the MABS and ESP 2S data are samples of different locations

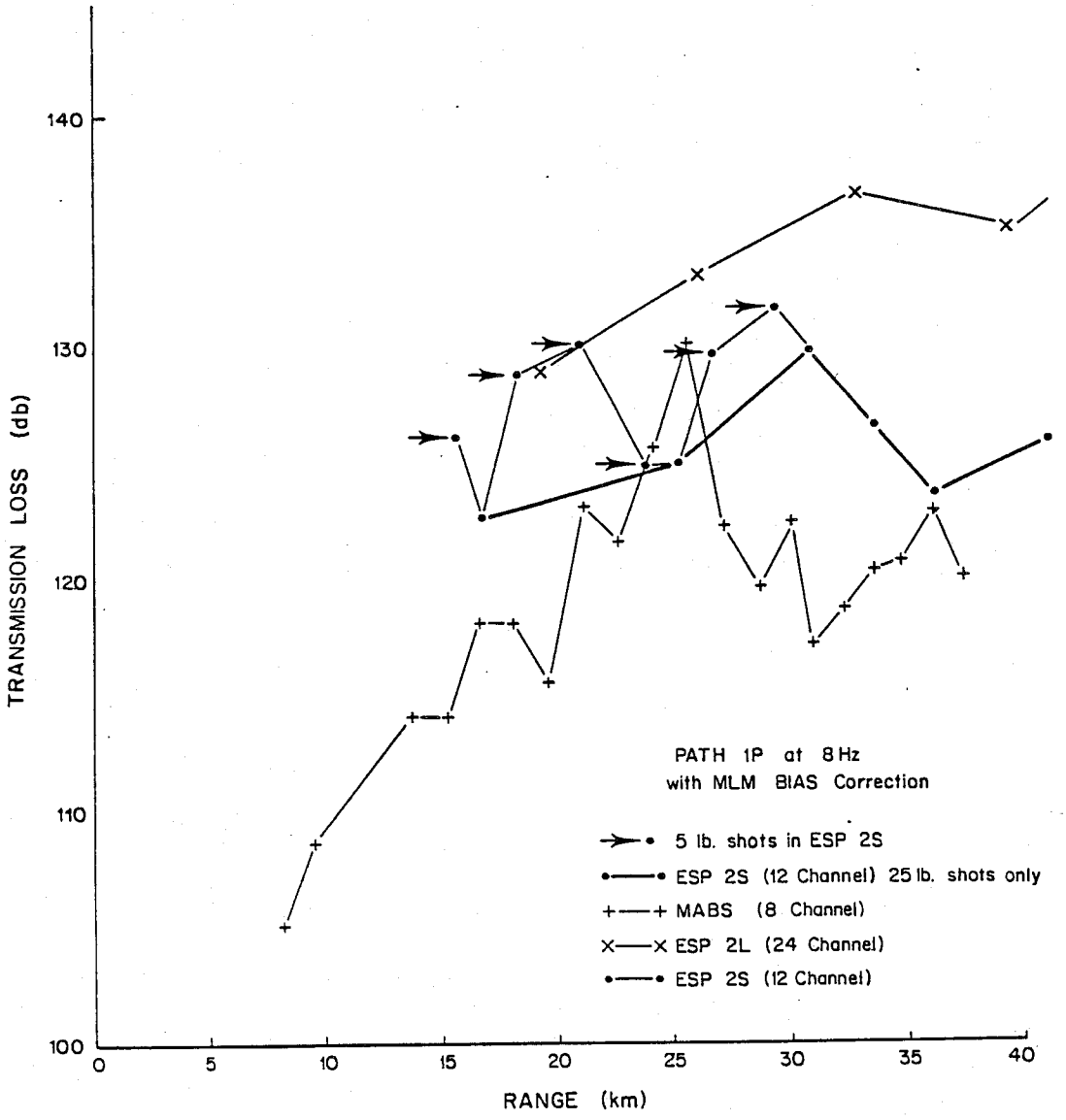

Fig.6-7
Results of transmission loss calculations on first arrivals (1P) at 8 Hz for ESP lines 2L and 2S, including vertical (MABS) array data.

and the crust is not laterally homogeneous; b) statistical fluctuations in the MLM estimator; and c) errors in MLM bias correction. Since the bias corrections employed are based on empirical results and since MLM bias is very sensitive to the number of sensors used, the latter is probably more significant. If we look at fig. 6-7, however, in which TL estimates for the same set of data are shown without bias corrections, we can see that the variation of the estimates with the number of sensors used has been significantly reduced in the corrected set.

iii) There is a consistent drop in TL for all 3 data sets between the ranges of 25 and 40 km. As we have mentioned, this is often encountered in refraction data. This drop is about 6 db in 2S ESP data, 10 db in 2S MABS, but only 2 db in the 2L data. The latter, however, is undersampled so that evidence for a greater focusing effect between offsets of 33 to 40 km may have been missed.

Figure 6-9 illustrates the results produced when TL estimates for line 2L, out to a range of 104 km, are calculated for 4 separate frequency bands and are "corrected" for geometrical spreading. A value, 10 log r^2 (r being the horizontal offset in meters), was subtracted from each TL value. In this drawing, an ideal pressure wavefront with a simple spherical attenuation would appear as a horizontal line. We observe that the actual loss in the crust increased with range somewhat faster than the r^2 dependence. Assuming the geometrical factor has been accounted for, this added loss reflects the absorption of energy that has taken place along the path. In this figure, the "resonance" phenomenon of a low point in TL between offsets of 30 and 40 km

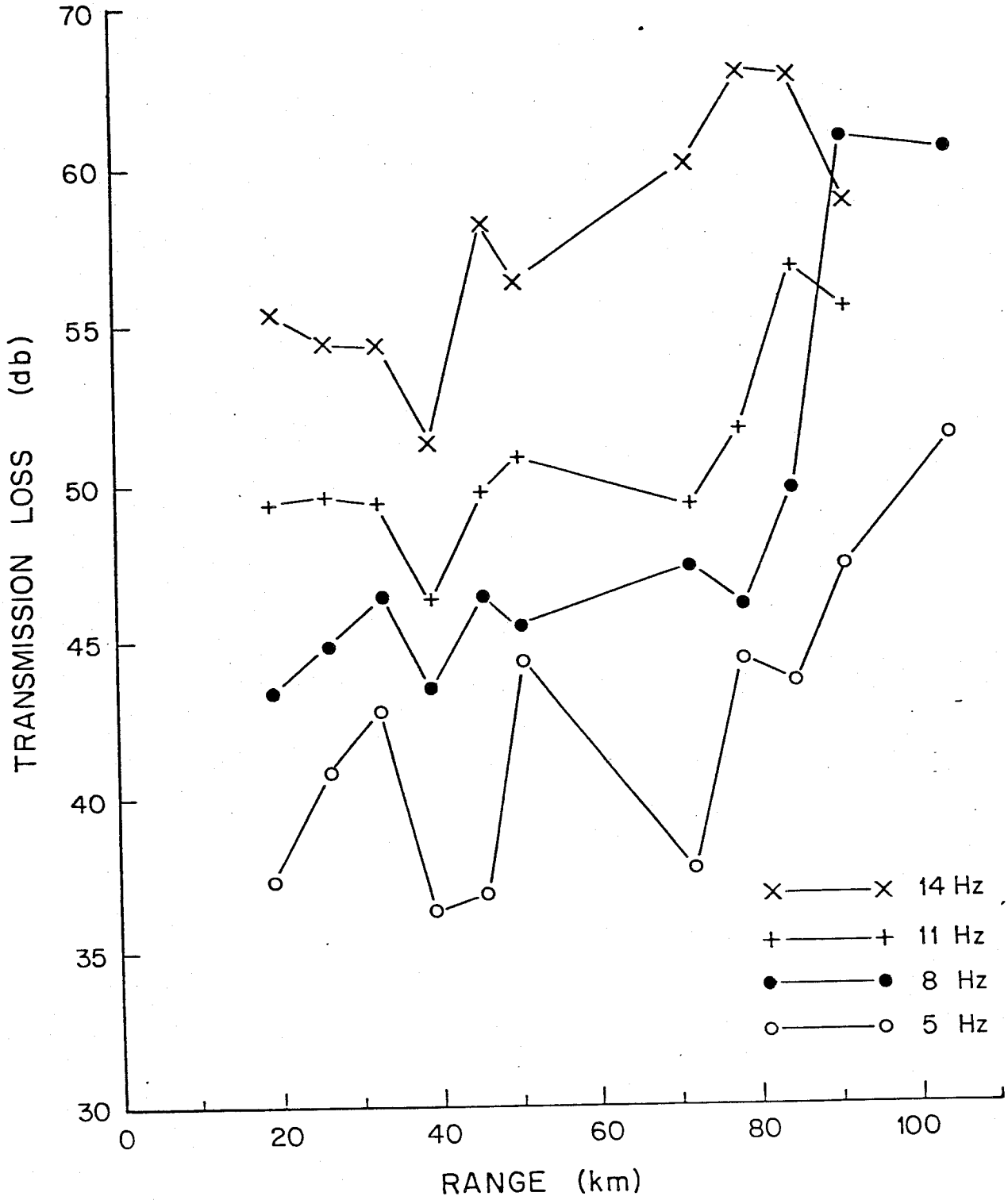

Fig. 6-9
Transmission loss estimates at 5, 8, 11 and 14 Hz for line 2L data.

appears more dramatically for line 2L data than in figure 6-7 because of the geometrical spreading factors applied.

Parameters of linear regression applied to TL estimates

In Table 6-2, the results of applying a linear regression to transmission loss estimates versus offset are presented. The parameters of the regression tabulated are:

N	the number of TL estimates used in the regression;
α (db/km)	the slope of the fitted line with respect to offset, indicating loss above (or below) geometrical losses due to absorption and other effects;
β (db)	the intercept at zero offset of the regression which is an indication of "insertion losses" such as reflection losses at layer boundaries and transmission coefficients;
ρ	the "coefficient of determination" or correlation coefficient indicating the quality of fit achieved by the regression. Values closer to 1 indicate a better fit than values near zero;
σ	the standard deviation of the regression
Q	a dimensionless attenuation factor: the ratio of energy stored in one cycle to the energy lost during the cycle: $Q = \frac{\pi f}{c_p \alpha} \cdot 20 \log e$ (Clay & Medwin, 1977)

Regression results for path 1P from line 2L in table 6-2 are presented for the entire line and also separately: i) for offsets up to 35 km; and ii) for offsets beyond 35 km. The correlation coefficients for the latter two sets are consistently higher than for estimates made from the entire line, since

Path	Data Set	Center Freq. (Hz)	N	α (db/km)	β (db)	ρ	σ	Q
1P	Line 2L	5	11	.12	34.59	.53	3.22	162
	(20 to	8	11	.17	38.13	.66	3.38	183
	104 km	11	10	.09	45.29	.54	2.01	476
	offset)	14	10	.11	50.66	.63	2.06	496
1P	Line 2L	5	3	.45	28.33	.98	.34	43
	(20 to	8	3	.22	38.9	.94	.3	142
	35 km	11	3	-.08	50.8	1.00	.13	-
	offset)	14	3	-.13	57.5	.98	.16	-
1P	Line 2L	5	8	.20	28.56	.69	2.85	97
	(35 to	8	8	.24	32.56	.7	3.39	130
	104 km	11	7	.15	40.58	.73	1.77	286
	offset)	14	7	.15	47.54	.65	2.12	364
1P	Line 2S	8	6	-.13	44.43	.08	2.11	-
	(ESP 5#	12	6	-.93	61.05	.99	.53	-
	shots; 16 to 30 km)	16	6	-.67	60.48	.65	2.35	-
1P	Line 2S	8	3	.23	34.90	.72	.81	136
	(ESP 25#	12	3	.18	37.08	.08	3.39	260
	shots; 17 to 30 km)	16	3	-.50	58.50	.98	.45	-
1P	Line 2S	8	11	.77	22.06	.78	2.23	40
	(MABS; 8	12	11	-.02	40.36	.03	2.63	-
	to 25 km offset)	16	11	-.23	47.46	.37	1.58	-

TABLE 6-2

Results of linear regression for path 1P

the effect of the nonlinear behavior at "resonance" near 35 km is decreased. This division of 2L data is also motivated by the fact that data below 35 km may reflect losses in propagation through "layer 3", while estimates made from data beyond 35 km involve energy that has interacted with the Moho.

The most consistent feature in the results for 2L in table 6-2 is the increase in insertion loss, β , with center frequency. This loss increases an average of 9 db for each 3 Hz increment in frequency. The magnitude and frequency behavior of β is essentially on agreement with the results of Baggeroer and Falconer (1981) for estimates of transmission loss for events interpreted as Moho refractions in the CANBARX experiment. The slopes, α , however, averaging about .2 db/km for line 2L "Moho" data, are consistently lower than those in the CANBARX paper (which is on the order of .5 db/km) and are also lower than attenuations extrapolated from data published by Hamilton (1972), which tends to be closer to 1 db/km. The data in the latter paper is relatively sparse at low frequencies and concerns propagation in marine sediments. Acoustic behavior in basement basalt and/or Moho would be expected to be more efficient as the present results indicate.

As with the Rose data, the estimates in the CANBARX paper are based on crustal refraction data and the procedure used in evaluationg TL is the same as used here except that MLM bias corrections were not performed. The fact that large bias corrections, essentially based on empirical results, were used in the 24 channel 2L data and that similar corrections (although they would be smaller for the CANBARX array, with a maximum of 12 functioning channels) were not applied to the CANBARX data may account for the discrepancy between the

two estimates of α . CANBARX results are also based on data taken from five experiments while the ROSE 2L estimates involve data from up to eleven separate shots.

The values of Q obtained here, in keeping with lower estimates of in ROSE results, are higher than in CANBARX. As such, they tend to be closer to the results of Jacobson (Jacobson et al, 1981) in which values of Q^{-1} , the "specific quality factor", obtained in a sedimentary region in the Bay of Bengal, approached values less than .01 at the greatest depths sampled. Estimates of Q are lacking in the tables for data in which the resulting α estimate was negative. These negative estimates occur in lines in which the attenuation of energy was less severe than that caused by spherical spreading, possibly due to the effect of "resonance".

ROSE line 2L data, although relatively sparse with respect to shot density, is considered to be of higher quality than the line 2S data in which a smaller number of data channels was used. In table 6-2, results for path 1P are also presented for ESP and MABS data for 2S. The parameters of the regression are considerably more scattered than those for 2L and the correlation coefficients of some 2S results decreases below .1. In comparing the 2L and 2S parameters, with the data from 2S involving offsets up to, but not including, the ranges at which "resonance" occurred, a consistent feature appears to be the decrease of the estimated slope, α , with increasing center frequency. In both the 25 lb ESP and the MABS 2S cases, α is a maximum at the lowest frequency and decreases so that at the upper center frequency, it is negative. This is a suspect result since α , reflecting (at least partially) absorption losses in the crust, would be expected to increase with frequency, perhaps linearly as in the data published in Hamilton

Path	Data Set	Center Freq. (Hz)	N	α (db/km)	β (db)	ρ	σ	Q
2P	Line 2L	5	11	.04	37.91	.11	2.92	487
	(20 to	8	11	.07	41.25	.26	3.11	445
	104 km	11	10	.04	46.53	.3	1.57	1072
	offset)	14	10	.08	49.62	.34	2.73	682
2P	Line 2S	8	5	-.20	45.74	.06	3.06	-
	(ESP 5#	12	5	-.45	50.58	.46	1.92	-
	shots; 16	16	5	-.26	51.06	.29	1.59	-
	to 30 km)							
2P	Line 2S	8	3	.67	21.76	.32	3.43	46
	(ESP 25#	12	3	.83	16.84	.99	.21	56
	shots; 17	16	3	.28	39.36	.18	2.06	222
	to 35 km)							
2P	Line 2S	8	8	.59	24.18	.4	2.43	53
	(MABS; 16	12	8	-.29	44.00	.22	1.66	-
	to 25 km)	16	8	.19	35.56	.03	2.99	328
	offset)							
1W	Line 2L	8	5	-.005	28.75	.0008	1.93	-
	(20 to	11	5	.26	32.24	.26	2.16	769
	52 km)	14	5	.87	47.59	.87	2.12	292
1W	Line 2S	8	12	.1	29.9	.39	.95	1455
	(ESP; 15	12	12	-.07	29.75	.04	2.19	-
	to 42 km;	16	12	.07	19.34	.02	.98	4158
	all shots)							
1W	Line 2S	8	6	.05	31.87	.19	.8	2910
	(ESP to 42	12	6	-.19	34.6	.28	2.13	-
	km; 25# shots)							
1W	Line 2S	8	6	.10	29.48	.22	.89	1455
	(to 30 km;	12	6	-.16	30.74	.3	1.20	-
	5# shots)							
"Layer 2"	Line 2S	8	4	-.1	54.34	.13	.93	-
	(ESP)	12	4	-.37	58.71	.44	1.59	-
		16	2	-.58	67.5	1.00		-

Table 6-3

Results of linear regression for paths 2P, 1W, and "layer 2" returns

(1972). Although the 2S data is scattered, this pattern is corroborated in the 2L results within the 20 to 35 km offset range. This phenomenon may be caused by the "resonance" affecting the estimated slope at offsets less than 35km. Another possibility is that, as a general rule, bias corrections tend to be largest at higher frequencies where original frequency/wavenumber estimates are usually lower. Higher frequency data may have tended to be "over-corrected", causing this pattern in the regression parameters. The pattern, however, seems to be associated with data collected up to the resonance point only. Line 2L data, beyond 35 km, is not affected as severely.

In table 6-3, results of regressions performed on TL estimates for paths 2P, 1W, and the low level, possibly "layer 2", events are tabulated. In accord with results in the CANBARX paper, the insertion losses for the multiple reflection/refraction path, 2P, are greater than those for the primary 1P, but attenuations, α , especially in the 24 channel data, tend to be smaller (near zero). The phenomenon of relatively high multiple amplitudes is commonly observed in refraction profiles but remains to be analysed rigorously. In all the 2P data presented, the correlation coefficients are considerably smaller than those for 1P, possibly due to the rough topography encountered in the waterborne segments of these events.

The effects of seafloor topography also extend to the 1W data in which all of the regression parameters tabulated again have relatively low correlation coefficients. As discussed previously, the theoretical path for these events encounters the seafloor before arriving at the receivers. For line 2L data, insertion loss and, in this case, α increases with frequency. Care must be taken in interpreting this result because, as we have seen, large Lloyd mirror and directivity corrections are incorporated in the higher

frequency estimates. Although the quality of the linear fit is poor, due to the rough bathymetry, the estimated slopes from line 2S average near zero, implying near spherical spreading for 1W.

Finally, although only four events could be identified as being possible "layer 2" arrivals, the regression results for these, available only for line 2S, show the same decreasing slope pattern with frequency that was encountered in Table 6-2. The magnitudes of the slopes roughly correspond to the slopes obtained for 1P in ESP-2S, but the insertion loss is markedly higher. This is in sharp contrast with the low α for events considered to be layer 2 arrivals in the CANBARX paper. The identification of this set of events in the ROSE data remains undetermined: the arrival times corresponding to those of possible shear arrivals (which would account for the high insertion loss due to poor coupling between compressional and shear waves at the basement), but the estimated phase velocities at the array tending to be too high for shear propagation.

Summary

In applying MLM array processing techniques to the analysis of data from the ROSE experiment, the effectiveness of the velocity estimation procedure was diminished by extremely rough topography. Estimated phase velocities at the array reflect variations in bathymetry as well as the properties of crustal sections with which generated energy interacts. Results obtained in applying the same analysis techniques to data from experiments such as CANBARX (Baggeroer & Falconer, 1981) and FRAM II (Duckworth et al,

1982), in which bottom roughness was much less severe, have been more successful in the inversion of the velocity information obtained into higher resolution crustal models. We have shown that, even in a "worst case" situation, the ability of the algorithm to discriminate arrivals by means of relative phase velocity estimates is valuable when combined with more conventional methods of processing refraction data.

Apart from considerations of velocity structure, we have shown that amplitude information obtained from MLM estimates can be used effectively for obtaining estimates of transmission loss in the crust. Although some work has been done in determining TL in marine sediments, the work described here and in the CANBARX paper (Baggeroer & Falconer) is a rare attempt at estimating crustal losses. The results of both papers agree in insertion loss estimates for primary crustal paths. The attenuation of primary paths, on the order of .5 db/km in the CANBARX results, is somewhat smaller, on the order of .2 db/km, in the work done with the ROSE data.

The ROSE results incorporate corrections obtained by the introduction of a procedure for the removal of bias effects in the MLM algorithm, so that TL estimates are more accurate. This procedure, based on empirical results, is applicable to MLM estimates obtained from sparse arrays, which are often the only economical and practical means of obtaining the benefits of array techniques in the marine environment.

REFERENCES

Aki,K.; Richards,P., Quantitative Seismology, Theory and Methods, W.H. Freeman & Co., 1980.

Baggeroer,A.B.; Falconer,R., "Array refraction profiles and crustal models of the Canada basin", JGR (in press), 1981.

Capon,J., "High resolution frequency wavenumber spectral analysis", Proc IEEE, Vol. 57, 1969.

Capon,J.; Goodman,N.R., "Probability distributions for estimators of the frequency wavenumber spectrum", Proc IEEE, Vol. 58, 1970.

Cerveny,V.; Ravindra R., Theory of Seismic Head Waves, University of Toronto Press, 1971.

Christensen,N.I.; Salisbury,M.H, "Structure and Constitution of the Lower Oceanic Crust", Reviews of Geophysics and Space Physics", Vol. 13, 1975.

Clay,C.S.; Medwin,H., Acoustical Oceanography, John Wiley and Sons, 1977.

Detrick,R.S.;Purdy,G.M.,"Crustal structure of the Kane fracture zone from seismic refraction studies", JGR, Vol.85, 1980.

Duckworth,G.L.;Baggeroer,A.B.;Jackson,H.R.,"Crustal Structure Measurements near Fram II in the Pole Abyssal Plain", Tectonophysics, (in press),1982.

Dyer,I., Class Notes from MIT course 13.85, Spring, 1981.

Edelblute,D.J.; Fisk,J.M.; Kennison,G.L.,"Criteria for optimum signal detection for arrays", JASA, Vol.41, 1967.

Ewing,J.,"Elementary theory of seismic refraction and reflection measurements" in The Sea, Vol.3, Interscience, 1963.

Ewing,J.; Houtz,R., "Mantle reflections on airgun-sonobuoy profiles", JGR, Vol.74, 1969.

Ewing,J.I.; Purdy,G.M., "Upper Crustal Velocity Structure in the Rose are of the East Pacific Rise", JGR (in press), 1982.

Goodman,N.R.,"Statistical Analysis based on a certain multivariate complex Gaussian distribution", Ann. Math. Stat., Vol.34, 1963.

Grant,F.S.; West,G.F., Interpretation Theory in Applied Geophysics, McGraw Hill, 1965.

Jacobson,R.S.; Shor, G.G.;Dorman,L.M., "Linear inversion of body wave data-Part II: Attenuation versus depth using spectral ratios", Geophysics, Vol.46, 1981.

Kennett,B.L.N., "Towards a more detailed seismic picture of oceanic crust and mantle", Marine Geophysical Researches 3, 1977.

Lacoss,R.T., "Data Adaptive Spectral Analysis Methods", Geophysics, Vol.36, 1971.

Lewis,B.T.R.; Snydsman,W.E., "Evidence for a low velocity layer at the base of the crust", Nature, vol.266, 1977.

Lewis, B.T.R., "Evolution of ocean crust seismic velocities", Ann. Rev. Earth Planet Sci., Vol.6, 1978.

Ludwig,W.; Rabinowitz,P.D., "Structure of Vema fracture zone", Marine Geology, 1980.

Leverette,S.J.,"Data adaptive velocity/depth spectra estimation in seismic wide angle reflection analysis", PhD Thesis, MIT, 1977.

Orcutt,J.A.; Kennett,B.L.N.; Dorman,L.M., "Structure of the East Pacific Rise from an ocean bottom seismometer survey", Geophys. J.R. Astron. Soc.,Vol.45, 1976.

Prada,K.E.,"A system for digital acquisition and processing of marine seismic profiling data",OCEAN '74, IEEE Int Conf Engineering Ocean Environment, IEEE Publ 74-CHO-873-0-OCC, 1974.

Purdy,G.M., "The variability in seismic structure of layer 2 near the East Pacific Rise at 12 N", JGR (in press), 1982.

Raitt,R.W.,"The crustal rocks" in The Sea, Vol 3, Interscience, 1963.

Sereda,I.T.; Hajnal,Z.,"Velocity analysis of multifold near-vertical crustal reflection data", presented at 46th annual international SEG meeting, 1976.

Stoffa,P.L.; Buhl,P.,"Two-ship multichannel seismic experiments for deep crustal studies", JGR, Vol. 84, 1979.

Stoffa,P.L.; Diebold,J.B.; Buhl,P., "Inversion of seismic data in the tau-p plane", Geophysical Research Letters, Vol.8, 1981.

Telford,W.M.; Geldart,L.P.; Sheriff,R.E.; Keys,D.A., Applied Geophysics, Cambridge University Press, 1976.

Wakely, J., "Pressure Signature Model for an Underwater Charge", U.S. Navy Journal of Underwater Acoustics", Vol.27, 1977.

Appendix 4-1

Correlation and density functions between inputs and outputs of linear filters

The correlation function of a simple random process x(t) is defined as:

$$R_x(\tau) = \mathcal{E}\{x(t)\,x^*(t-\tau)\}$$

where $\mathcal{E}$ denotes expectation, and the superscript * is the complex conjugate. In the situation shown in fig. 4-1, a process x(t) is the input to a pair of linear filters with frequency responses $H_1(f)$ and $H_2(f)$, and impulse responses $h_1(t)$ and $h_2(t)$. The output of a filter is just:

$$y(t) = x(t) * h(t)$$
$$= \int x(\tau)\,h(t-\tau)\,d\tau$$

where * denotes convolution. The correlation function of the output process $y_1(t)$ with <u>any</u> desired process, d(t), is:

$$R_{y_1 d}(\sigma) = \mathcal{E}\{y_1(t)\,d^*(t-\sigma)\}$$
$$= \int_{-\infty}^{\infty} h_1(t-\tau)\,\mathcal{E}\{x(\tau)\,d^*(t-\sigma)\}\,d\tau$$
$$= \int_{-\infty}^{\infty} h_1(t-\tau)\,R_{xd}(\tau-t+\sigma)\,d\tau$$

With the substitution $\tau' = t-\tau$, we get:

$$R_{y_1 d}(\sigma) = \int_{-\infty}^{\infty} h_1(\tau')\,R_{xd}(\sigma-\tau')\,d\tau'$$

$$= h_1(\sigma) * R_{xd}(\sigma) \qquad \text{(A4-1-1)}$$

Likewise, the correlation function $R_{dy_1}(\sigma)$ is:

$$R_{dy_1}(\sigma) = \mathcal{E}\{d(t)\,y_1^*(t-\sigma)\}$$
$$= \int_{-\infty}^{\infty} h_1^*(t-\sigma-\tau)\,\mathcal{E}\{d(t)\,x^*(\tau)\}\,d\tau$$
$$= \int h_1^*(t-\sigma-\tau)\,R_{dx}(t-\tau)\,d\tau$$

With the substitution $\tau' = t-\tau$, we have:

$$R_{dy_1}(\sigma) = \int h_1^*(\tau'-\sigma)\,R_{dx}(\tau')\,d\tau$$
$$= h_1(-\sigma) * R_{dx}(\sigma) \qquad \text{(A4-1-2)}$$

If we take the Fourier transform of A4-1-1 and A4-1-2, we obtain the spectral density functions:

$$S_{y_1 d}(f) = H_1(f) S_{xd}(f) \tag{A4-1-3}$$

$$S_{dy_1}(f) = H_1^*(f) S_{dx}(f) = H_1^*(f) S_{xd}^*(f) \tag{A4-1-4}$$

From A4-1-3, using $d(t) = y_1(t)$, we obtain:

$$S_{y_1}(f) = H_1(f) S_{xy_1}(f)$$

Now using $d(t) = x(t)$ in A4-1-4, we get:

$$S_{y_1}(f) = H_1(f) H_1^*(f) S_x(f) = |H_1(f)|^2 S_x(f) \tag{A4-1-5}$$

Also, if $d(t)$ is $y_2(t)$ in A4-1-3:

$$S_{y_1 y_2}(f) = H_1(f) S_{x y_2}(f)$$

Now letting $x(t)$ be $d(t)$ in A4-1-4:

$$S_{y_1 y_2}(f) = H_1(f) H_2^*(f) S_x(f) \tag{A4-1-6}$$

Appendix 4-2

Calculation of spectral density function of the output of an array processor

Referring to fig. 4.2, the output of the processor is just:

$$y(t) = \sum_i y_i(t)$$

where:

$$y_i(t) = g_i(t) * x_i(t)$$

The correlation function of this output is then:

$$R_y(\sigma) = \mathcal{E}\{y(t)\, y^*(t-\sigma)\}$$

$$= \mathcal{E}\left\{\left[\sum_i y_i(t)\right]\left[\sum_j y_j^*(t-\sigma)\right]\right\}$$

Taking the expectation inside of the summations, we obtain:

$$R_y(\sigma) = \sum_i \sum_j \mathcal{E}\{y_i(t) y_j^*(t-\sigma)\}$$

$$= \sum_i \sum_j R_{y_i y_j}(\sigma) \qquad \text{(A4-2-1)}$$

We rewrite equations A4-1-1 and A4-1-2 from Appendix 4-1:

$$R_{y_i d}(\sigma) = g_i(\sigma) * R_{x_i d}(\sigma) \qquad \text{(A4-2-2)}$$

$$R_{d y_i}(\sigma) = g_i(-\sigma) * R_{d x_i}(\sigma) \qquad \text{(A4-2-3)}$$

where d(t) is any desired process. Identifying $y_j(t)$ with d(t) in A4-2-2, equation A4-2-1 becomes:

$$R_y(\sigma) = \sum_i \sum_j g_i(\sigma) * R_{x_i y_j}(\sigma)$$

Now identifying d(t) with $x_j(t)$, we obtain:

$$R_y(\sigma) = \sum_i \sum_j g_i(\sigma) * g_j(-\sigma) * R_{x_i x_j}(\sigma) \qquad \text{(A4-2-4)}$$

Taking the Fourier transform, we get:

$$S_y(f) = \sum_i \sum_j G_i(f)\, G_j^*(f)\, S_{x_i x_j}(f) \qquad \text{(A4-2-5)}$$

Appendix 4-3

Derivation of Optimal Response Function for Arbitrary Noise Covariance

We wish to minimise $S_y(f) = \sum_{i=1}^{K}\sum_{j=1}^{K} G_i(f)\, S_{ij}(f)\, G_j^*(f)$ with the constraint that $\mathcal{L}(f, \underline{v}_t) = 1 = \sum_{i=1}^{K} G_i(f)\, e^{-j2\pi \underline{v}_t \cdot \underline{\Delta}_i}$.

Via Lagrangian Multipliers:

$$\text{MIN: over } G_i(f) \quad \sum_{i=1}^{K}\sum_{j=1}^{K} G_i(f) S_{ij}(f) G_j^*(f) + \lambda(f)\left\{\sum_{i=1}^{K} G_i(f) e^{-j2\pi \underline{v}_t \cdot \underline{\Delta}_i} - 1\right\}$$

a) Take partials $\frac{\partial}{\partial G_k(f)}$ and set to zero:

$$2\sum_{j=1}^{K} S_{kj}(f)\, G_j^*(f) + \lambda(f) e^{-j2\pi \underline{v}_t \cdot \underline{\Delta}_k} = 0$$

for k = 1, 2,....,K.

b) Define vector $\underline{G}(f) = [G_1(f), G_2(f), \ldots\ldots, G_K(f)]^T$, the steering vector $\underline{E}(f, \underline{v}_t)^T = [e^{j2\pi \underline{v}_t \cdot \underline{\Delta}_1}, \ldots\ldots, e^{j2\pi \underline{v}_t \cdot \underline{\Delta}_K}]$, and the KxK Hermitian matrix $[S_{ij}(f)]$, so that we may write the above as:

$$2[S_{ij}(f)]\,\underline{G}^* + \lambda(f)\,\underline{E}^*(f, \underline{v}_t) = 0$$

or

$$\underline{G}^*(f) = -\frac{\lambda(f)}{2}[S_{ij}(f)]^{-1}\underline{E}^*(f, \underline{v}_t) \qquad \text{(A4-3-1a)}$$

or

$$\underline{G}^T(f) = -\frac{\lambda(f)}{2}[S_{ij}(f)]^{-1}\underline{E}^*(f, \underline{v}_t) \quad \text{(by taking conjugate transpose)} \qquad \text{(A4-3-1b)}$$

c) Take partial $\frac{\partial}{\partial \lambda(f)}$ and set to zero:

$$\sum_{i=1}^{K} G_i(f) e^{-j2\pi \underline{v}_t \cdot \underline{\Delta}_i} = \underline{G}^T \underline{E}^* = 1$$

d) Substitute for $\underline{G}^T$ from A4-3-1b:

$$1 = -\frac{\lambda(f)}{2}\underline{E}^T(f, \underline{v}_t)[S_{ij}(f)]^{-1}\underline{E}^*(f, \underline{v}_t)$$

or

$$-\frac{\lambda(f)}{2} = \left[\underline{E}^T(f, \underline{v}_t)[S_{ij}(f)]^{-1}\underline{E}^*(f, \underline{v}_t)\right]^{-1}$$

e) Now substitute $-\frac{\lambda(f)}{2}$ into equations A4-3-1:

$$\underline{G}^*(f) = \frac{[S_{ij}(f)]^{-1}\underline{E}^*(f,\underline{\nu}_t)}{\underline{E}^T(f,\underline{\nu}_t)[S_{ij}(f)]^{-1}\underline{E}^*(f,\underline{\nu}_t)} \qquad \text{(A4-3-2a)}$$

$$\underline{G}^T(f) = \frac{\underline{E}^T(f,\underline{\nu}_t)[S_{ij}(f)]^{-1}}{\underline{E}^T(f,\underline{\nu}_t)[S_{ij}(f)]^{-1}\underline{E}^*(f,\underline{\nu}_t)} \qquad \text{(A4-3-2b)}$$

f) Since $\mathcal{Y}(f,\underline{\nu}) = \sum_{i=1}^{k} G_i(f)\, e^{-j2\pi \underline{\nu}\cdot\underline{r}_i} = \underline{G}^T\underline{E}^*(f,\underline{\nu})$,

we have:

$$\mathcal{Y}(f,\underline{\nu}) = \frac{\underline{E}^T(f,\underline{\nu}_t)[S_{ij}(f)]\underline{E}^*(f,\underline{\nu})}{\underline{E}^T(f,\underline{\nu}_t)[S_{ij}(f)]^{-1}\underline{E}^*(f,\underline{\nu}_t)} \qquad \text{(A4-3-3)}$$

g) The spectral density function of the output, which is also the MLM estimate of the frequency wavenumber function, is found by substituting from eqs. A4-3-2 into the quadratic form:

$$\begin{aligned} S_{\mathcal{Y}}(f) &= \underline{G}^T[S_{ij}(f)]\underline{G}^* \\ &= \frac{\underline{E}^T(f,\underline{\nu}_t)[S_{ij}(f)]^{-1}}{\underline{E}^T(f,\underline{\nu}_t)[S_{ij}(f)]^{-1}\underline{E}^*(f,\underline{\nu}_t)}[S_{ij}(f)]\frac{[S_{ij}(f)]^{-1}\underline{E}^*(f,\underline{\nu}_t)}{\underline{E}^T(f,\underline{\nu}_t)[S_{ij}(f)]^{-1}\underline{E}^*(f,\underline{\nu}_t)} \\ &= \frac{1}{\underline{E}^T(f,\underline{\nu}_t)[S_{ij}(f)]^{-1}\underline{E}^*(f,\underline{\nu}_t)} \qquad \text{(A4-3-4)} \end{aligned}$$

Appendix 4-4

Derivation of Optimal Response Function for Uncorrelated Sensor Noise

We wish to minimize $S_y(f) = \sum_{i=1}^{K} S_w(f) |G_i(f)|^2$ with the constraint that $\mathcal{D}(f, \underline{\nu}_t) = 1 = \sum_{i=1}^{K} G_i(f)\, e^{-j 2\pi \underline{\nu}_t \cdot \underline{\Delta}_i}$.

Via Lagrangian multipliers:

$$\text{MIN: over } G_i(f) \quad S_w(f) \sum_{i=1}^{K} |G_i(f)|^2 + \lambda(f) \left[\sum_{i=1}^{K} G_i(f) e^{-j 2\pi \underline{\nu}_t \cdot \underline{\Delta}_i} - 1 \right] \tag{A4-4-1}$$

a) Take partials $\frac{\partial}{\partial G_k(f)}$ and set to zero:

$$2 S_w(f) G_{ke}^*(f) + \lambda(f) e^{-j 2\pi \underline{\nu}_t \cdot \underline{\Delta}_{ke}} = 0$$

or

$$G_{ke}(f) = \frac{-\lambda(f) e^{+j 2\pi \underline{\nu}_t \cdot \underline{\Delta}_{ke}}}{2 S_w(f)} \tag{A4-4-2}$$

b) Take partial $\partial/\partial\lambda(f)$ and set to zero:

$$\sum_{i=1}^{K} G_i(f) e^{-j 2\pi \underline{\nu}_t \cdot \underline{\Delta}_i} - 1 = 0 \tag{A4-4-3}$$

c) Substitute value of $G_{ke}(f)$ in A4-4-2 into A4-4-3, and obtain:

$$\sum_{i=1}^{K} \left(- \frac{\lambda(f)}{2 S_w(f)} \right) - 1 = 0$$

or,

$$\lambda(f) = - \frac{2 S_w(f)}{K}$$

d) Substitute value of $\lambda(f)$ into A4-4-2 and get final results:

$$G_{ke}(f) = \frac{e^{j 2\pi \underline{\nu}_t \cdot \underline{\Delta}_{ke}}}{K} \tag{A4-4-4}$$

$$\mathcal{D}(f, \underline{\nu}) = \sum_{i=1}^{K} G_i(f) e^{-j 2\pi \underline{\nu} \cdot \underline{\Delta}_i} = \sum_{i=1}^{K} \frac{e^{-j 2\pi (\underline{\nu} - \underline{\nu}_t) \cdot \underline{\Delta}_i}}{K} \tag{A4-4-5}$$

Appendix 4-5

Evaluation of correlation function of Fourier coefficients from a sensor pair

$$\text{Let } X_{iw}(f_1) = \int_{-T/2}^{+T/2} x_i(t)\, w(t)\, e^{-j2\pi f_1 t}\, dt$$

be the Fourier coefficient at f_1, associated with the windowed time series from sensor i. The window length is T sec. Then the correlation function:

$$\mathcal{E}\left\{X_{iw}(f_1) X^*_{jw}(f_2)\right\} = \int_{-T/2}^{+T/2} dt_1 \int_{-T/2}^{+T/2} dt_2\, \overline{x_i(t_1) x_j^*(t_2)}\, w(t_1) w^*(t_2) e^{-j2\pi f_1 t_1} e^{+j2\pi f_2 t_2}$$

$$= \int_{-T/2}^{T/2} dt_1 \int_{-T/2}^{T/2} dt_2\, R_{x_i x_j}(t_1 - t_2)\, w(t_1) w^*(t_2) e^{-j2\pi f_1 t_1} e^{+j2\pi f_2 t_2}$$

Substitute the density function associated with $R_{x_i x_j}(t_1, t_2)$:

$$= \int dv\, S_{ij}(v) \int dt_1\, w(t_1) e^{j2\pi(v - f_1)t_1} \int dt_2\, w(t_2) e^{-j2\pi(v - f_2)t_2}$$

$$= \int dv\, S_{ij}(v)\, W^*(v - f_1) W(v - f_2)$$

where $W(f) = \int_{-T/2} w(t) e^{-j2\pi f t}\, dt$

If BW is the effective bandwidth of the transform of the window function (which, for a cosine window is $8/3T \approx$ 2.6 Hz for T = 1 sec), then:

$$\mathcal{E}\left\{X_{iw}(f_1) X^*_{jw}(f_2)\right\} \approx \begin{cases} 0 & (f_1 - f_2 > BW) \\ S_{x_i x_j}(f_1) \int W(v)^* W(v - (f_1 - f_2))\, dv & (f_1 - f_2 \leq BW) \\ S_{x_i x_j}(f_1) \int_{-\infty}^{\infty} |W(v)|^2\, dv & (f_1 = f_2) \end{cases}$$

Appendix 6-1

Corrections to Frequency/Wavenumber Estimates due to Sampling

For a pressure waveform at location $\underline{r}$ of length T, with an approximately constant spectral density, $\mathcal{S}_p(\bar{f},\underline{r})$, across frequency band, W, we can write:

$$\tilde{p}^2_{f_o,W}(\underline{r}) = \frac{1}{T}\int_{-T/2}^{T/2} p^2_{f_o,W}(\underline{r},(t))\,dt \approx W\mathcal{S}_p(f_o,\underline{r})$$

or:

$$\mathcal{S}_p(f_o,\underline{r}) \approx \frac{1}{WT}\int_{-T/2}^{T/2} p^2_{f_o,W}(\underline{r},t)\,dt$$

If we sample data at an interval ΔT, we can approximate this as:

$$\mathcal{S}_p(f_o,\underline{r}) \approx \frac{1}{WT}\sum_{n=0}^{N-1} p^2_{f_o,W}(\underline{r},n\Delta T)\Delta T = \frac{\Delta T}{WT}\sum_{n=0}^{N-1} p^2_{f_o,W}(n\Delta T)$$

where $N = T/\Delta T$. In terms of the two sided discrete Fourier transform of the raw, broadband mean square pressure, $\bar{p}^2_{f_o,W}(n\ T)$, this becomes:

$$\mathcal{S}_p(f_o,\underline{r}) = \frac{\Delta T}{WT}\sum_{n=0}^{N-1}\left|\frac{1}{N}\sum_{k=k_o-\frac{M}{2}\Delta f}^{k=k_o+\frac{M}{2}\Delta f} P(k\Delta f)\,e^{-j\frac{2\pi nk}{N}}\right|^2$$

where k_o is the frequency term number corresponding to f_o, and Δf is the coefficient spacing in Hz. Rewriting this as:

$$\mathcal{S}_p(f_o,\underline{r}) = \frac{\Delta T}{WT}\frac{1}{N}\sum_{k}\sum_{k'} P(k\Delta f)P(k'\Delta f)\left\{\frac{1}{N}\sum_{n=0}^{N-1} e^{-j2\pi\frac{(k-k')n}{N}}\right\}$$

and recognizing that the quantity in brackets is zero unles $k' = iN$ (i integer), we have:

$$\mathcal{S}_p(f_o,\underline{r}) = \frac{\Delta T}{WTN}\sum_{k=k_o-\frac{M}{2}\Delta f}^{k=k_o+\frac{M}{2}\Delta f}|P(k\Delta f)|^2$$

For data sampled exactly at the Nyquist rate, $1/\Delta T = 2W'$, where W' is the total bandwidth of the input, the spacing of the N (= $T/\Delta T$) frequency coefficients in the DFT is just:

$$\frac{2W'}{N} = \frac{2W'\Delta T}{T} = \frac{1}{T}$$

The number of terms (M) in the present band, W, is then:

$$M = W/1/T = WT$$

We can rewrite the expressions for the density function as:

$$\mathcal{S}(f_0, \underline{\Delta}) = \frac{\Delta T}{WTN} \cdot WT \; \frac{\sum_{k} |P(k\Delta f)|^2}{WT}$$

or

$$\mathcal{S}(f_0, \underline{\Delta}) = \frac{(\Delta T)^2}{T} \; \frac{\sum_{k=k_0-M/T}^{k=k_0+M/T} |P(k\Delta f)|^2}{M}$$

Appendix 6-2

Lloyd Mirror Correction

Referring to Fig. 6-1, EDA represents a pure sinusoidal plane wavefront with frequency f, arriving at a sensor at point A at time t. The vertical angle is α and hydrophone depth is BA = d. The sensor will also be influenced at this moment by a surface reflected arrival that has traversed the extra distance DC + CA. Assuming specular reflection:

$$\angle ECD = \angle BCA = \beta$$

the geometry of the situation will be as shown. The extra distance travelled is then:

$$DC + CA = \frac{d}{\cos\alpha}\left[1 + \cos 2\alpha\right]$$

$$= 2d\cos\alpha$$

If the upcoming arrival is a pure sinusoidal plane wave with frequency f and unit amplitude, the waveform at A can be written as:

$$e^{j\omega t}\left[1 + e^{-\frac{2d\cos\alpha}{c}}\right]$$

where we have assumed perfect reflection at the surface except for a 180° phase shift.The amplitude of the resultant waveform is then:

$$\left| 1 - e^{-\frac{4\pi f d\cos\alpha}{c_o}} \right| = \left| 2\sin\left(2\pi\frac{fd\cos\alpha}{c_o}\right) \right|$$